Nanolithography with an atomic force microscope: quantum point contacts, quantum dots, and quantum rings

Vom
Fachbereich Physik der Universität Hannover
zur Erlangung des Grades
Doktor der Naturwissenschaften
- Dr. rer. nat. -
genehmigte Dissertation
von

Dipl. Phys. Ulrich Felix Keyser

geboren am 31. März 1975 in Braunschweig

2002

Referent: Prof. Dr. R. J. Haug
Korreferent: Prof. Dr. W. Wegscheider

Tag der Promotion: 10.7.2002

One Ring to rule them all, One Ring to find them,
One Ring to bring them all and in the darkness bind them

J. R. R. Tolkien

Abstract

In this thesis we used the atomic force microscope (AFM) for the creation of complex mesoscopic devices with various geometries. The basis for our experiments were GaAs/AlGaAs-heterostructures with two-dimensional electron gases (2DEG) 57 nm, 40 nm, and 34 nm below the surface. We studied in detail controlled mechanical nanomachining and local oxidation.

We fabricated ballistic quantum point contacts by engraving a constriction into a GaAs/AlGaAs-heterostructure with the tip of an AFM. The devices were nanomachined using both a silicon tip and a diamond tip to study the influence of the tip material. It turned out that a diamond tip is almost perfect not only for a fast and simple processing but also in forming proper potential profiles to observe ballistic electron transport. The appearance of the 0.7 ($2e^2/h$) conductance anomaly confirms the high quality of diamond-engraved devices. We deduced the depletion lengths induced by the different tips, yielding $\sim$ 200 nm for diamond-engraved samples, which is roughly two times smaller than typical depletion lengths in devices patterned with a Silicon tip.

A detailed study of the local oxidation with an AFM proved the importance of the oxidation current for the controlled fabrication of tunnelling barriers in 2DEGs. We found a linear dependence of the barrier height on the oxidation current which is related to the depth of the oxide lines. With these tunnelling barriers we fabricated a single-electron transistor containing several hundred electrons well described by the constant interaction model.

Further we demonstrated that the AFM-based nanolithography provides a relatively easy and controlled approach to create parallel quantum dots. The double dot was stepwise fabricated with a combination of controlled nanomachining and local oxidation. The dots were defined by splitting a quasi-one-dimensional resonant tunnelling diode in two separate zero-dimensional regions. Analysing of the transport measurements of the two quantum dots allowed the identification of the specific Coulomb-blockade oscillations of each dot. We showed that the current

could be directed through both quantum dots separately by applying high negative gate voltages to the respective in-plane gates. These experiments proved that the combination of controlled nanomachining and local oxidation with an atomic force microscope is a straightforward approach to fabricate robust mesoscopic devices.

In the remaining part of the thesis we investigated the transport characteristic of a quantum ring defined by local oxidation in great detail. We discussed the Aharonov-Bohm effect in this asymmetric quantum ring with a diameter of below 450 nm. The analysis of the data with Fourier transformation indicated only one interfering subband in the ring. This led to a modulation of the conductance of more than 50%. The electron orbit extracted from the periodicity of the Aharonov-Bohm effects fits perfectly to the ring geometry. The attached in-plane gates allow to tune the phase of the Aharonov-Bohm effect at zero magnetic field and we observed the typical sharp phase jumps by π that are related to the asymmetry of our device. Finally, we showed that the line-shape of the resonances in the quantum ring is controlled by an outer gate voltage and the magnetic field. This fact was explained by interference between a resonant bound state and directly submitted electrons. This led to a Fano like characteristic.

The attached in-plane gates of the quantum ring allowed to study the same device in the Coulomb-blockade regime. With the observation of spin flips in the addition spectrum in a perpendicular magnetic field we determined the number of electrons to below ten in this voltage range. The observation of a Kondo effect enabled to study the spin structure of the measured quantum ring. The Kondo resonances vanished and broadened with increasing temperature. The peak conductance follows the universal curve and was used to estimate the Kondo temperature of the device. Non-linear transport measurements showed an even-odd behaviour of the Kondo effect. This result together with a Zeeman splitting in a perpendicular magnetic field led to the conclusion that the Kondo effect was induced by a single spin on the ring. The magnetic field dependence of the conductance in the Kondo valley could be interpreted as ballistic transport of as few as five electrons.

At low magnetic fields we observed oscillations in the ground state of the device with a periodicity related to the number of electrons on the ring. This effect caused by strong electron-electron interactions was attributed to the small number of electrons. We found Aharonov-Bohm oscillations of the conductance in the Kondo regime as well. The finite conductance due to the Kondo effect was used for an analysis of the

phase evolution of this Aharonov-Bohm effect in the Coulomb-blockade valley. The measurement yielded phase jumps by π at the Coulomb-blockade resonances and a smooth shift of the Aharonov-Bohm maxima in between.

The observation of the Kondo and Aharonov-Bohm effect shows the wide range of possible research topics for these kind of devices. Due to their smallness together with the few electrons and the exact control of the sample parameters these devices are ideal systems to compare the experimental results with theoretical predictions. With the AFM-based lithography it should be possible to design novel geometries for mesoscopic systems, which may show an unexpected variety of new effects in transport experiments.

Keywords
nano fabrication, Kondo effect, Aharonov-Bohm effect

Schlagworte
Nanostrukturierung, Kondoeffekt, Aharonov-Bohm-Effekt

Contents

1 Introduction

It has been always a dream for experimentalists to *design* artificial confinement potentials for electrons. In semiconductor physics these are realized in quantum dots consisting of up to several hundred atoms [1]. These quantum dots are often called *mesoscopic* because they are much smaller than macroscopic crystals but still larger than single atoms in the microscopic world. A very successful approach to investigate exciting effects like electron-electron interactions and interference phenomena in these systems is transport spectroscopy, which allows to probe the wave function of the confined electrons.

Two key concepts in solid state physics have enabled the direct fabrication of small quantum dots investigated in this thesis. The first is the invention of modulation doped GaAs/AlGaAs-heterostructures in 1978 allowing the production of high-quality two-dimensional electron gases (2DEG) [2]. The second milestone was the development of the scanning tunnelling microscope in 1982 by Binnig and Rohrer [3], which allowed the investigation of surfaces with atomic resolution and even the displacement of single atoms [4] in the following years. In 1986 the invention of the atomic force microscope (AFM) [5] boosted the development of the new field of nanotechnology in all natural sciences ranging from biology to physics.

In this thesis we combine 2DEG and AFM lithography for a realization of mesoscopic devices. For the observation of quantum mechanical effects one has to shrink the dimensions of a quantum dot to the wavelength of electrons in the material system. Within a 2DEG the typical wavelength of the electrons lies around some ten nanometers which is more than two orders of magnitude longer than in metals. The typical tip of an AFM has a radius of below ten nanometers which is even smaller than the wavelength of the electrons. Therefore, an AFM tip is a natural candidate for the local manipulation of the electronic structure in a 2DEG.

The first demonstration of the depletion of a 2DEG with an AFM was published in 1995 [6] almost one decade after the invention of

the AFM. In these experiments the AFM tip induced a local chemical oxidation at the surface of a heterostructure. As a consequence the band structure is distorted locally underneath the created oxide line and the 2DEG is depleted. A completely different technique is the removal of atoms from a surface with an AFM tip used as a nanoscopic engraving tool. This is the most direct method of modifying a 2DEG with an AFM.

The advantages of both techniques are obvious, no further processing of the samples is needed, no photoresists, chemical etching, masks, or metallizations. Additionally, there are no limitations to the device geometry and the accuracy of the lithography lies in the range of a few nanometers.

With the controlled nanomachining [7] and the local oxidation a realization of quantum dots in a 2DEG is possible [8, 9, 10]. In addition, we discuss the possibility to create multiple connected topologies with the AFM like rings with an inner and outer boundary. These devices allow to study interference phenomena like the Aharonov-Bohm effect [11] in the Kondo regime [12, 13, 14, 15, 16, 17] where electron-electron correlation effects dominate the transport characteristic.

Outline

Chapter 2 begins with a short description of electrons confined to low dimensional conductors, namely two-, one-, and zero-dimensional systems, respectively. As examples for transport phenomena we discuss the ballistic transport through quantum point contacts and the tunnelling of electrons through potential barriers. The chapter ends with a brief introduction to resonant tunnelling diodes based on 2DEG.

Chapter 3 contains a detailed overview of the GaAs/AlGaAs-heterostructures used as a basis for the realization of the mesoscopic devices. With self-consistent calculations of the band structure of a 2DEG we describe the depletion of heterostructures by defects induced only at the surface. This is the underlying principle for the direct nanolithography, that is described in **Chapter 4**. The chapter starts with an introduction to the AFM as a tool for investigating surfaces. Afterwards, we describe the two AFM techniques used for the direct fabrication of the mesoscopic devices, namely the controlled nanomachining and the local oxidation. Of special interest is a comparison of diamond and silicon as tip materials for the nanomachining of ballistic quantum point contacts. The second part of the chapter reviews the creation

of tunnelling barriers with local oxidation. We discuss the influence of the writing parameters on the oxide growth at the surface of heterostructures. We show that the oxidation currents directly determines the depth of the oxide lines.

In **Chapter 5** we introduce the constant interaction model that is used to describe a single-electron transistor, consisting of a quantum dot with attached contacts and leads, in the Coulomb-blockade regime. The model is compared with the results obtained from a quantum dot defined with local oxidation. In the second part of the chapter we show the stepwise fabrication of a parallel double quantum dot by cutting a one-dimensional resonant tunnelling diode in quasi zero-dimensional regions.

Chapter 6 describes measurements on a very small quantum ring that was defined with local oxidation. We study the open transport regime where the electrons are transmitted ballistically through the ring structure. The ring acts as an interferometer and allows to observe the Aharonov-Bohm effect. With the attached in-plane gates we tune the phase of the electronic wave function inside the ring arms. The chapter ends with a short discussion of Fano-resonances in the conductance through the ring that might be caused by an interference of a resonant with a non-resonant transmitted state.

The thesis continues in **Chapter 7** with measurements on a quantum ring in the Coulomb-blockade regime. Of special interest is the Kondo effect that leads to a finite conductance even for a constant electron number on the ring. The non-linear transport measurements on the quantum ring exhibit clear indications for a Kondo effect induced by a single electron spin. The study of the addition spectrum in high magnetic fields enables us to extract the exact number of electrons on the ring in the Coulomb-blockade regime. Finally, we use the Kondo effect to study the evolution of the Aharonov-Bohm effect in the Coulomb-blockade valley.

A summary of the results is given in **Chapter 8**.

2 Low-dimensional electron systems

In this chapter we review the basic principles of low-dimensional electron systems. We discuss the density of states of two- and one-dimensional electron gases. An introduction to single-particle states in a zero-dimensional potential well follows. The result is compared to the magnetic field dependence of the ground state of a strictly one-dimensional quantum ring. In the second part of the chapter we describe two important transport phenomena for our thesis, namely ballistic conductance through quantum point contacts and tunnelling through potential barriers. The chapter ends with an introduction to lateral resonant tunnelling through a double-barrier structure.

2.1 Confined electrons

2.1.1 Two-dimensional electron gas

Electrons in a three-dimensional periodic potential can be described as plain waves with an energy

$$E(\vec{k}) = \frac{\hbar^2}{2m^*}(k_x^2 + k_y^2 + k_z^2) \ . \tag{2.1}$$

$\vec{k}$ is the wave vector of the electron. Its components $k_i = 2\pi/\lambda_i$ are the wave numbers and λ_i $(i = x, y, z)$ the wavelength in all three dimensions x, y, z. m^* is the so-called effective mass of the electrons that takes the specific band structure of the crystal into account. In general m^* is a tensor that is defined by the following expression

$$\left(\frac{1}{m^*}\right)_{ij} = \frac{1}{\hbar^2}\frac{\partial^2 E(\vec{k})}{\partial k_i \partial k_j} \ . \tag{2.2}$$

In a parabolic conduction band m^* will not depend on the energy of the electrons and

$$m^* = m^*_{xx} = m^*_{yy} = m^*_{zz} \ .$$

A two-dimensional electron system is created by applying an additional confinement potential $V(z)$ along the z-direction in a crystal. This leads to a quantization of the energy levels $E_z(n_z)$ where n_z is the number of the occupied levels. These levels will be named as subbands in the following. Instead of equation 2.1 we get

$$E(k_x, k_y, n_z) = \frac{\hbar^2}{2m^*}(k_x^2 + k_y^2) + E_z(n_z) \ . \tag{2.3}$$

Apparently, the electrons can only move freely in the xy-plane perpendicular to the potential $V(z)$. One possible experimental realization of a two-dimensional electron gas (2DEG) will be described in Chapter 3.1.

The density of states $D_{n_z}(E)$ in the specific subband n_z in a 2DEG does not depend on the energy

$$D(E) = 2\frac{L^2 m^*}{2\pi\hbar^2} \ ,$$

here we use $\hbar = h/2\pi$ with h Planck's constant and L the size of the system. The factor two considers the electron spin. $D(E)$ for a system with several occupied subbands is just the sum of the Heaviside function Θ

$$D(E) = \sum_i D_i(E) = \frac{L^2 m^*}{\pi\hbar^2} \sum_i \Theta(E - E_i) \ . \tag{2.4}$$

In the $\vec{k}$-space this system is a disc with a radius of $k_F = \sqrt{2\pi n_e}$ with n_e the density of the electrons in the 2DEG. k_F is defined as the wave number at the Fermi energy E_F at zero temperature. With this relation we get for the Fermi energy in a 2DEG

$$E_F = \frac{\pi\hbar^2}{m^*} n_e \ . \tag{2.5}$$

2.1.2 One-dimensional electron gas

With another confinement potential along the y-direction we can restrict further the free motion to the x-axis of the system. The energy of the electrons is then quantized in the y and z-direction

$$E(k_x, n_y, n_z) = \frac{\hbar^2 k_x^2}{2m^*} + E_y(n_y) + E_z(n_z) \ . \tag{2.6}$$

Each pair of n_y and n_z denotes a specific one-dimensional (1D) subband in this system. To simplify we assume for the following considerations that $n_z = 1$ and the number of the occupied 1D-subbands depends only on n_y. The density of states $D(E)$ has to be modified

$$D(E) = 2\frac{L}{\pi\hbar}\sqrt{\frac{m^*}{2E}} \ . \tag{2.7}$$

The main difference to the two-dimensional electron gas is that the density of states is proportional to $1/\sqrt{E}$ instead of constant. We will later see that this dependence has an important consequence for the transport through such an 1D-system.

2.1.3 Zero-dimensional systems

Spectrum of a quantum dot

With a third confinement potential $V(x)$ the electrons are bound to a quasi zero-dimensional region of space. If $V(x), V(y)$ and $V(z)$ are of the parabolic form the energy of the electron is quantized

$$E(n_x, n_y, n_z) = \hbar\omega_x(n_x + \frac{1}{2}) + \hbar\omega_y(n_y + \frac{1}{2}) + \hbar\omega_z(n_z + \frac{1}{2}) \tag{2.8}$$

with $n_i = 0, 1, 2, ..$ the number of occupied levels in each direction and $\hbar\omega_i$ the energy of the harmonic oscillator that denotes the separation of the levels ($i = x, y, z$). All energies are discrete and thus the electron is confined in the potential.

The density of states $D(E)$ in a 0D-system is the sum over Dirac δ-functions

$$D(E) \propto 2 \sum_{n_x, n_y, n_z} \delta(E - E(n_x, n_y, n_z)) \ . \tag{2.9}$$

The pre-factor considers the two-fold degeneracy of each state due to the electron spin.

In semiconductor physics such a system is often named quantum dot (QD) or even artificial atom because of the similarities with the energy spectrum of real atoms. In the following we neglect any influence of interaction effects by assuming only one confined electron in the system.

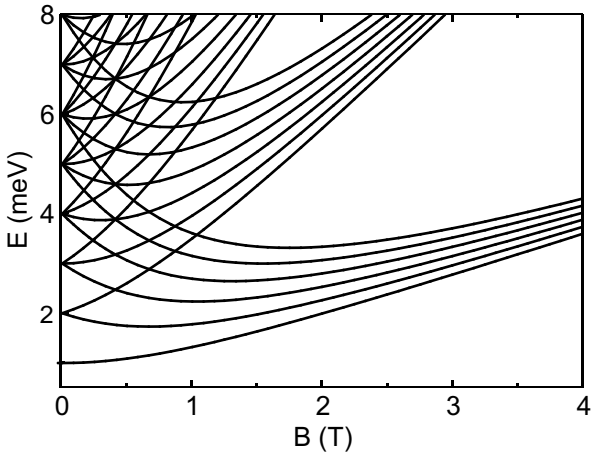

Figure 2.1: Magnetic-field dependence of the energy levels for one electron in a 2D parabolic confinement potential with $\hbar\omega_0 = 1$ meV. The Zeeman energy is neglected.

We can create a quasi disc-like quantum dot by choosing $\hbar\omega_z \gg \hbar\omega_{x,y}$. For simplicity we assume $\hbar\omega_x = \hbar\omega_y = \hbar\omega_0$ and separate the Hamiltonian $\hat{H}_g = \hat{H} + \hat{H}_z$. $\hat{H}$ is given by

$$\hat{H} = \frac{1}{2m^*}\hat{p}^2 + \frac{1}{2}m^*\omega_0^2 r^2 \ , \tag{2.10}$$

where $\hat{p}$ is the lateral momentum operator in the x, y-plane. Due to the radial symmetry of this Hamiltonian it can be solved in polar coordinates $\vec{r} = r\exp(i\varphi)$ which results in eigenvalues of the form

$$E(n, l) = (2n + 1 + |l|)\hbar\omega_0 \tag{2.11}$$

with the radial quantum number $n = 0, 1, 2, ..$ and the angular momentum quantum number $l = 0, \pm 1, \pm 2, .. .$ Please note, that in Cartesian coordinates $\vec{r} = (x, y)$ the ground state energy has the form $E(n_x, n_y) = \hbar\omega_0((n_x + 1/2) + (n_y + 1/2))$.

When we apply a magnetic field B perpendicular to the plane of the quantum dot the energy of the system has to be modified

$$E(n, l) = (2n + 1 + |l|)\sqrt{(\hbar\omega_0)^2 + (\hbar\omega_c/2)^2} + (l/2)\hbar\omega_c \ , \tag{2.12}$$

with the cyclotron frequency $\omega_c = eB/m^*$. This result first calculated by Fock [18] is obtained by neglecting the influence of the electron spin, which is reasonable for a system with only one electron.

The result of a calculation is shown in Figure 2.1. In the limit of very high magnetic fields, i.e. $\hbar\omega_c \gg \hbar\omega_0$, equation 2.12 can be rewritten in the following form

$$E(n,l) \approx (2n + 1 + (|l| + l)/2)\hbar\omega_c \ . \tag{2.13}$$

This result indicates the formation of Landau levels in the system at very high magnetic fields. In the spectrum of the quantum dot in Figure 2.1 this is visible by the "bunching" of the electron states for $B > 2$ T.

Spectrum of a quantum ring

These considerations are only valid for a quantum dot with a simple connected topology. The characteristic changes completely for a quantum ring with outer and inner boundary. In a model with a strictly one dimensional geometry which encloses a magnetic flux of m flux quanta $\phi_0 = h/e$ the energy spectrum $E_{l,m}$ of a single-mode ring can

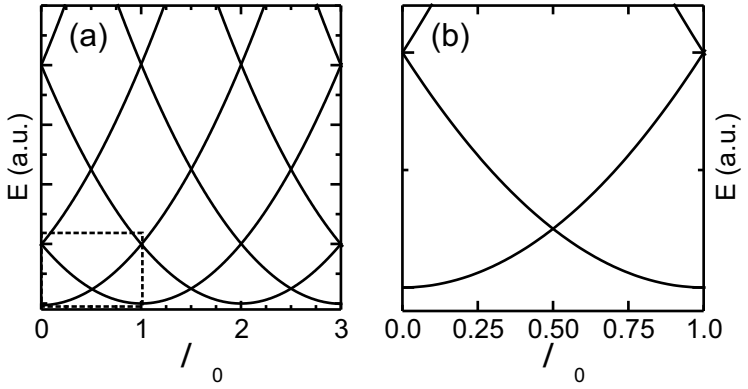

Figure 2.2: (a) Theoretical spectrum of a single mode one-dimensional quantum ring as a function of the applied flux ϕ. Each state follows a parabola with constant angular momentum quantum number $l = 0, \pm1, \pm2, .. \ .$ (b) Magnification of the region in the dashed box shown in (a).

be calculated to [19]

$$E_{l,m} = \frac{2\hbar^2}{m^* d_e^2}(m+l)^2 \ . \tag{2.14}$$

Here m^* is the effective mass of the electron, $l = 0, \pm 1, \pm 2, ..$ the angular momentum quantum number, and d_e the diameter of the ring.

For every value of l the states lie on parabolas with the minimum at a magnetic flux $\phi = m\phi_0$ as depicted in Figure 2.2(a). An increase of m by one leads to a change of the ground state of the ring from $l = 0$ to $l = -1$, see Fig.2.2(b). Therefore, the energy of the ground state is oscillating with a period of h/e in a perpendicular magnetic field even in a single-particle picture. This is in contrast to the results for the quantum dot. The ground state of a quantum dot is always $n = 0$ and $l = 0$, see Figure 2.1.

2.2 One-dimensional ballistic transport

One possibility to create a one-dimensional system is to cut a narrow wire out of a 2DEG. On the left-hand side of Figure 2.3 a schematic picture of a 1D-channel in a two-dimensional electron gas is depicted. The solid black lines indicate insulating regions separating the gates from the rest of the 2DEG depicted in grey. The density of the electrons in the constriction and thus the electronic width w_{1D} is controlled by the voltages applied to the gates. Such a device works in principle like a field-effect transistor that is laid out flat on a surface.

Inside a constriction in a 2DEG a quasi one-dimensional channel of length l_{1D} and width w_{1D} might be formed. In the following we assume that w_{1D} is smaller compared to all other quantities. The channel is directly coupled to the two-dimensional reservoirs. A qualitative microscopic picture is shown in Figure 2.3(a)+(b). The transport characteristic of such a system is classified in three different regimes: diffusive, quasi-ballistic, or ballistic [20].

The system is diffusive if the mean free path l_e of the electrons is smaller than the length of the channel: $l_e \ll l_{1D}$, Figure 2.3(a). l_e is governed by scattering of electrons on impurities (indicated by the grey circles in Figure 2.3(a)) or a rough surface of the channel boundaries. In a quasi-ballistic system l_e is larger than w_{1D} but still smaller than l_{1D}. When impurities are absent in the channel and its boundaries are smooth on the length scale defined by the Fermi wavelength of the

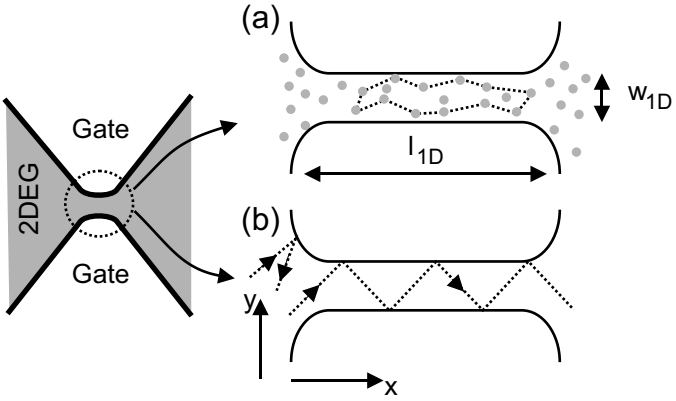

Figure 2.3: Microscopic picture of the channel between two gates: (a) diffusive transport regime ($l_e \ll l_{1D}$) (b) ballistic transport regime ($l_e \gg l_{1D}$).

electrons $l_e \gg l_{1D}$ follows. In this regime the electrons are ballistically transmitted through the channel and the scattering at the boundaries is specular, Figure 2.3(b). In other words, due to the absence of scatterers all electrons that enter the channel will be transmitted through it which results in a transmittance $\mathcal{T} = 1$ of the channel.

In our experiments we will define very short channels of a few ten nanometers length. These kind of devices are known as ballistic quantum point contacts (QPC).

We will calculate the conductance G through a QPC. In a ballistic regime, the conductance through a classical point contact was first derived by Sharvin [21]:

$$G = \frac{2e^2}{h}\frac{k_F w_{1D}}{\pi} = \frac{2e^2}{h}\frac{2w_{1D}}{\lambda_F} \ , \tag{2.15}$$

where $k_F = 2\pi/\lambda_F$ is the Fermi wave vector and λ_F the Fermi wavelength at E_F. The conductance is limited by scattering of the incident electrons at the entrance of the constriction and thus scales linearly with w_{1D}.

Quantum mechanical effects lead to deviations from a continuous dependence of G on w_{1D} when the Fermi wavelength λ_F of the electrons is comparable to the width of the point contact w_{1D}. As a consequence one obtains a quantized conductance. In a typical GaAs/AlGaAs-heterostructure used here we get $\lambda_F \sim 50$ nm, therefore the electronic width

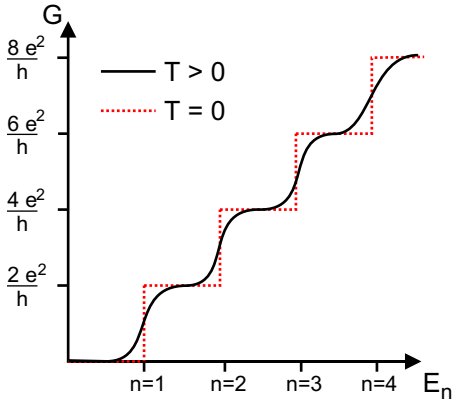

Figure 2.4: Conductance G of a ballistic quantum point as a function of the number of occupied subbands n at temperature $T = 0$ and $T > 0$.

of a quantum point contact should be smaller than a few 100 nm to observe quantization.

A simplified explanation for the quantization of G in units of $2e^2/h$ is the formation of discrete energy levels inside the quantum point contact that are accessible for transport. By assuming a harmonic confinement potential perpendicular to the current direction the eigenvalues of the energy in the quantum point contact have the form [20]:

$$E(k_x, n_y) = \frac{\hbar^2 k_x^2}{2m^*} + \left(n_y + \frac{1}{2}\right)\hbar\omega_0 \ , \qquad (n_y = 0, 1, 2, ..) \qquad (2.16)$$

which contains a free-electron kinetic energy in the longitudinal x-direction (parallel to the current flow). The energy levels are equally spaced with $\hbar\omega_0$. Since the electrons can only move freely in the x-direction this leads to quasi one-dimensional subbands. Each subband is characterized by a specific transmission coefficient $\mathcal{T}_n$. Electrons can only pass the point contact if their energy matches the energy of the occupied subbands in the QPC.

We calculate the net current I flowing through a point contact with N occupied subbands at zero temperature. I is obtained by integrating over all electronic states between the electrochemical potentials of the

source and drain contacts μ_S, μ_D:

$$I = e \sum_{n=1}^{N} \int_{\mu_D}^{\mu_S} dE \frac{1}{2} \frac{dN_n}{dE} v_n(E) \mathcal{T}_n(E) \ . \tag{2.17}$$

Again $\mathcal{T}_n$ is the transmission probability of each subband that is accessible for the electrons. The product of the 1D-density of states $dN_n/dE = 2/\pi \cdot (dE_n/dk_x)^{-1}$ and the velocity of the electrons $v = 1/\hbar \cdot (dE_n/dk_x)$ yields $(dN_n/dE_n) \cdot v_n = 4/h$. Formula 2.17 is simplified with this result and we calculate the conductance $G = I/V$ of the QPC to

$$G = \frac{2e^2}{h} \sum_{n=1}^{N} \mathcal{T}_n \ , \tag{2.18}$$

which is the so-called two-terminal Landauer-formula. In the ballistic regime the transmission probability is $\mathcal{T}_n = 1$ for $n = 1..N$ with N the maximum number of populated subbands. According to these considerations the conductance G is quantized

$$G = \frac{2e^2}{h} N \ . \tag{2.19}$$

The above considerations are valid at zero temperature ($T = 0$) and lead to sharp steps in the conductance G through a QPC as a function of the number of occupied subbands as shown in Figure 2.4 by the dashed line. At finite T the steps are smeared out because of the Fermi-Dirac distribution of the electrons in the contacts given by

$$f(E) = \frac{1}{\exp\left(\frac{E - E_f}{k_B T}\right) + 1} \ , \tag{2.20}$$

with k_B the Boltzmann constant. An ideal characteristic at finite temperature is shown by the solid line in Figure 2.4.

Scattering in the quantum point contact, either at rough boundaries or impurities, lead to deviations from the ballistic case. If defects are present in the constriction the $\mathcal{T}_n$ of the subbands will differ. This will distort the characteristic and the clear quantization of the conductance is lost.

2.3 Tunnelling phenomena in low dimensional systems

After this short introduction to one-dimensional ballistic transport we introduce the tunnelling through potential barriers.

2.3.1 Tunnelling barriers

A potential or tunnelling barrier is described by its energetic height Φ_0 and the width w. A simple idealized example is shown in Figure 2.5. A rectangular tunnelling barrier separates a continuum of electronic states that contain electrons up to the electrochemical potential μ indicated by the grey region, depicted at zero temperature $T = 0$ K. In a classical picture all incident electrons with a certain energy $E < \Phi_0$ are reflected at the barrier. Classical particles can only pass the barrier when their energy exceeds Φ_0. In contrast, the quantum mechanical calculation of the transmission coefficient t results in $t > 0$ for a barrier with finite height even for electrons with $E < \Phi_0$: the electrons can tunnel through the barrier. The calculation of t in dependence of Φ_0 and w yields for $E < \Phi_0$ [22]:

$$t \propto \exp\left(-w\sqrt{\frac{2m^*}{\hbar^2}(\Phi_0 - E)}\right) \quad . \tag{2.21}$$

This result is only valid if the wavelength of the electrons λ is much shorter than the barrier width.

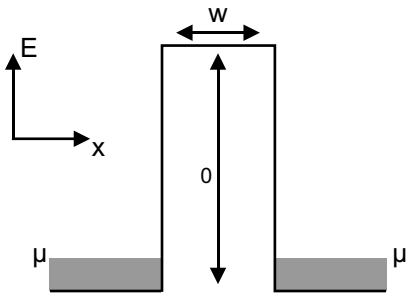

Figure 2.5: Idealized tunnelling barrier shown for an electrochemical potential $\mu \ll \Phi_0$ in the contacts.

We are interested in the current-voltage (IV) characteristic of a *real* tunnelling barrier as shown in Figure 2.6(a). In our case, a real barrier situated in a realistic semiconductor will be distorted compared to Figure 2.5 because free electrons will screen the potential. This leads to an effective rounding of the barrier shape. This can be simulated by self consistent calculations. Examples for real barriers in a two-dimensional electron gas can be found e.g. in the work of Peck [23].

A real barrier with different applied bias voltages is shown in Figure 2.6. At zero bias ($V_{SD} = 0$), the electrochemical potentials μ_s, μ_D in the source and drain contacts are equal, Figure 2.6(a). By raising V_{SD} ($\mu_S > \mu_D$) a current will start to flow eventually through the barrier, because empty states exist on the other side of the barrier, Figure 2.6(b).

There is an additional effect for the real barrier: its effective height Φ^{eff} above the electrochemical potential in the source contact μ_D is reduced by an amount $\Delta\Phi = \alpha e V_{SD}$ with e the elementary charge and α a voltage-to-energy conversion factor. In general, the voltage drop over the barrier will be linear and in the case of a symmetrical barrier it follows $\alpha = 0.5$. This is depicted in Figure 2.6(b). For an asymmetric barrier α will be smaller than 0.5.

With even higher V_{SD}, Φ^{eff} is further reduced (Figure 2.6(c)) and the tunnelling current grows accordingly. If Φ^{eff} falls below zero, the barrier is reduced to an Ohmic resistor with a resistance $R = dV_{SD}/dI_{SD}$, and the current grows according to Ohm's law $I_{SD} = V_{SD}/R$ linearly for $eV_{SD} \gg \Phi_0$, Figure 2.6(d).

The resulting IV-characteristic is shown in Figure 2.7 for two symmetric tunnelling barriers with the same width but different heights Φ_0 as shown in the upper left inset. The dashed line depicts the characteristic for the higher barrier, in which the tunnelling current is suppressed over a wide voltage range around $V_{SD} = 0$. In this region I_{SD} is too small to be detected with our measurement setups. This is different for the smaller barrier because here a detectable tunnelling current flows already around $V_{SD} = 0$ (solid line in Figure 2.7). Φ_0 can be estimated by extending the linear region of the characteristic to $V_{SD,0}$ at $I_{SD} = 0$, as indicated in the lower right inset of Figure 2.7. For a symmetrical tunnelling barrier ($\alpha = 0.5$) $V_{SD,0}$ will be identical for both bias directions and thus

$$\Phi_0 = 0.5 e V_{SD,0} \ . \tag{2.22}$$

This is a very simplified method for the estimation of Φ_0. For an exact

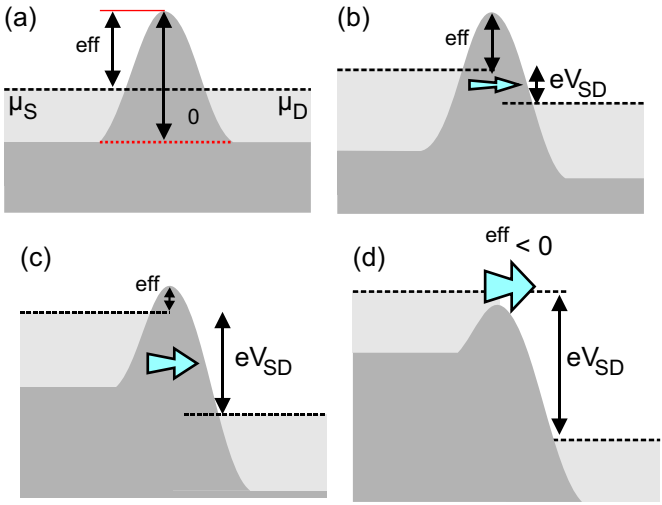

Figure 2.6: Tunnelling current through a barrier at different source-drain bias V_{SD}. The effective barrier height Φ^{eff} and Φ_0 change both with variation of V_{SD}.

determination of α and Φ_0 temperature dependent measurements of the tunnelling current are required, see e.g. Ref. [24].

2.3.2 2D-1D-2D resonant tunnelling

In Chapter 2.2 we discussed the transport features through a 1D-system in the ballistic regime. What happens if we couple a one-dimensional system like a quantum wire with two tunnelling barriers to a 2DEG ?

A schematic picture of such a device is shown in Figure 2.8(a). The tunnelling barriers that establish the tunnel coupling and define the 1D-wire are depicted. The length of the wire is determined by the width of the 2DEG itself. $\mu_{S,D}$ denote the electrochemical potential in the source and drain contacts. A system with two consecutive barriers is often named double-barriers structure. The one-dimensional wire in between may contain several energy levels depending on the barrier heights and the barrier separation, here we depicted two levels indicated by the horizontal lines.

This device is a 2D-1D-2D resonant tunnelling diode (RTD). Such a RTD has similar properties as vertical 3D-2D-3D RTDs that were first

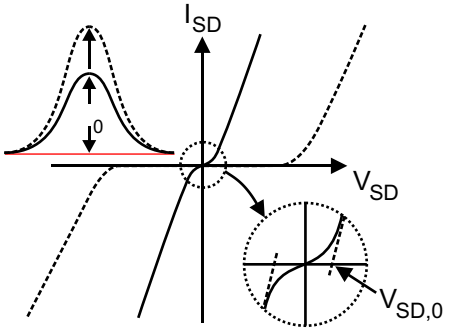

Figure 2.7: IV-characteristic of two tunnelling barriers with different height Φ_0.

demonstrated experimentally in 1974 by Chang, Esaki, and Tsu [25].

In Figure 2.8(b)+(c) a sketch of a RTD with an applied bias voltage V_{SD} is shown that induces a difference of the electrochemical potentials $\mu_S - \mu_D = eV_{SD}$. For the flow of a tunnelling current, energy and momentum of the electrons have to be conserved and there have to be free states across the barriers. Therefore, electrons can only tunnel if their energy in the x-direction matches the energy of the subband E_0 between the double barriers: $\hbar^2 k_x^2/2m^* = E_0$, with m^* as the effective mass of the electrons in the material. In Figure 2.8(a) tunnelling is forbidden, because $k_F = \sqrt{2m^*\mu_S/\hbar^2} < k_0$ as depicted in the graph on the right-hand side. Please note, that in two dimensions there is only a Fermi circle with radius k_F in the k_x, k_y-plane.

The position of the subband relative to the electrochemical potential can be controlled with the bias voltage V_{SD}. With a voltage-to-energy conversion factor $\alpha \sim 0.5$ for a symmetric structure we calculate the energy of the subband E_r relative to the band edge of the emitter

$$E_r = E_0 - \alpha e V_{SD} \ .$$

At V_T applied to the structure, E_r matches μ_S and k_r if shifted into the Fermi circle. All the electrons with a wave vector that ends on the vertical line at k_r in Figure 2.8(b) can pass the structure resonantly. The number of electrons that may tunnel depends on the length of the segment and with increasing V_{SD} there are more states available. Therefore, the current I will grow accordingly. This continues until E_r falls below the conduction band edge in the emitter. At this point there is a sharp drop in I, because electrons with a $k_r < 0$ are no longer

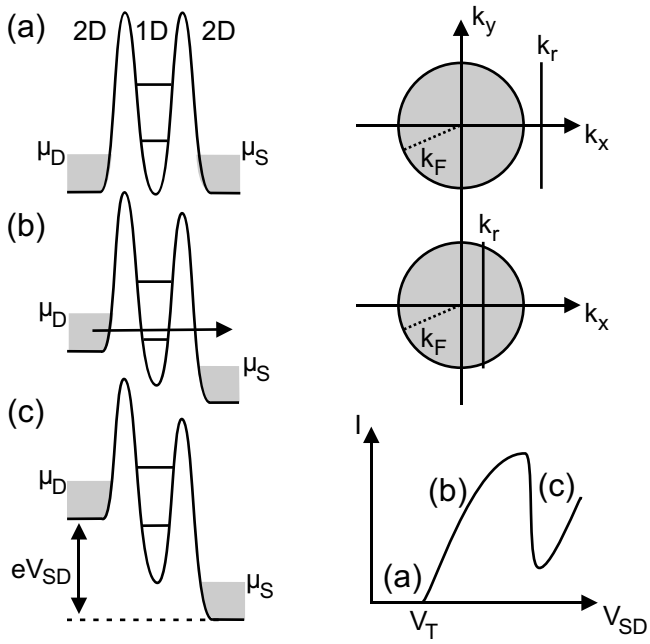

Figure 2.8: (a)-(c) Sketch of a 2D-1D-2D resonant tunnelling diode with varying bias voltage V_{SD}. On the right hand side the Fermi circle is shown with the resonant level at k_r. Lower right: resulting IV-characteristic.

transmitted. This leads to a peak in the IV-characteristic of every resonant tunnelling device as indicated in the lower right picture in Figure 2.8. At the sharp break down of the current there is a negative-differential resistance (NDR), which is especially interesting for high-frequency devices [26].

3 Depletion of a two-dimensional electron gas

In this chapter we describe the basis for all our experiments, namely two-dimensional electron gases (2DEG) in GaAs/AlGaAs-heterostructures. We give a detailed overview about the three specific heterostructures used for fabricating mesoscopic devices.

In the second part we introduce the underlying principle of direct writing of electronic structures with an atomic force microscope. For one of the heterostructures we discuss the possibility of the controlled depletion of a 2DEG.

3.1 Heterostructures

The starting point for all the experiments in this thesis are two dimensional electron gases (2DEG). In Chapter 2.1.1 the basic properties of 2DEGs are described. In the following paragraph an experimental realization in a semiconductor crystal is discussed.

One possibility to fabricate a semiconductor heterostructure is the growth by molecular-beam epitaxy (MBE). In general, a heterostructure consists of two or more semiconductors with different band gaps, which are combined in a single crystal. With a correct layer and doping sequence one can create e.g. a triangular potential well along the growth direction below the surface. The structure contains a two-dimensional electron gas at liquid ^{4}He-temperatures of 4.2 K. The electrons are confined within the potential and can only move in the plane perpendicular to the growth direction.

GaAs and AlGaAs are ideal candidates for the fabrication of heterostructures, because they have almost the same lattice constants but different band gaps: $a_{\mathrm{GaAs}} = 5.6533$ Å and $a_{\mathrm{AlAs}} = 5.6611$ Å, [27]. The AlGaAs material system is preferred especially for the band-gap engineering of 2DEGs for research applications because the band gap of the ternary semiconductor $\mathrm{Ga}_{1-x}\mathrm{Al}_x\mathrm{As}$ depends on the Al-content.

In the schematic picture in Figure 3.1 the formation of a 2DEG in a GaAs/AlGaAs-heterostructure is shown. An intrinsic semiconductor like GaAs with the Fermi energy E_F in the middle of the band gap between the valence band E_V and the conduction band E_C is shown. It is brought into contact with a doped semiconductor with larger band gap like AlGaAs. In equilibrium, E_F has the same value throughout the whole crystal and the band structure aligns itself self consistently. At the interface there is a discontinuity in the conduction and the valence band. The conduction band of the intrinsic semiconductor is bent down and the conduction band of the doped material is bent up (lower part of Figure 3.1). This leads to the formation of the triangular potential well with quantized energy levels, often named as subbands. By choosing a suitable doping concentration only the lowest subband is occupied.

In general, there are two different approaches for the doping of GaAs/AlGaAs-heterostructures. One possibility is the bulk modulation doping where several 10 nm AlGaAs are doped with e.g. Si with a typical concentration of about 10^{18} m^{-3}. In contrast, wafers with a δ-doping contain a layer of Si-donors with a thickness of only a few Å sandwiched between two adjacent AlGaAs layers. The advantage of both heterostructures is the spatial separation of the electrons from the positively charged donors. This reduces the main scattering process at low temperatures, which limits the mobility of the electrons, namely the remote impurity scattering. Today, with the advancement of the MBE-techniques it is possible to produce 2DEGs with exceptional high

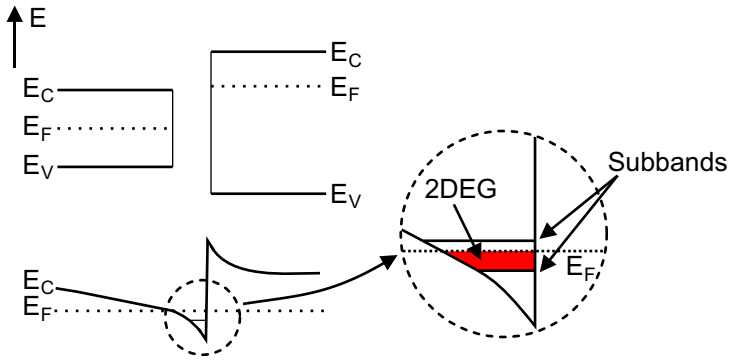

Figure 3.1: Formation of a triangular potential at the interface of two semiconductors with different band gaps.

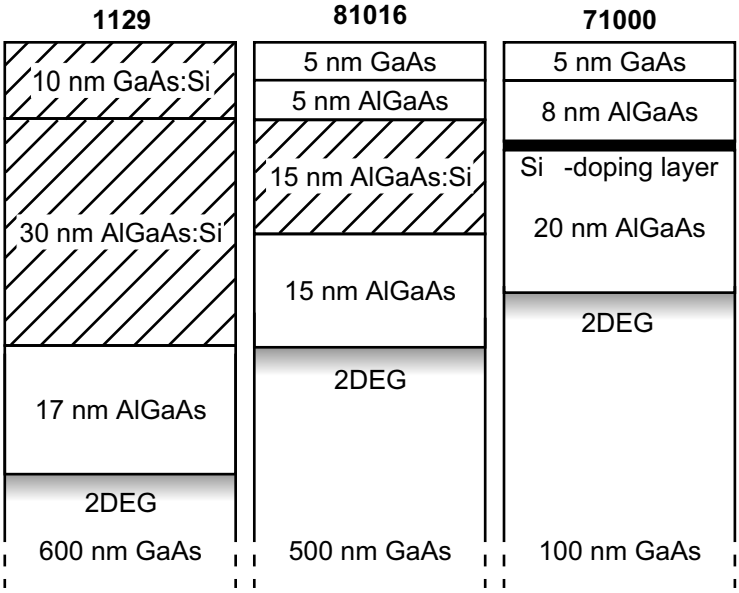

Figure 3.2: Layer sequence of the wafers: 1129, 81016, and 71000. The Silicon modulation-doped regions are marked with stripes. Please note the δ-doping layer of wafer 71000.

electron mobilities of more than 3000 $m^2V^{-1}s^{-1}$.

We use three different types of GaAs/AlGaAs-heterostructures in this work. Two of them are modulation doped heterostructures: the material 1129 was fabricated at the Lehrstuhl für Angewandte Physik at the Ruhr-Universität Bochum. Wafer 81016 was grown at the Max-Planck-Institut für Festkörperforschung in Stuttgart. The material system 71000, a very shallow 2DEG with δ-doping, was provided by the Walter Schottky Institut, München. All three layer sequences are

	1129	81016	71000
Electron density n_e (m^{-2})	$4.07 \cdot 10^{15}$	$4.0 \cdot 10^{15}$	$4.3 \cdot 10^{15}$
Electron mobility μ_e ($m^2V^{-1}s^{-1}$)	107	23.0	42.1
Distance 2DEG - surface (nm)	~ 57	~ 40	~ 34

Table 3.1: Characteristic values of the three heterostructures 1129, 81016, and 71000 at $T = 4.2$ K.

shown in Figure 3.2. The distance between the surface and the 2DEG is 57 nm (1129), 40 nm (81016), and 34 nm (71000), respectively. The main characteristics of the substrates are summarized in Tab. 3.1.

3.2 Local depletion of heterostructures

In this thesis we will use the tip of an atomic force microscope (AFM) for the direct manipulation of the electronic structure in a two-dimensional electron gas inside a GaAs/AlGaAs-heterostructure. The actual techniques for the direct nanolithography will be described in the next Chapter 4. At this point we give a short introduction to the underlying principle.

The band structure inside a GaAs/AlGaAs-heterostructure is very sensitive to changes at the sample surface, especially the shallow 2DEGs used here. As an example we want to demonstrate the influence of a groove in the sample surface on the band structure of the wafer 81016. In the following "band structure" means the edge of the conduction band in the sample parallel to the growth direction.

In Figure 3.3(a) the layer sequence of wafer 81016 is shown. For an undisturbed surface we calculated the band structure of this wafer with

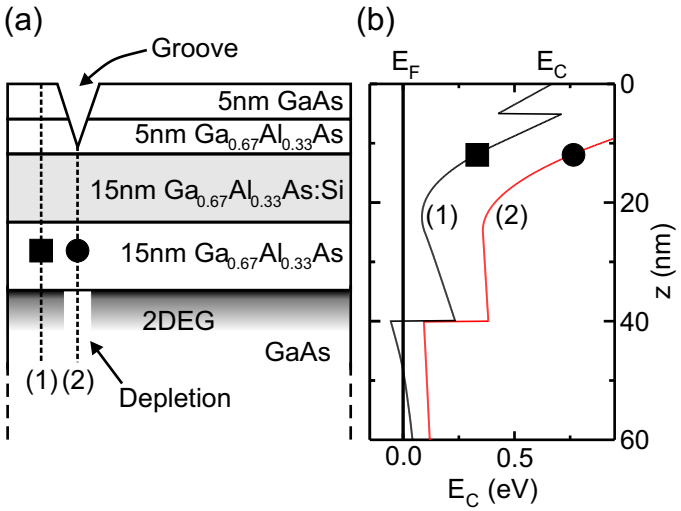

Figure 3.3: (a) Layer sequence of wafer 81016 with a 9 nm deep groove. (b) Simulated band diagram without ■ and with • the groove.

a self-consistent Poisson solver [28]. The result is depicted by the black line marked with a square in Figure 3.3(b), the edge of the conduction band is shown. Because the minimum of the band structure lies below E_F, a 2DEG is formed inside the triangular potential well.

To deplete the 2DEG, we can use a characteristic of the GaAs. At the surface the Fermi energy E_F is pinned near the middle of the band gap of GaAs due to the formation of surface states. By removing a small amount of material from the surface e.g. by scribing a groove with an AFM tip. This moves the interface closer to the 2DEG and because of the pinning of E_F in the band-gap the triangular potential well is lifted above E_F and the 2DEG is depleted.

As an example for this process, we calculate the band structure of wafer 81016 again with a groove that protrudes 9 nm into the sample, shown by the white triangular area in Figure 3.3(a). As already mentioned the minimum of the band structure is shifted above E_F and the 2DEG contains no longer any electrons. This process is similar to a shallow etch process [29]. For this example, the simulation results in a conduction band some 100 meV above E_F (curve (2) in Figure 3.3(b)). The raising of the conduction band underneath the defect is very sensitive to the depth. This was shown in several studies [30, 24] and will be used later in this thesis (see Chapter 4.3) to produce tunnelling barriers with varying height in a well defined manner.

It is important to notice that the influence is only local underneath the groove. As a consequence, it is possible to write insulating regions directly into a 2DEG with a resolution depending only on the width and the depth of the structures created at the surface. Another advantage is the spatial separation between the defect and the 2DEG. This avoids the creation of additional inhomogeneities in the 2DEG, because the "defect" is situated only at the surface.

3.3 Conclusion

In this chapter we described the details of the GaAs/AlGaAs-heterostructures used in this thesis. With self-consistent calculations we explained the depletion of the 2DEG inside a heterostructure by removing material from the surface. This is the underlying principle for fabricating of mesoscopic devices with an atomic force microscope. In the following chapter we give a detailed description of the processing of the samples.

4 Nanolithography with an atomic force microscope

The atomic force microscope (AFM) is a powerful tool for producing mesoscopic devices directly in GaAs/AlGaAs-heterostructures. We introduce two different fabrication techniques in which the tip of an AFM is used for manipulating of the surface.

In the first part of this chapter we describe the controlled nanomachining. The AFM tip is used as an engraving tool for a controlled creation of grooves in surfaces of GaAs/AlGaAs-heterostructures. The two-dimensional electron gas underneath a groove is depleted and thus we can directly write insulating regions into the electronic system. We use this technique for fabricating ballistic quantum point contacts.

An alternative approach is the local oxidation of a surface induced by a negative voltage on a conducting AFM tip. This allows the production of tunnelling barriers in the 2DEG of a heterostrcuture in a controlled manner. We study the dependence of the oxide growth on the writing parameters like tip velocity, relative humidity and the oxidation current. The chapter ends with a comparison of both techniques.[1]

[1] Parts of this chapter are published in: E. Oesterschulze, A. Malavé, U. F. Keyser, M. Paesler, and R. J. Haug, *Diamond cantilever with integrated tip for nanomachining*, Diamond and Related Materials **11**, 667 (2002). The main part of this work is published in J. Regul, U. F. Keyser, M. Paesler, F. Hohls, U. Zeitler, R. J. Haug, A. Malavé, E. Oesterschulze, D. Reuter, and A. D. Wieck, *Fabrication of quantum point contacts by engraving GaAs/AlGaAs heterostructures with a diamond tip*, Applied Physics Letters **81(11)**, 2023-2025 preprint: cond-mat/0202402.

4.1 Scanning probe microscopy

The invention of the scanning tunnelling microscope (STM) [3] and the atomic force microscope (AFM) [5] was followed by a fast development of new techniques for the imaging of surfaces like e.g. magnetic force and friction measurements. Scanning probe microscopes (SPM) are used in all fields of research, ranging from semiconductor physics to life sciences. The idea for all SPMs is very simple: a sample is put onto a piezo-resistive crystal that is deformed with sub-Ångstrom accuracy in all three dimensions by applying a voltage for each direction [31]. In combination with SPM-tips that have a single atom at the tip-apex it is possible to investigate single atoms or molecules on all kinds of surfaces with different methods [32].

The various SPMs differ by the parameter used for the detection of the tip-sample distance. For the operation of the STM a small voltage is applied between the tip of the microscope, and the sample and the tunnelling current is measured. Because this current is very sensitive to the tip-sample distance it can be used as a feedback parameter to obtain topographic images. However, the requirement of the tunnelling current limits the STM to conducting surfaces.

This major drawback was overcome with the invention of the atomic *force* microscope (AFM). The main difference between the STM and the AFM is the parameter used for measuring the tip-sample interaction. An AFM operates in the following way: the AFM tip is in direct contact with the sample and measures the force between sample and tip. Compared to the STM, this alternative approach to the feedback is a major advantage for the AFM and enables the investigation of all kinds of materials ranging from insulators to living cells. Due to these capabilities the AFM became one of the most important tools for the analysis of surfaces in research and industrial applications.

Contact mode

There are several different imaging modes to investigate a surface with an AFM tip. In this thesis we are using the so-called contact mode which is explained in this paragraph. The contact mode is used to obtain a picture of sample surface and also for nanolithography described as well.

A schematic picture of an AFM is shown with its important building blocks in Figure 4.1. The AFM tip itself consists of a cantilever that

supports the tip. The cantilever is connected to a bulk region needed for the handling of the AFM tips with tweezers. Normally the whole system consisting of tip, cantilever, and bulk, is fabricated of the same material, commonly silicon. In a simple picture, the cantilever is described as a leaf spring with a characteristic spring constant k. In the contact mode, a contact force F_C is applied between the tip and the surface during the scanning of the surface with a xyz-piezo-resistive crystal (*abbreviation: piezo*). A simple idealized picture of this process is shown in Figure 4.1. With the spring constant k of the cantilever the force F_C is easily calculated with Hooke's law: $F_C = k\Delta z$, where Δz is the deflection of the cantilever out of equilibrium. The AFM feedback loop measures the contact force between the tip and the surface with the help of a laser that is focused onto the cantilever. The laser beam is reflected at the cantilever top and shines onto a photo detector. The deflection and thus the change of the contact force is monitored by measuring the voltage variation dV at the detector, Figure 4.1. The height information is obtained by recording the voltages applied to the z-piezo, which are needed to keep the signal of the photo detector constant. Finally, the sample topography is visualized by converting the voltage applied to the z-piezo into height information dz and plotting the data array in a color-coded image.

The idea to keep F_C minimal and constant reduces the probability to damage the sample by an AFM tip, which is usually harder than the

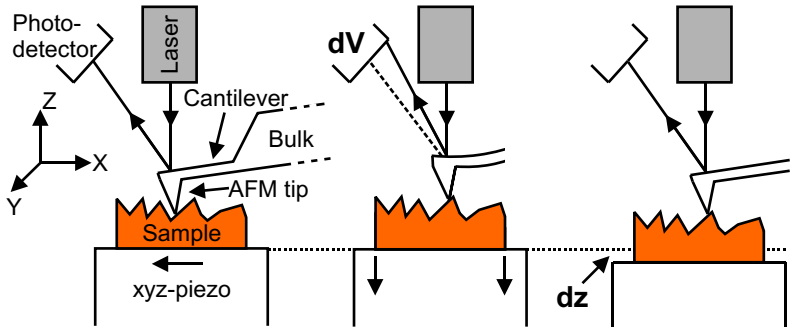

Figure 4.1: Schematic drawing of an AFM consisting of the tip, xyz piezo-resistive crystal, photo detector, and laser. From left to right: When the deflection of the cantilever and thus the contact force changes, the crystal is moved by dz to compensate for the voltage difference dV at the detector.

substrate. When the force constant of the cantilever is exactly known, the AFM can be used to detect ultra-low forces in the range of 10^{-18} N or less [33]. These capabilities enabled to investigate e.g. the Casimir force between an AFM tip and a surface [34].

4.2 Nanomachining of quantum point contacts

4.2.1 Controlled nanomachining of heterostructures

We use the tip of an AFM as nanolithographic tool for engraving grooves into the surface of a GaAs/AlGaAs-heterostructure. This removal of material is the most direct approach to the manipulation of surfaces. This technique is also known as mechanical nanomachining and was demonstrated by several groups on polymer films [35], Langmuir-Blodgett films [36, 37], metals [38] and oxides [39]. The first experiments to modify the electronic structure of a metal film were done by Wendel *et al.* [40].

The nanomachining was also applied on a variety of relatively hard semiconductor surfaces [41, 42, 43, 7]. For this technique it is essential to use a tip consisting of a material with a higher hardness than that of the substrate. An AFM tip will protrude into the surface and create a hole when we apply a high contact force of several μN. This will lead a pressure of several GPa at the tip apex due to the small tip radius, which lies around 10 nm for standard commercial tips. This is depicted schematically in Figure 4.2.

When the AFM tip is scanned over the surface with such high contact forces we can create grooves or lines with any desired geometry, e.g. on the surface of a GaAs/AlGaAs-heterostructure. In Chapter 3.2 we already mentioned that a groove in a heterostructure is one possibility to deplete the two-dimensional electron gas (2DEG).

The big advantage of the AFM is the small tip radius which allows a line width to below 50 nm of an engraved line [44]. In principle the minimal width of the groove depends only on outer experimental parameters like e.g. the radius of the tip, the angle at the tip apex, the contact force, and the number of times writing the same structure with the tip.

A depletion of the 2DEG should result in an increase of the resistance of the 2DEG. Thus we can control the engraving process with the mea-

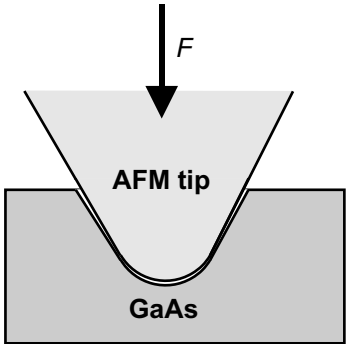

Figure 4.2: Mechanical nanomachining of GaAs with an AFM tip.

surement of the 2DEG resistance R during the nanomachining. It was shown that the room temperature resistance R of AFM-created lines directly determines the low-temperature characteristic [7]. It turned out, that a 2DEG is completely cut for $R > 1$ MΩ and shows a wide region of suppressed current with a very high tunnelling resistance of more than 50 GΩ at $T < 4.2$ K. The breakdown voltage of these high tunnelling barriers lies typically above $V = \pm 3$ V. This characteristic makes them ideally suitable for the definition of gates for mesoscopic devices.

A schematic picture of the measurement setup for the controlled nanomachining is shown in Figure 4.3. The AFM tip is scanned perpendicular over a Hall bar and depletes the 2DEG. The process is monitored with Keithley 2000 multimeter, which measures the resistance *in situ* during nanomachining the line. The AFM laser is disabled

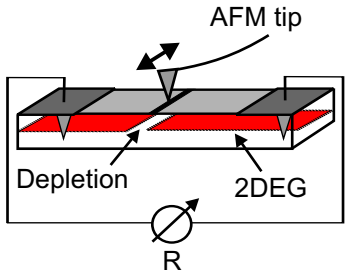

Figure 4.3: Schematic picture of the measurement setup for the controlled nanomachining. The 2DEG is depleted underneath the groove.

with a relay during the lithography to suppress the generation of carriers in the sample that would hinder the resistance measurement. If R exceeds some MΩ the scribing is stopped.

The fabrication of in-plane gates and single-electron transistors with this controlled nanomachining of GaAs/AlGaAs-heterostructures was recently shown [7, 45]. In this thesis we use this technique exclusively for the nanomachining of in-plane gates with very high tunnelling resistance.

4.2.2 AFM tips and samples

For the experiments presented here we use standard silicon tips fabricated by Nanosensors and new all-diamond AFM tips. Both types of tips have a relatively high force constants of more than 40 N/m. The diamond-tips were grown by hot-filament chemical vapor deposition of polycrystalline diamond onto a prepatterned silicon substrate. A scanning electron microscope (SEM) image of an all-diamond tip is shown in Figure 4.4. Please note, that all components (cantilever, tip, bulk) consist of diamond which is very unusual. Despite the rough surface, the tip radius is still smaller than 50 nm. A magnification of a tip apex is shown in the upper right inset in Figure 4.4. Please note the different length scale of the pictures. Despite the rough surface there are some very sharp peaks, which form the active tip used for the nanomachining.

More details on the recently developed fabrication technique for these all-diamond tips can be found in Ref. [46].

The samples used for this experiment are based on a modulation doped GaAs/AlGaAs-heterostructure containing a two-dimensional electron gas (2DEG) 57 nm below the sample surface with a sheet density of 4.07×10^{15} m^{-2} and a mobility of 107 m^2/Vs (wafer 1129, see Chapter 3.1). We fabricated Hall bar geometries with standard photo lithography, wet-chemical etching, and alloyed Au/Ge-contacts. A detailed description of these standard processing steps can be found e.g. in Ref. [47]. Afterwards the samples were bonded and mounted into the AFM for the controlled engraving process.

Comparison of silicon- and diamond-tips for nanomachining

For the controlled nanomachining the AFM tip is repeatedly scanned over the Hall bar with a scanning speed of 0.1 mm/s and a contact

force of several ten μN. The total depopulation of this specific 2DEG is marked by an abrupt raise of the sample resistance to more than 3 MΩ.

For comparison, two typical resistance curves monitored during the fabrication of an insulating line with a diamond and a silicon tip are depicted in Figure 4.5(b). We applied a contact force of about 50 μN for both experiments. The scribing of the lines was stopped when the resistance R exceeded 3 MΩ. In Figure 4.5(b) R is plotted as a function of the number of scan lines N_{Scan} for the silicon tip (dashed line) and the diamond tip (solid line). With the Si-tip we have to repeat the scribing for at least 40 times before the total depletion of the 2DEG is accomplished. The onset is marked with an arrow in Figure 4.5. With the all-diamond tip the depletion of the 2DEG is achieved already within one single scan over the Hall bar.

Figure 4.6(a) shows an AFM image of a typical insulating engraved line on a GaAs/AlGaAs- heterostructure that was scribed with a Si-tip with the same parameters as described above. For this example the tip was scanned $\sim$ 100 times over the surface to get an insulating line. The resulting line has a width of 250 nm. The depth $z \sim 9$ nm suffices for the total depletion of the 2DEG underneath the groove for this heterostructure.

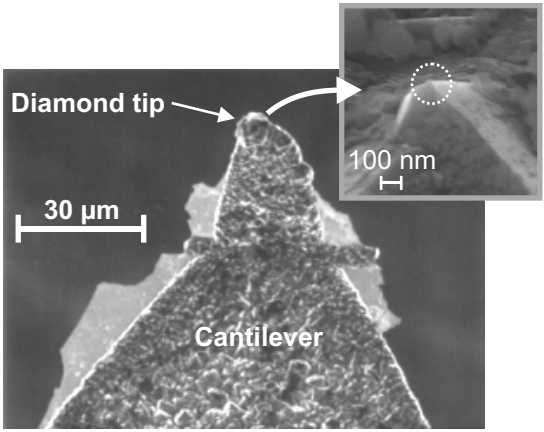

Figure 4.4: Scanning electron microscope image of an all-diamond AFM tip. The inset shows a magnification of the tip that has a radius smaller than a few ten nanometers (indicated by the circle).

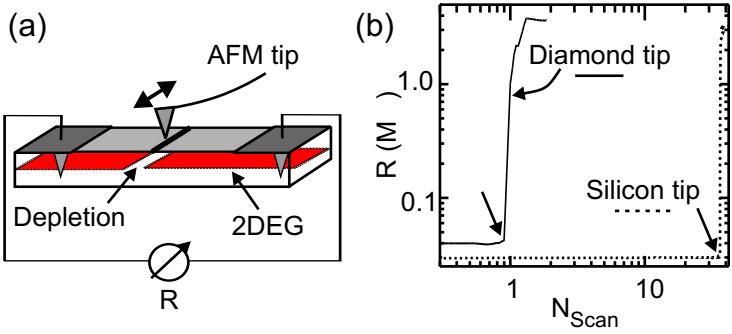

Figure 4.5: (a) Measurement setup for the controlled nanomachining of heterostructures. (b) Sample resistance R as a function of the number of scans N_{scan} during the fabrication of insulating lines with a diamond tip and a silicon tip (dashed line).

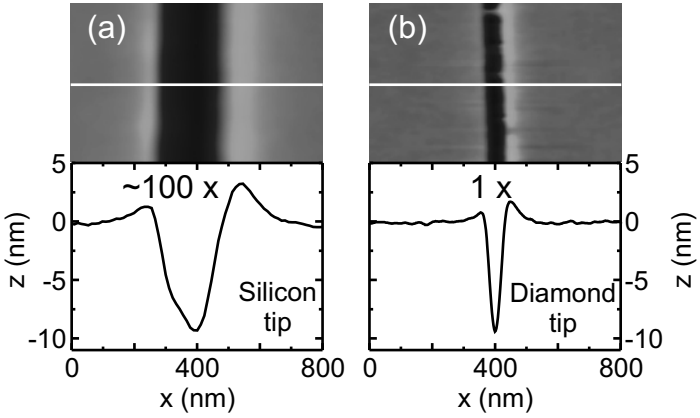

Figure 4.6: Results of the engraving with (a) a silicon tip and (b) a diamond tip. Upper part: AFM micrograph of the grooves. Lower part: depth profile along the white lines. (a) After ∼100 scans with a silicon tip, (b) after one scan with a diamond tip.

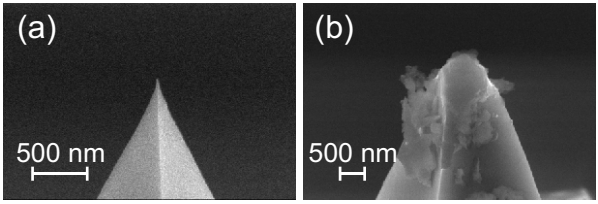

Figure 4.7: SEM image of a silicon AFM-tip before (a) and after (b) the nanomachining, the picture is taken from Ref. [24]. Please note the different length scales.

We achieve much narrower lines of 90 nm width and the same depth $z \sim 9$ nm by using an all-diamond probe as shown in Figure 4.6(b). The displayed groove was manufactured by scanning a diamond tip similar to that shown in Figure 4.4 once over the surface with a similar contact force as for Si. Compared to the former results in Figure 4.6(a) the processing time for e.g. a 100 μm line is substantially reduced by nearly two orders of magnitude from minutes to a few seconds. The reduction of the line width from 250 nm to 90 nm is mainly explained by the severe tip wear of the Si-tip during the writing process. After the engraving we measured the radius of the Si-tip and the diamond-tip by scanning electron microscopy (SEM). Whereas the Si-tip radius increased by at least a factor of 10 to more than 100 nm [24], Figure 4.7, images of the diamond tips yielded an unchanged radius of below 50 nm before and after the fabrication.

As expected the tip wear for diamond is almost negligible. In fact, we used this diamond tip for the fabrication of more than 40 devices without any observation of tip degradation. In contrast, a silicon tip can only be utilized once in most cases.

Comparison of the transport measurements

For comparison of the electronic properties of insulating lines fabricated by the different tips we defined two short one-dimensional channels by engraving constrictions into the GaAs/AlGaAs-heterostructure. The regions separated from the constriction by an insulating groove serve as in-plane gates. In the upper left inset of Figure 4.8 an AFM image of the completed structure is shown, which was written with a Si-tip. The sample engraved with the all-diamond tip is depicted in the upper left inset of Figure 4.9.

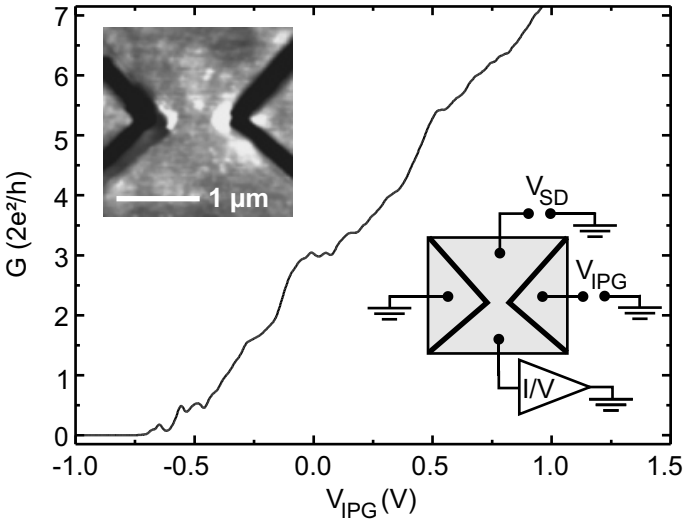

Figure 4.8: Conductance G of the QPC nanomachined with a silicon tip as a function of one in-plane gate voltage. The upper left inset shows an AFM micrograph of the device. Lower left inset: measurement setup.

This design defines a quantum point contact in the 2DEG. At low temperatures we expect the conductance G through both devices to be quantized in $2(e^2/h)$ as described in Chapter 2.2. For the transport measurement we used a standard lock-in technique with an excitation voltage of $V_{SD,ac} = 60$ μV at 13 Hz. The samples were set into a ^{3}He-cryostat with a base temperature $T = 350$ mK. The conductance curves presented here were recorded by varying one of the two in-plane gates whereas the second gate was kept at a fixed potential. A constant series resistance of the contacts and the 2DEG was subtracted. A schematic picture of the measurement setup is shown in the lower inset of Figure 4.8.

In Figure 4.8 the differential conductance dI_{SD}/dV_{SD} of the sample patterned with a Si-tip is shown. In the following we will refer to the sample just by mentioning the tip material. The conductance of the silicon-patterned sample, shown in Figure 4.8, exhibits only a few poorly resolved conductance plateaus. This indicates that there are many scatterers inside the channel which obscure the ballistic transport.

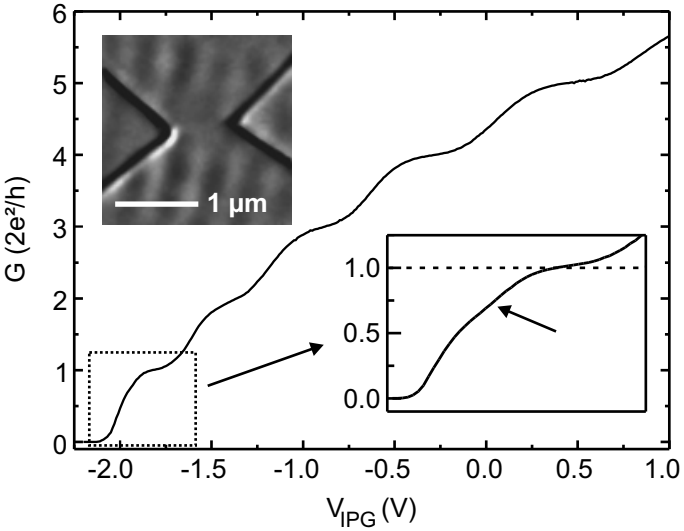

Figure 4.9: Conductance G of the QPC nanomachined with the diamond tip as a function of one in-plane gate voltage. The upper left inset shows an AFM micrograph of the device. The vertical lines are artifacts in this measurements. Lower left inset: the arrow indicates the 0.7-anomaly.

In contrast, the curve in Figure 4.9 corresponding to the diamond-patterned sample shows flat quantized plateaus at integer multiples of $2(e^2/h)$. This indicates the formation of a clean ballistic quantum point contact [48] formed by an adiabatic potential without any impurities. The appearance of the nice conductance plateaus demonstrates that the grooves scribed with the diamond tip define a smooth potential without significant fluctuations.

The electronic width of the constriction w_{dia} for the diamond tip can be roughly estimated by using formula 2.15 for a point contact. For the conductance and the carrier concentration, determined by Shubnikov-de Haas measurements, $w_{\mathrm{dia}} \sim 100$ nm is calculated at zero gate voltage. By comparison with the geometric width of 500 nm an estimation of the depletion width around the nanomachined barriers $w_{\mathrm{depl,dia}} \sim 200$ nm is obtained. This value is nearly half the length of $w_{\mathrm{depl,si}} \sim 370$ nm extracted for the silicon-patterned sample from the measurement shown in Figure 4.8.

The larger depletion length of the grooves created with the silicon

tip as well as the presence of significant potential fluctuations indicated by the resonant structures and the lack of plateau flatness are probably related to an enhanced formation of surface defects. These are caused by the increased number of scans needed for the depletion of the 2DEG. Additionally, the grooves scribed with the silicon tips are factor of two wider than the diamond ones, which might explain the difference in w_{depl}.

By inspection of the first conductance step in the right inset of Figure 4.9 we observe an additional shoulder close to 0.7 ($2e^2/h$). This so-called 0.7 anomaly [49] is an indicator for very clean one-dimensional channels and is considered to be caused by electron-electron interactions. The exact underlying mechanism of this structure is still not clear but it is an intrinsic property of low-disorder quantum point contacts. Together with the well resolved plateaus the appearance of the 0.7 anomaly shows that we scribed with the all-diamond tip a nearly adiabatic constriction free from significant potential fluctuations.

4.3 Local oxidation of heterostructures

One way to create tunnelling barriers in a GaAs/AlGaAs- heterostructure is described already in the preceding part of this chapter. Another possibility to deplete a two-dimensional electron gas is the oxidation of the heterostructure in an electrolytic cell. The oxide grown during the process protrudes into the surface and the band structure underneath is lifted above the Fermi energy E_F in the material very similar to the controlled nanomachining. Despite the difference to the mechanical removal of atoms from the surface this technique uses the same underlying principles as described in Chapter 3. We will show in this section that the local oxidation gives us a direct control over the height of the tunnelling barriers.

In the semiconductor industry the anodic oxidation in macroscopic electrolytic cells is a common technique to oxidize the surface of wafers during the processing of integrated circuits [50]. For the chemical reaction the wafer is mounted into a container in which a noble metal serves as cathode and the wafer material as anode. Water or acids (pH$<$ 7) serve usually as the electrolyte. From the chemical analysis of this macroscopic wet-chemical oxidation the reaction equation of GaAs is known [50]:

$$2\mathrm{GaAs} + 12\mathrm{h}^+ + 10\mathrm{OH}^- \longrightarrow \mathrm{Ga_2O_3} + \mathrm{As_2O_3} + 4\mathrm{H_2O} + 2\mathrm{H}^+ \ . \quad (4.1)$$

Here, h^+ stands for positively charged holes in the GaAs. This macroscopic process can be scaled down by using a conducting AFM tip to induce an oxidation of the GaAs locally beneath the tip.

Using a conducting AFM tip with a diameter of a few nanometers

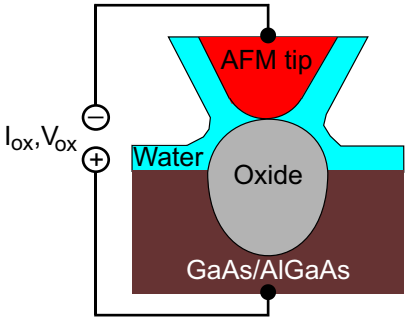

Figure 4.10: Electrolytic nanocell for the local anodic oxidation.

as cathode one can reduce the size of the above mentioned electrolytic cell dramatically to a few 100 nm^3. Under ambient conditions, there is an adsorbed water layer on almost every surface and provides the required electrolyte. The thickness of the water film depends on the relative humidity of the surrounding air. In Figure 4.10 a schematic picture of the electrolytic nanocell is shown. We oxidize the surface with the AFM tip in the contact mode: the tip remains in contact with the underlying heterostructure during the whole writing process. With a Keithley source-meter model 2400 we apply a constant current to the tip that is negatively biased with respect to the sample. The oxide protrudes out of the surface because of the volume expansion due to the incorporation of oxygen atoms.

The growth of the oxide in our experiments is determined by the oxidation current I_{ox} and the voltage V_{ox}. In our experiments I_{ox} is kept constant throughout the oxidation process. Because of the low tip-to-sample resistance of a few MΩ we can use $|V_{ox}| < 8$ V. This reduces the probability of electrostatic discharging that often destroys the tip during the writing process. The oxidation in the constant current mode extends the lifetime of an AFM tip [51].

Since the first experiments on the local oxidation of the surface of silicon with an AFM, the electrochemical induced nanolithography became an important tool for the fabrication of Si-based semiconductor devices [52, 53, 54, 55]. After the pioneering work of Ishii and Matsumoto [6] several groups began to utilize the so-called local anodic oxidation for the direct patterning of the two-dimensional electron gas (2DEG) in GaAs/AlGaAs-heterostructures [8, 56, 10, 57].

There were several studies on the reaction in this *nanocell* with silicon as anode [58, 59, 60]. Until now there exist several approaches to a detailed microscopic model of this nanooxidation process on Si [61, 62, 63]. The process on GaAs, compared to Si a very complicated material system, was only addressed by a study of Okada *et al.* [64], who investigated the influence of a voltage modulation on the oxide growth. Little is known about the exact reaction that takes place during the oxide formation in the nanocell at the GaAs/AlGaAs-surface. Studies with Auger-electron spectroscopy show that oxygen is incorporated into the surface by the local oxidation on Si [65, 66, 67] and heavily p-doped GaAs-wafers [68]. The reaction on heterostructures will be even more complicated since the samples consist not only of GaAs but of AlGaAs only a few nm below the surface as well (see Figure 3.2). The macroscopic reaction equation is no longer valid, leaving the exact form of

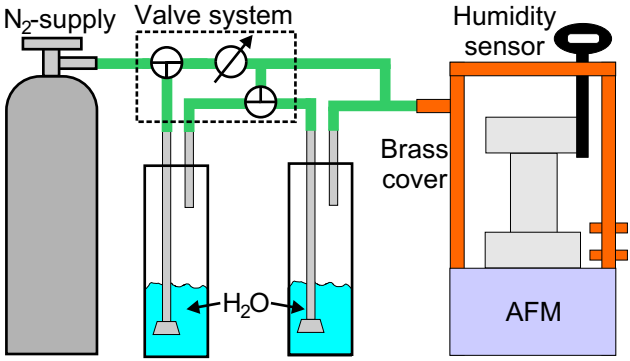

Figure 4.11: Schematic drawing of the continuous flow system for controlling the relative humidity for the local oxidation.

the equation unclear at this point of the experiments.

Experimental details

To learn more about the nanooxidation, the characteristics of the writing process on GaAs/AlGaAs, the influence of the oxidation current, relative humidity, and writing speed on the oxide depth and height will be discussed next. In all experiments highly n-doped tips with low spring constants of less than 0.1 N/m fabricated by Nanosensors were used. Controlling the thickness of the water film and thus the efficiency of the oxidation process, was achieved with a continuous flow system built around the AFM. A schematic picture is shown in Figure 4.11. A brass cover with openings (inlet and outlet) for gaseous Nitrogen allows an incessant gas stream during the scanning and oxidation. We supply the Nitrogen from a pressure tank and control the relative humidity by mixing dry N_2 and N_2 that was moistened with distilled water. Additional openings enable the manipulation of the sample from the outside. The relative humidity is measured by a commercial sensor that is mounted inside the brass cover. Using this setup we can vary the relative humidity between 20% and 90%. It turned out that a constant room temperature is essential to avoid a drift in the relative humidity during the experiments. The installation of an air conditioning in the laboratory solved this problem.

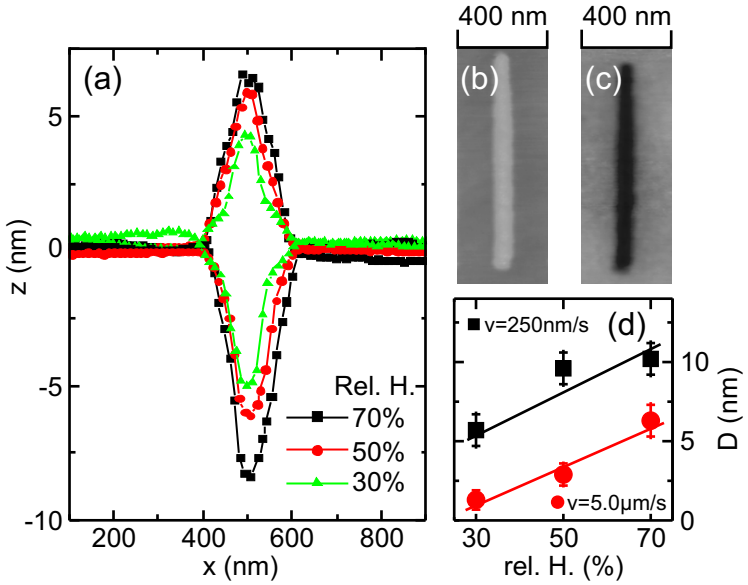

Figure 4.12: (a) Section of the height/depth of an oxide line as a function of the position on the sample before/after a HCl etch. Writing speed $v = 250$ nm/s and $I_{ox} = 100$ nA. (b) AFM image of an oxide line before and (c) after the HCl etch. (d) Depth D of the oxide lines as a function of the relative humidity for two tip velocities ($v_{\text{tip}} = 250$ nm/s, $v_{\text{tip}} = 5.0$ μm/s) at $I_{ox} = 100$ nA. The lines serve to guide the eyes.

Dependence on relative humidity and tip velocity

The depth of the oxide lines is the most important parameter for the depletion of the heterostructures. We studied the dependence of the oxide growth on the relative humidity by writing several oxide lines at different relative humidities and with varying tip velocities. All experiments were done with a constant oxidation current. Directly after the oxidation the height of each line was measured using the same AFM tip. The oxide depth can be determined by dipping the samples for 30 s in hydrochloric acid (17%) that selectively removes the oxide. After the HCl treatment the sample was mounted again into the AFM to analyze the depth of the remaining groove.

Figure 4.12(a) shows the height/depth profile of three oxide lines

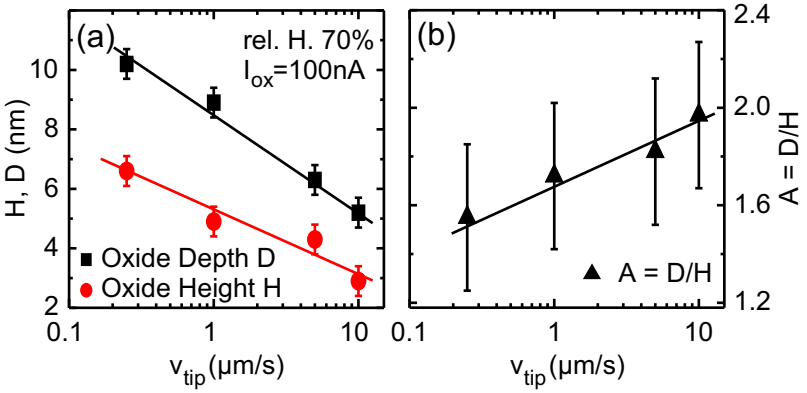

Figure 4.13: (a) Oxide height H and depth D as a function of the tip velocity v_{tip} (b) Average aspect ratio $A = D/H$ as a function of v_{tip} for all humidities and currents. The lines serve as a guide to the eye.

that were created at three different relative humidities of 30%, 50%, and 70% with a writing velocity $v_{\text{tip}} = 250$ nm/s and $I_{ox} = 100$ nA with the same AFM tip on wafer 81016. In the lower part of Figure 4.12(a) the depth-profile of the three lines is shown. The profiles were obtained by averaging ten consecutive scan lines in the middle of each oxide line before and after the HCl-etch. Figure 4.12(b)+(c) displays two AFM images of an oxide line at 70% relative humidity before (b) and after (c) the HCl treatment. It is evident that the oxidation depth and height increases with an increasing thickness of the water film on the surface. In Figure 4.12(d) the depth D of oxide lines is shown as a function of the relative humidity for $I_{ox} = 100$ nA with $v_{\text{tip}} = 250$ nm/s and $v_{\text{tip}} = 5.0$ μm/s. For both tip velocities the depth of the oxide increases with growing humidity.

These results indicate that the depth of an oxide line written with a constant oxidation current I_{ox} depends directly on the relative humidity. A similar behaviour was found in a study of Avouris *et al.* for the local oxidation of Silicon as well [69].

To characterize the lines we define the aspect ratio $A = D/H$ with D the oxide depth and H the height of the lines. The influence of the velocity on the aspect ratio A is shown in Figure 4.13(a) where we plotted the depth D and height H at $v_{\text{tip}} = 250$ nm/s, 1.0 μm/s, 5.0 μm/s, 10.0 μm/s (at constant relative humidity 70%, $I_{ox} = 100$ nA). An in-

creasing v_{tip} leads to a reduction of the oxidation depth due to the shorter reaction time.

From Figure 4.13(a) we can conclude that the oxide height is smaller than the depth at every tip velocity. By analysing the data of 48 oxide lines created at different relative humidities (30%, 50%, 70%), oxidation currents ($I_{ox} = 100, 250, 500, 1000$ nA) and four different writing velocities ($v_{\mathrm{tip}} = 0.25, 1.0, 5.0, 10.0$ μm/s) we calculated $A = D/H$. A is shown in Fig.4.13(b) as a function of v_{tip}, the error bars reflect the sometimes very rough oxide surface. At $v_{\mathrm{tip}} = 0.25$ μm/s we get $A \sim 1.6$ and with increasing v_{tip} the aspect ratio grows to $A \sim 2.0$. Apparently, the oxide grows faster into the substrate than out of the surface. This is in contrast to experiments on Si where $A < 1$ was observed e.g. in [69]. The origin of this difference is not clear.

The faster oxide growth into the GaAs compared to Si allows in principle to write narrower oxide lines that have the same depth. D is the most important parameter for the depletion of the 2DEG in a heterostructure. Thus one has to optimize the writing parameters to get the desired oxide depth. In the following we will show that the current during the oxidation determines D and thus the barrier height Φ_0.

4.3.1 Tunnelling barriers by local oxidation

After this short introduction to the chemistry of the local oxidation with an AFM, we will focus on the main topic: the fabrication of tunnelling barriers in the 2DEGs of the heterostructures. Of special interest is the result of an earlier study which indicates that the electronic height Φ_0 of a tunnelling barrier, respectively the depletion of the 2DEG underneath an oxide line, depends linearly on the oxidation current I_{ox} [24, 10]. The exact origin of this experimental result was not clear, although a higher I_{ox} was believed to deepen the oxide [24, 69], which would explain this effect.

To test this hypothesis 15 oxide lines were written at a relative humidity of 70% with our typical writing velocity of $v_{\mathrm{tip}} = 250$ nm/s on the wafer 81016. The oxidation current was varied between 10 nA$< I_{ox} <$ 1000 nA. In Figure 4.14(a) we plotted the depth D of the 15 lines extracted from the AFM image after the removal of the oxide. Several functions were fit to the data to determine the dependence of

D on I_{ox}. The best fit was obtained with the phenomenological form

$$D(I_{ox}) \propto I_{ox}^{0.4\pm0.05} \quad . \tag{4.2}$$

The origin of this dependence could not be clarified up to now. The finite oxidation voltage might be an explanation. This will be discussed in more detail in a later paragraph.

The three data points for $D > 6$ nm indicate perhaps a change in the kinetic of the oxide growth. This is possible, because this particular heterostructure has a 5 nm thick GaAs-cap layer. Directly underneath follows a layer of AlGaAs which might lead to another oxide growth. However with only three data points this is very speculative.

As mentioned above, underneath the oxide a tunnelling barrier is formed in the 2DEG, which is described by its electronic height Φ_0 above the conduction band edge. In the inset of Figure 4.14(b) a sketch of the conduction band with a tunnelling barrier is depicted. The relation between the depth of the oxide lines and the depletion of the 2DEG is determined by calculating the band structure of wafer 81016 for oxide depths ranging from $D = 1$ nm to $D = 9$ nm. The result is displayed in Figure 4.14(b). A fit with a similar phenomenological function as in Figure 4.14(a) yielded

$$\Phi_0 \propto D^{2.4\pm0.05} \tag{4.3}$$

and is shown in Figure 4.14(b). In general, the exact dependence has to be calculated for each heterostructure.

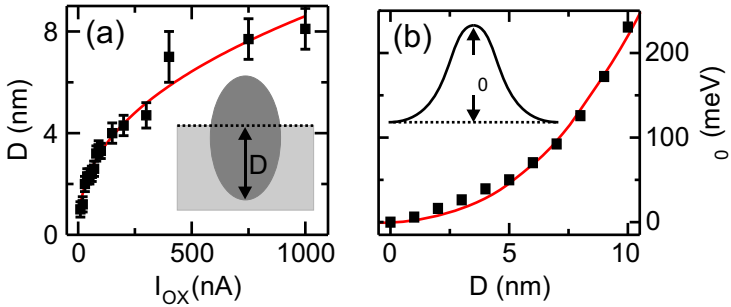

Figure 4.14: (a) Oxide depth D as a function of oxidation current I_{ox}. (b) Change of the conduction band minimum as a function of D calculated with SimWindows [28].

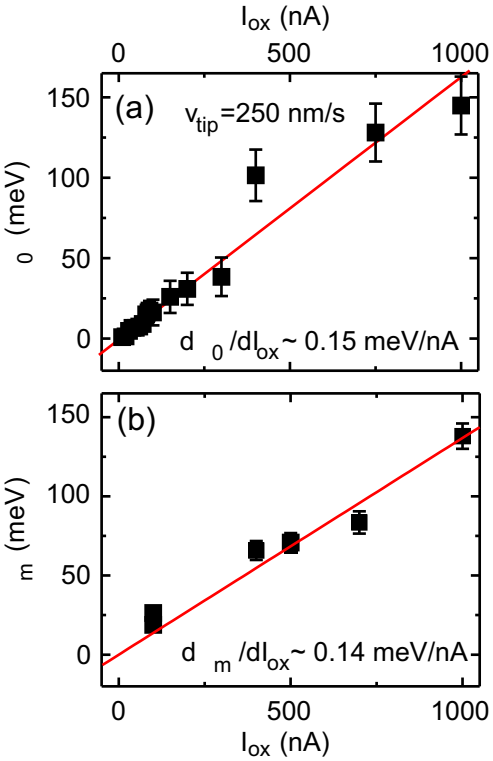

Figure 4.15: (a) Calculated barrier height Φ_0 from the data in Figure 4.14. (b) Measured barrier height Φ_m taken from Ref. [24].

For calculating the dependence of Φ_0 on I_{ox} we use formula 4.2 in formula 4.3

$$\Phi_0 \propto I_{ox}. \tag{4.4}$$

For this specific heterostructure the two results lead to a linear dependence of Φ_0 on I_{ox}. The computed Φ_0 with the deduced depth of the oxide lines is plotted in Figure 4.15(a). We observe a linear dependence with a slope of 0.15 ± 0.01 meV/nA. Figure 4.15(b) shows the experimental results of the measured barrier heights Φ_m of six oxide lines written on wafer 81016 taken from Ref. [24]. The slope is 0.14 ± 0.1 meV/nA which is in very good agreement with the value extracted from the calculations.

The linear dependence of the barrier height on the oxidation current

is especially interesting since we have control over Φ_0 by adjusting an external parameter that is easily controlled with a current source. In Chapter 5.1 we will use this technique for the direct writing of a single-electron transistor.

Remarks on the importance of the oxidation current

These results underline clearly the importance of the oxidation current for the writing of tunnelling barriers with a constant oxidation current. The experimentally found linear dependence of the barrier heights on the oxidation current is in good agreement with the calculated values. One should keep in mind that these extensive experiments were done only on wafer 81016 and the origin for the dependence of the oxide depth on the oxidation current is not totally clear. One possible explanation for the saturation of the oxide depth at the higher currents is the saturation of the oxidation voltage in our experiments. In several studies it was shown that the oxide depth is limited by the field strength in the oxide [58] because the OH^--ions will no longer be transported through the oxide and finally the reaction will cease to exist.

Compared to Si with an aspect ratio of $A < 1$ our results prove that the current enhances the oxide growth into the GaAs which is indicated by the high aspect ratios of oxide depth vs. oxide height. This might be an indication for another mechanism of the oxidation. Please note that more oxygen is incorporated in Si (two O-atoms per Si-atom) than in GaAs (1.5 O for each Ga and As). This might explain dhe different A found in the experiments. But the exact stoichiometry of the oxide growth is still unclear. It is known for instance that these anodic oxides contain a finite amount of water that enhances the volume expansion [50].

However, the exact influence of the oxidation current is still to be clarified. For an oxide line with a depth of 6 nm, width of 100 nm, length of 1 μm, and $v_{\mathrm{tip}} = 250$ nm/s an oxidation current of less than 10^{-12} A would suffice to fulfill equation 4.1. In principle, we need only 12 h^+ to oxidize two Ga- and As-atoms. Thus we conclude that the main part of the oxidation current is a direct (tunnelling) current between tip and sample. The influence on the reaction might be explained as follows. Avouris *et al.* demonstrated a current induced local oxidation process in thin metallic films with current densities in the order of 10^{11} Am^{-2} [58]. Our oxidation currents lead to densities in the range of 10^{10} Am^{-2} which is one order of magnitude smaller.

For this estimation we assumed a tip radius in the range of half the typical line width. Further mechanisms that might play a role are a local heating underneath the tip and an electromigration of atoms or the OH^--ions. Actually, high currents through an AFM tip were used to change the doping of a semiconductor [70].

Further studies are needed to learn more about the mechanism and exact reaction of the oxidation with constant oxidation current. The usage of durable AFM tips (e.g. diamond) and different heterostructures, would help to clarify the influence of the layer structures, the different elements (Al, Ga, As, Si, ..), and the shape and doping of the AFM tip on the local oxidation.

4.4 Comparison of local oxidation and nanomachining

In Chapter 4.2 we described mechanical nanomachining as another approach to fabricate tunnelling barriers. Both the nanomachining and the local oxidation together with the flexibility of the AFM allow to write directly almost every geometry with an AFM tip into the 2DEG. Here we want to compare the two fabrication principles and comment on the practicability of both techniques.

The major advantage of the nanomachining and the local oxidation is the spatial separation between the created structures and the 2DEG which minimizes the possible formation of defects. Additionally, we don't need any further processing steps, masks, or photoresists to complete our samples.

Both approaches have their distinct advantages. With the local oxidation we can controllably write tunnelling barriers with a specific height into the 2DEG. But there are limitations to the maximum breakdown voltages to a few hundred meV. With the nanomachining we can deplete 2DEGs that are more than 100 nm below the surface and create insulating lines with breakdown voltages of several volts [71] but the 2DEG is depleted 200 nm around the nanomachined lines. This reduces the steepness of the potential walls of devices defined by nanomachining compared to the local oxidation where the depletion length is only a few ten nanometers long, see Chapter 5. Because of the limitation to the oxide growth, the local oxidation is limited to 2DEGs that are less than 50 nm below the surface [30]. Because of the water film needed

for the chemical reaction the local oxidation has to be performed under ambient conditions. In contrast, the nanomachining of surfaces could be utilized in principle in any environment, ranging from a cryostat with temperatures of some Kelvin to applications in a ultra-high vacuum chamber for e.g. the in situ manipulation of samples grown with molecular beam epitaxy. Which of the techniques is finally used for fabricating mesoscopic devices depends on the desired characteristics.

4.5 Conclusion

In the first part of this chapter we introduced the controlled nanomachining for the depletion of heterostructures. We fabricated quantum point contact devices by engraving a constriction into a GaAs/AlGaAs-heterostructure with the tip of an atomic force microscope. We scribed devices using both a silicon tip and a diamond tip to study the influence of the tip material. It turned out that a diamond tip is almost perfect not only on the basis of a fast and simple processing but also in forming proper potential profiles to observe ballistic electron transport. The appearance of the 0.7 ($2e^2/h$) conductance anomaly confirms the high quality of diamond-engraved devices. We deduced the depletion lengths induced by the different tips, yielding $w_{\mathrm{depl,dia}} \sim 200$ nm for diamond-engraved samples, which is roughly two times smaller than typical depletion lengths in devices patterned with a Silicon tip.

In the second part of the chapter we introduced the local oxidation with an AFM. With this alternative approach to the depletion of heterostructures we have a technique that gives us a direct control over the height of the tunnelling barriers in a two-dimensional electron gas. With the analysis of the oxidation process we proved that the oxidation current determines the barrier height. We found a linear dependence between the oxidation current and the barrier height on the investigated wafer. With these tunnelling barriers we are able to fabricate a single-electron transistor as we demonstrate in Chapter 5.

5 Coulomb blockade in quantum dots

In this chapter we introduce the basic principles of the constant interaction model that is used to describe the characteristics of single-electron transistors. We develop the model and compare it with the results obtained from transport measurements on a single-electron transistor. This device was fabricated with local oxidation with an atomic force microscope (AFM) in a GaAs/AlGaAs-heterostructure and is described well within the framework of the model.

In the second part we demonstrate the stepwise fabrication of parallel double quantum dots. First a 2D-1D-2D resonant tunnelling device is fabricated with controlled nanomachining of the in-plane gates and subsequent local oxidation of a double-barrier structure. The resonant tunnelling device shows negative differential conductance in transport measurements at low temperatures. After this characterization two parallel quantum dots are created by cutting the 1D-wire again with local oxidation into two small quasi zero-dimensional regions. The new device shows Coulomb-blockade oscillations and diamonds with different periods for each of the quantum dots.[1]

[1] Parts of this chapter were already published in U. F. Keyser, H. W. Schumacher, U. Zeitler, R. J. Haug, and K. Eberl, *Fabrication of quantum dots with scanning probe nanolithography*, physica status solidii (b) **224**, 384 (2001) and U. F. Keyser, M. Paesler, U. Zeitler, R. J. Haug, and K. Eberl, *Direct fabrication of parallel double quantum dots with an atomic force microscope*, accepted for publication in Physica E.

5.1 Single charge tunnelling

A single-electron transistor consists of a small region of space, in semiconductor physics named quantum dot (QD), that is coupled to the environment, source and drain contacts and a capacitively coupling gate. In Figure 5.1(a) a schematic picture of such a single-electron transistor (SET) is shown. There are many different possible realizations of these structures. A detailed description of these techniques lies outside the scope of this thesis and can be found in the extensive literature, see e.g. [1, 72].

The corresponding circuit diagram for a SET is depicted in Figure 5.1(b). W choose to depict a configuration with two gate electrodes ($G1$ and $G2$) because this is a common feature for all our devices. Each gate has a capacitance $C_{G,x}$ ($x = 1, 2$) to the QD. The tunnelling barriers that separate the dot from the leads are characterized by their tunnelling rates $\Gamma_{S,D}$ and the capacitances $C_{S,D}$ to the source and drain contacts, respectively.

5.1.1 Constant interaction model

To start, we define the classical overall capacitance of a SET $C_\Sigma = \sum_i C_i$ by the sum over the capacitances C_i of every attached contact or gate. With these definitions and neglecting any influence from the single-particle energy levels, the free energy $F(N)$ of a QD is just the

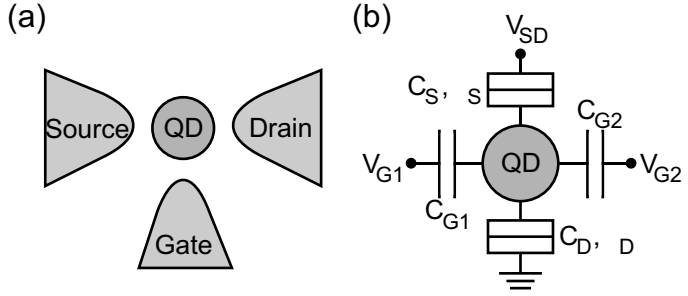

Figure 5.1: (a) Single-electron transistor (SET): a quantum dot (QD) is coupled to contacts, source and drain, and a gate electrode. (b) Circuit diagram for an SET with two attached gates. Each contact and gate is characterized by a specific capacitance C_i to the QD. The tunnelling barriers are defined by the transparencies $\Gamma_{S,D}$

sum of the classical energy of a capacitor with C_Σ and the outer gate voltages:

$$F(N) = \frac{(Ne)^2}{2C_\Sigma} - \sum_i Ne\frac{C_i}{C_\Sigma}V_i \tag{5.1}$$

where the sum over i is carried out over all outer voltages V_i. The chemical potential $\mu_{QD}(N)$ of the QD is defined as the derivative of $F(N)$ with respect to N:

$$\mu_{QD}(N) = \frac{\partial F(N)}{\partial N} = \frac{e^2}{C_\Sigma}N - \frac{1}{C_\Sigma}\sum_i NC_i eV_i \ . \tag{5.2}$$

To add one electron to a QD with N electrons we have to pay the charging energy $U = \mu_{QD}(N+1) - \mu QD(N) = e^2/C_\Sigma$. In this model U is constant with respect to N if C_Σ and all other capacitances are independent of N, in general this is only true for metallic or semiconductor QDs with $N \gg 100$.

With a slight modification of this model by adding the single-particle levels E_s inside the QD to $F(N)$ we get the *constant interaction model* which is the most simple description of a semiconductor quantum dot:

$$F = \sum_1^N E_s + \frac{(Ne)^2}{2C_\Sigma} + Ne\sum_i c_i V_i. \tag{5.3}$$

The energy difference ΔE needed to add an electron to the QD has to include the energy difference of the single particle levels:

$$\Delta E = \frac{e^2}{C_\Sigma} + E_{N+1} - E_N. \tag{5.4}$$

If the same state is filled consecutively with a spin up and a spin down electron it follows that $\Delta E = U + E_{N+1} - E_N = U$. For electrons added to different states $E_{N+1} \neq E_N$, ΔE will be larger than U. In general, U, C_i, and the level structure will depend upon the gate voltages. In this case the constant interaction model still describes the main features of the transport characteristic of SETs but only in a small range of the gate voltage.

Coulomb-blockade oscillations

After the definition of $\mu_{QD}(N)$ one can write down the relations that have to be fulfilled to get a stable number of electrons N on a QD. With

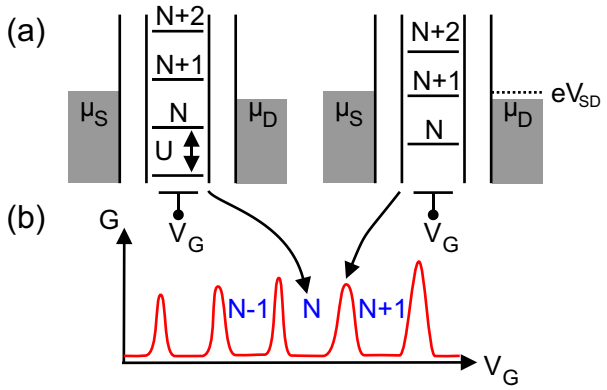

Figure 5.2: (a) Schematic picture of a QD between the tunnelling barriers, with attached leads, and one gate. μ_S and μ_D denote the electrochemical potential in the contacts. A small bias voltage is applied which leads to $\Delta\mu = \mu_S - \mu_D = eV_{SD}$. We show the addition spectrum. (b) Coulomb-blockade oscillations as a function of the gate voltage at finite temperatures. After each peak the electron number on the dot N increases by one.

μ_S, μ_D as the chemical potentials in the source and drain contacts these are:

1. $\mu_S, \mu_D < \mu_{QD}(N+1)$
2. $\mu_S, \mu_D > \mu_{QD}(N)$
3. $\mu_S, \mu_D + k_B T < \mu_{QD}(N+1)$.

$k_B T$ is the thermal energy of the electrons in the leads, with k_B Boltzmann's constant and T the absolute temperature. If the chemical potentials in the contacts are higher than $\mu_{QD}(N)$ but lower than $\mu_{QD}(N+1)$, because of energy conservation N is fixed (relations (1)+(2)).

A typical charging energy U for our devices is in the range of 1 meV which corresponds to a temperature range of $T \sim 10$ K. An observation of the charging effects requires $U \gg k_B T$ and thus the temperature T of the device has to be $T < 1$ K to fulfill relation (3) and enable an undistorted measurement of the Coulomb blockade.

A simple sketch of a quantum dot with the two tunnelling barriers and energy levels equally spaced by U is shown in Figure 5.2(a) at

$T = 0$. One gate is depicted underneath the structure. Here we assume that the level spacing $E_{N+1} - E_N$ is much smaller than U.

We can tune μ_{QD} by the outer gate voltages and thus N is directly controlled. We start our discussion with the configuration shown in the left-hand picture in Figure 5.2(a). If only a small bias voltage $eV_{SD} \ll U$ is applied, no electrons are transported through the QD if conditions (1)-(3) are met and there are N electrons on the dot. By increasing V_G the electrochemical potential is lowered until $\mu_S \geq \mu_{QD}(N+1) \geq \mu_D$. As soon as the level enters the small bias window, the charge on the QD fluctuates between N and $N+1$, right-hand side in Figure 5.2(a). A sharp rise of the conductance G is the consequence due to the electrons passing the QD. With a further increase of V_G it finally follows $\mu_{QD}(N+1) < \mu_D$ and the direct tunnelling of electrons is once more blocked. G drops again to zero.

This behaviour leads to a peak in the $G(V_G)$ characteristic. A sequence of these peaks is often named as Coulomb-blockade oscillations. After each peak the electron number on the QD is again constant but with one additional charge confined on the dot. These considerations are summarized in the schematic picture in Figure 5.2(a).

In Figure 5.2(b) we show the schematic characteristic for a semiconductor quantum dot at finite temperatures. The peak heights reflect the different overlap of the wave function on the dot with the contacts due to distinct single-particle states. It should be mentioned again, that $k_B T \ll U$ is required to observe these effects.

For a determination of the overall capacitance C_Σ and thus an estimate for the charging energy U we have to compare the level spacing on the QD with a *known* energy like that of the injected electrons $E = \alpha e V_{SD}$. Here α is again a lever factor (see Chapter 2.3.1) that accounts for the voltage drop occurring partly at the first and the second tunnelling barrier. We start with the configuration shown in Figure 5.3(a) with $\mu_S = \mu_D = \mu_{QD}(N+1) + U/2$. In this case, adding an electron to a symmetric QD ($\alpha = 0.5$) requires a source-drain voltage $V_{SD,U}$

$$V_{SD,U} = 2 \cdot 0.5 \frac{U}{e} = \frac{e}{C_\Sigma} \ . \tag{5.5}$$

This is depicted on the right-hand side of Figure 5.3(a). In this configuration the charge on the dot fluctuates between $N-1$, N, and $N+1$.

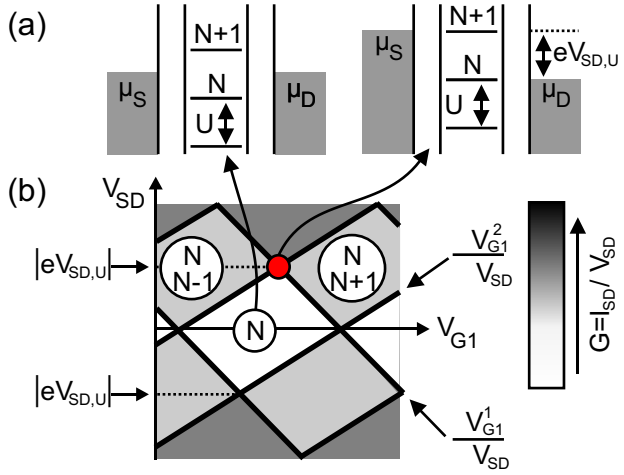

Figure 5.3: (a) Sketch of a quantum dot at zero and finite bias voltages. (b) Ideal charge stability diagram of a quantum dot: the conductance $G(V_G, V_{SD})$ is shown. The thick black lines denote the position of the Coulomb-blockade peaks.

The charge stability diagram

The position of the energy levels on the dot depends on all outer gate and bias voltages. Each voltage pair in the V_{SD}, V_G-plane where an electron might be added to the dot defines a charge-degeneracy point. At these points the electron number is not constant and a current can flow through the quantum dot.

As explained in the former section, this is achieved by either applying a sufficiently high V_G or by increasing V_{SD}, Figure 5.3(a). A condition for the constant interaction model is that the capacitances are constant and thus μ_{QD} depends linearly on all applied voltages. Therefore, the regions in the V_{SD}, V_G-plane where N is stable have boundaries that lie on straight lines when we plot the conductance $G = I_{SD}/V_{SD}$ as a function of V_{SD} and V_G, as shown in Figure 5.3(b). The gradients of the peak shifts can be calculated to

$$\frac{\partial V_{SD}^1}{\partial V_{G1}} = -\frac{C_{Gi}}{C_S} \tag{5.6}$$

$$\frac{\partial V_{SD}^2}{\partial V_{G1}} = \frac{C_{Gi}}{C_\Sigma - C_S} \tag{5.7}$$

these lines border the so-called Coulomb-blockade rhombus or diamond. A detailed description of the derivation of these formulae can be found in Ref. [73]. The resulting graph is known as the *charge stability diagram* and is depicted in the lower part of Figure 5.3(b).

Inside each diamond around zero bias the number of electrons on the QD is stable and no transport takes place. In the diamonds with their center at finite bias voltages the charge on the dot can fluctuate which leads to a finite G. These diamonds are depicted in light grey. The possible electron numbers on the dot are given in the circles in each region with constant G in Figure 5.7(b). For example, in the diamond marked with N and $N+1$ the charge on the dot fluctuates between these values. The arrows connect the dot configurations shown in Figure 5.3(a) with the corresponding positions in the plot. As one can see the maximum width of the diamonds in the V_{SD}-direction gives us an estimate for $V_{SD,U}$.

In principle, this graph contains all the information needed to characterize an SET with its capacitances. In our common measurement setups the drain contact is grounded. Please note, that a direct measurement of the drain capacitance C_D is only possible by an exchange of the contacts.

Remarks on the model

We want to emphasize that this model holds only for low tunnel coupling between the QD and the leads. Low means in this context that the tunnelling resistance R_T of each barrier has to be much higher than h/e^2. This relation is obtained from the uncertainty relation $\Delta E \Delta t \gg h$ and the overall capacitance C_Σ of the quantum dot that defines a typical time scale $\Delta t = R_T C_\Sigma$.

Transport through the dot in this coupling regime will occur as two sequential tunnelling events of *one* electron. Higher order or correlated tunnelling of more than one electron at a time will be suppressed with a factor of $(\hbar\Gamma)^n$ $n = 2$ being the number of tunnelling barriers and $\Gamma = \Gamma_S + \Gamma_D$ the barrier transparencies of the source and drain barrier. $\Gamma_{S,D}$ measures the tunnelling rate of the electrons through the source and drain barrier, respectively. Additionally, we assume that the energy conservation is valid for all tunnelling events. Deviations from this behaviour will be later discussed in this thesis.

Local oxidation of a single-electron transistor

In the preceding paragraphs we discussed the constant interaction model. In this section we compare the characteristics of a "real" SET with the model.

We fabricated our SET on wafer 81016 with the local oxidation technique described in Section 4.3. The 2DEG is 40 nm below the surface. The exact layer sequence and important parameters of the 2DEG in this GaAs/AlGaAs-heterostructure can be found in Chapter 3.1. An AFM image of the completed SET is depicted in Figure 5.4. The in-plane gates [74] (marked by IPG1 and IPG2 in the figure) were isolated from the rest of the 2DEG by oxide lines defined on the surface with an oxidation current of $I_{ox} = 1\ \mu$A. The oxide lines were written three times to avoid any defects that could lead to a leaking gate. These define the boundaries of a 400 nm wide channel that connects the source and drain contacts.

In the next step a quantum dot is defined by writing two tunnelling barriers with a ten times lower current of $I_{ox} = 100$ nA perpendicular to the channel into the 2DEG. They have a distance of 300 nm. This forms a small island of 400×300 nm^2 with about 500 electrons. The number was estimated from the electron density of the material 81016 (see Table 3.1). The two tunnelling barriers couple the quantum dot between the IPGs to the source and drain contacts. With this config-

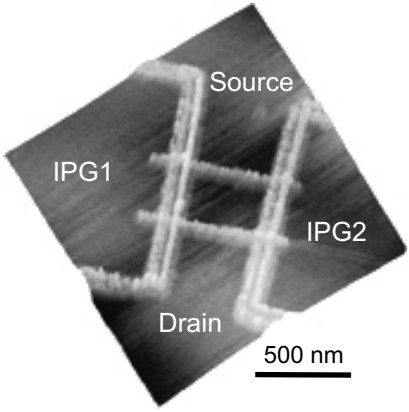

Figure 5.4: AFM image of a single-electron transistor on wafer 81016 fabricated with local oxidation. The island dimensions are 300×400 nm^2.

uration the SET corresponds directly to the circuit diagram already discussed in Figure 5.1(b).

Measurement of Coulomb-blockade oscillations

The Coulomb-blockade oscillations of our quantum dot measured at $T = 350$ mK with a standard lock-in setup are shown in Figure 5.5 as a function of V_{G1}. The peak conductance increases because the tunnelling barriers are also influenced by the in-plane gate voltage V_{G1}, but the distance between the peaks is constant over the whole gate voltage range. This experimental finding indicates that the constant interaction model is applicable for the description and N will be large in this structure. The extracted gate capacitance $C_{G1} = 28$ aF is calculated with

$$C_{Gi} = \frac{e}{\Delta V_{Gi}} \tag{5.8}$$

with ΔV_{G1} the peak spacing of two consecutive Coulomb-blockade peaks.

The symmetry of the gates is tested by measuring the gate-gate characteristic of the QD in the linear transport regime $V_{SD} \sim 0$: One gate (IPG1) is stepped while sweeping the other gate voltage (IPG2) quasi continuously. The result is shown as a grey-scale plot of the conductance G as a function of V_{G1}, V_{G2} in Figure 5.6. Black stands for high and white for low conductance. All Coulomb-blockade peaks move

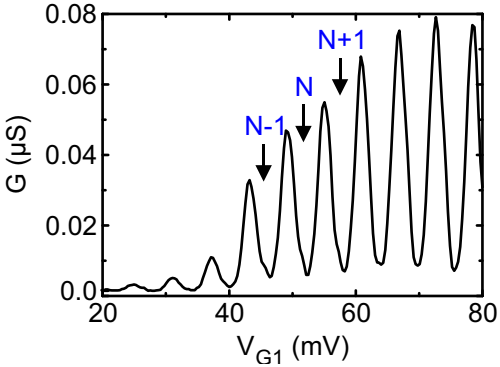

Figure 5.5: Measurement of the linear conductance G of the oxidized SET as a function of the in-plane gate voltage V_{G1} at $V_{G2} = 30$ mV, $T = 350$ mK.

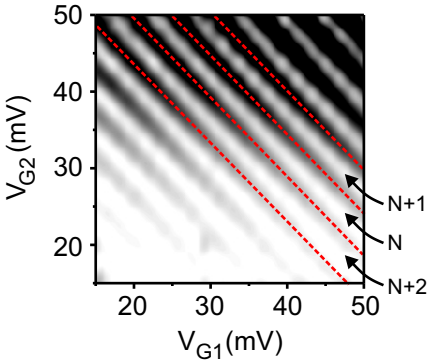

Figure 5.6: Grey-scale plot of the measured linear conductance G as a function of both in-plane gate voltages V_{G1}, V_{G2}.

parallel in the plane, which means that both gate capacitances are constant. This is underlined by the parallel dashed lines that denote the positions of four adjacent Coulomb-blockade peaks. From the symmetry of the plot we can conclude already that the gates are almost symmetric. A calculation of the capacitance of IPG2 yields $C_{G2} = 26$ aF, which is indeed very close to the value for IPG1. This indicates that the gates are very symmetric as expected from the fabrication with the same oxidation current. The extracted capacitances are summarized in Table 5.1.

Charging Energy of the dot

In Figure 5.7 the differential conductance as a function of V_{SD} and V_{G1} is plotted as a grey-scale map. As usual in this thesis high conductance is displayed in black and low appears as white. The real device behaves as expected and shows nice Coulomb-blockade diamonds over the full voltage range. For clarity, one Coulomb-blockade diamond is marked by white lines. The extracted charging energy $U \sim 0.9$ meV remains almost constant throughout the whole measurement. With this result we calculate the overall capacitance $C_\Sigma \sim 180$ aF. The deduced parameters are shown in Table 5.1.

Knowing the charging energy the electric diameter D_e of the quantum dot can be estimated by assuming that the QD is a flat disk [75]:

$$C_d = 4\epsilon_0\epsilon_r D_e. \tag{5.9}$$

	AFM image
Width	400 nm
Length	300 nm
N	~ 500
	Transport measurements
U	~ 0.9 meV
C (aF)	
C_Σ	~ 180
C_{G1}	28
C_{G2}	26
C_S	~ 110
C_{BG}	~ 0.08

Table 5.1: Parameters extracted for the SET in Figure 5.4(a).

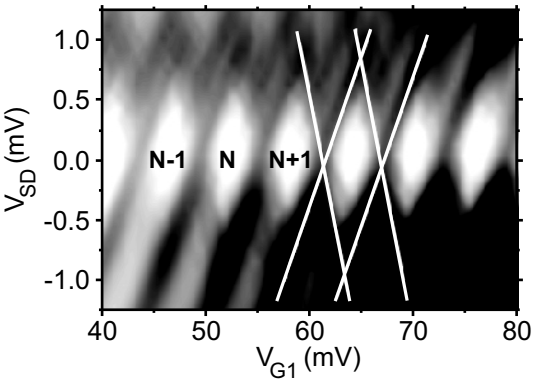

Figure 5.7: Differential conductance as a function of V_{SD} and V_{G1} of the SET shown in Figure 5.4(a), at $V_{G2} = 0.0$ mV and $T = 350$ mK.

For GaAs with $\epsilon_r = 12.4$ and $C_\Sigma = 180$ aF the electric diameter is $D_e \sim 400$ nm which is a little bit larger than the geometrically expected values. This discrepancy originates from the fact, that this equation describes the capacitance of a disc without any attached in-plane gates and neglecting any effects from the 2DEG. Here, the $C_{G,i}$ are already only a factor of four smaller than the overall capacitance V_Σ and thus cannot be neglected. Despite the major simplification of this calculation we can conclude, that the depletion length around the oxide lines is definitely smaller than 100 nm and most probably in the range of some ten nanometers. The values reported for the depletion length e.g. of shallow etched structures lie in the range of several 100 nm [76].

This result indicates the almost perfect transfer of the pattern generated by the local oxidation to the 2DEG. The very short depletion length was reported before in the literature but these structures were equipped with a metallic top-gate electrode and fabricated in an even shallower electron gas [56, 77]. Both features shorten the depletion length further compared to our experiments.

5.2 Stepwise fabrication of parallel quantum dots

We show the stepwise fabrication of two parallel quantum dots with an AFM. First we produce in-plane gates (IPG) with controlled nanomachining and subsequently a resonant tunnelling diode (RTD) with local oxidation by writing a double-barrier structure between the IPGs. The IPGs are fabricated with controlled nanomachining to achieve a wider gate voltage range. For the tunnel coupling we choose to use oxide barriers to have a maximum of control in the process.

The RTD shows negative differential resistance and especially the form of the resonance peak is controlled with an outer gate voltage applied to one of the IPGs. After the characterization of the device we cut the one-dimensional wire in two parts also with local oxidation which leads to the formation of two quasi zero-dimensional regions. These parallel quantum dots are characterized again with transport measurements and show Coulomb-blockade oscillations.

One interesting feature of parallel quantum dots is the possible formation of coherent electronic states, see e.g. [1]. Several groups studied extensively coupled quantum dots, but these experiments were per-

formed on devices with dots in series [78, 79, 80, 81] or with only one dot connected to the leads [82]. With the conventional lithographic techniques the fabrication of two quantum dots in parallel both coupled to the same contact pair is a very challenging problem. Very recently a new fabrication scheme was demonstrated by Holleitner *et al.* using elaborate electron beam lithography in combination with a calixarene layer [83]. The usage of AFM-based nanolithography provides a major simplification and a direct, simple, and robust approach to the manufacture of parallel double dots.

First step: Fabrication of an In-plane gate transistor

Our GaAs/AlGaAs-heterostructure was grown by molecular beam epitaxy with the following layer sequence from top to bottom: 10 nm GaAs cap layer, 15 nm Si-doped AlGaAs, 15 nm undoped AlGaAs spacer, and 500 nm of GaAs (wafer 81016, see Figure 3.2). This is the same heterostructure as used for the SET described in the preceding section.

In the first fabrication step the controlled nanomachining is done by applying a contact force of about 50 μN and scanning the tip over the surface ($v_{\mathrm{tip}} = 100$ μm/s). Grooves are scribed with a tapping-mode Si-tip into the GaAs/AlGaAs to deplete the 2DEG underneath and write insulating lines as described in Section 4.2. During the fabrication of the gates the sample resistance is monitored and as soon as the resistance of a nanomachined line exceeds 3 MΩ the tip is retracted. The low-temperature resistance of these lines is very high ($R > 50$ GΩ) over a wide voltage range (at least ± 3 V). The high resistance leads to low leakage currents, therefore the nanomachined lines are suitable to define gates for mesoscopic devices.

During the first step two in-plane gates (IPG) are nanomachined which define a lateral field effect transistor [74]. In principle, this device works like the quantum point contacts described in Section 4.2, but the defined channel is 2.7 μm wide and 2 μm long which is too wide for the observation of ballistic conductance in this heterostructure. After this processing, the IPG-transistor is tested at $T = 4.2$ K to check whether the gates have the expected high resistance to the constriction or not. If the devices show the expected characteristic, the samples are again mounted into the AFM for the further fabrication steps. Please note, that in the following parts of this chapter all transport measurements were performed in a ^{3}He-cryostat at a temperature $T = 350$ mK if not stated otherwise in the text.

Second step: Fabrication of a resonant tunnelling diode

The double-barrier structure is added to the IPG-channel by local oxidation with a conducting AFM tip. The AFM tip is negatively biased with respect to the grounded sample and scanned over the surface with a tip velocity of $v_{\mathrm{tip}} = 250$ nm/s. We work at a relative humidity of 60% and use the naturally formed water film on the sample as electrolyte for the electrochemical oxidation of the sample. As shown in Chapter 4.3 the height of the tunnel barriers Φ^{eff} depends linearly on I_{ox} [10].

The double-barrier structure was written across the IPG-channel with a distance of 250 nm between the tunnel barriers and an constant oxidation current of $I_{ox} = 150$ nA. An AFM image of the structure is shown in the inset of Figure 5.8. As mentioned above the gate-gate separation is 2.7 μm. Taking into account the depletion length of approximately 350 nm around the grooves made with a Si-tip (see Section 4.2) the conductive region is about 2.0 μm wide. Thus we have a lateral resonant tunnelling diode (RTD) consisting of an quasi one-dimensional island with a width of 250 nm and a almost ten times higher length of 2.0 μm.

The IV-characteristic of the device at $T = 350$ mK is depicted in Figure 5.8. The 1D-subband in the structure is coupled to the 2D-contacts by the two tunnelling barriers, and can be tuned by the IPGs relative to the electrochemical potentials of source μ_S and drain μ_D. Displayed is I_{SD} as a function of the voltage applied across the structure V_{SD}. The voltage of one IPG was stepped from -650 mV to -680 mV with $\Delta V_{IPG} = -10$ mV from top to bottom. All four curves show peaks in I_{SD} with negative differential conductance and a peak-to-valley ratio decreasing from 1.5:1 (-650 mV) to 1.1:1 (-680 mV). This demonstrates the tunability of the position and shape of the resonance by an IPG-voltage. With the in-plane gate voltage we tune the electrochemical potential of the contacts and thus the relative barrier heights. Our device shows a similar characteristic to a lateral RTD defined in a 2DEG with a negative biased metallic gate as shown by several groups, see e.g. [84, 85, 23].

The RTD has almost symmetric tunnelling barriers as indicated by the symmetric IV-characteristic in Figure 5.8. Both resonances have a peak current of just below 1 nA and the position of the resonance is almost the same for both bias directions $V_{\mathrm{res}} \sim |-V_{\mathrm{res}}|$.

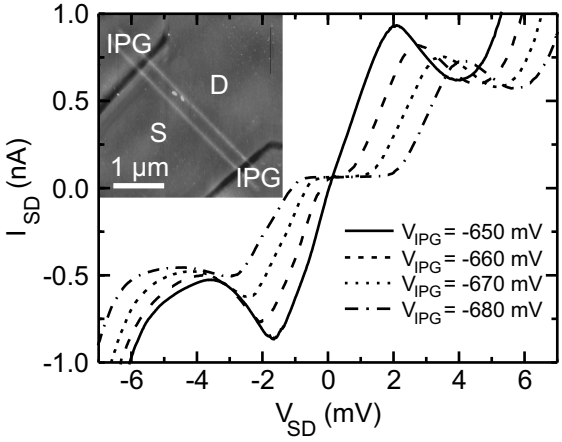

Figure 5.8: Source-drain current I_{SD} as a function of the source-drain bias V_{SD} for different in-plane gate voltages V_{IPG}, at $T = 350$ mK. Inset: AFM micrograph of the RTD. S and D mark the source-drain contacts and IPG the in-plane gates.

Third step: Fabrication of the parallel quantum dots

After this characterization step the RTD was again mounted into the AFM and another local oxidation was done to cut the 1D-wire into two quantum dots. In the AFM micrograph (Figure 5.9(a)) the sample is shown after the second oxidation step. The tunnelling barrier separating the dots was written with $I_{ox} = 300$ nA. Compared to the double-barrier structure this should lead to a lower tunnel coupling between the two quantum dots than between the dots and the leads, see Chapter 4.3.

The reduced tunnel coupling hinders the formation of a molecular state between the two quantum dots. With this design the most important interaction between the two dots is of the Coulomb type. The electrochemical potential of one dot may depend on the charging state of the other one. From the transport measurements we find that this is not important for the main characteristic of our device. These arguments indicate that we have two single-electron transistors in parallel that can be treated as individual devices. We apply the constant interaction model that was described in the preceding Section 5.1 to determine the capacitances of the QDs.

A simple circuit diagram of the device is displayed in Figure 5.11(b).

Both dots share the same leads enabling parallel transport through them. For clarity a configuration only with IPG1 is depicted. For the other gates (IPG2, backgate) one has to add capacitances between each gate and QD1 and QD2, respectively. The labels of the two quantum dots were chosen according to the nearest in-plane gate. For completeness we depict also a tunnelling barrier with a capacitive coupling between the two dots, but the inter-dot coupling is so small in our device that we can neglect it.

Transport measurements on the parallel quantum dots

We investigated the properties of this new sample with transport measurements as well. In principle, the capacitance between the quantum dot and one of the IPGs is determined by the size of the dot and the relative distance. In the next paragraph we will identify the Coulomb-blockade oscillations of the respective QD by measuring the gate-gate characteristic of the device.

In Figure 5.10(a) the source-drain current I_{SD} as a function of the backgate voltage for two different IPG-voltages is depicted. In the upper curve ($V_{IPG1} = -0.275$ V, $V_{IPG2} = -0.1$ V) we observe a fast oscillating Coulomb-blockade signal with a period $\Delta V \sim 0.36$ V that is modulated with a much longer period of ~ 6.3 V. In the lower curve in Figure 5.10(a) the gate voltages were set to $V_{IPG1} = -0.1$ V and $V_{IPG2} = -1.0$ V. The inset in Figure 5.10(a) shows a magni-

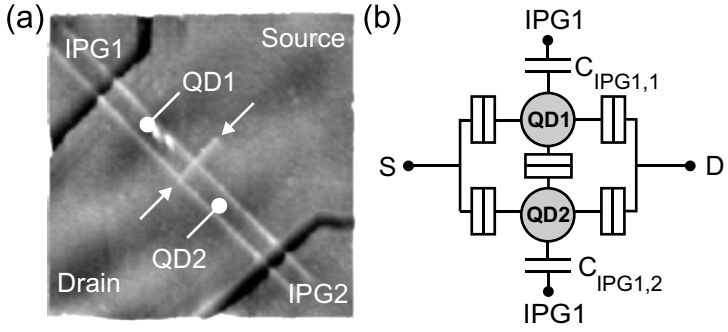

Figure 5.9: (a) AFM image of the parallel quantum dots, the RTD in Figure 5.8 was cut in the middle. The new oxide line is marked by the two arrows. (b) Circuit diagram for one gate configuration (IPG1).

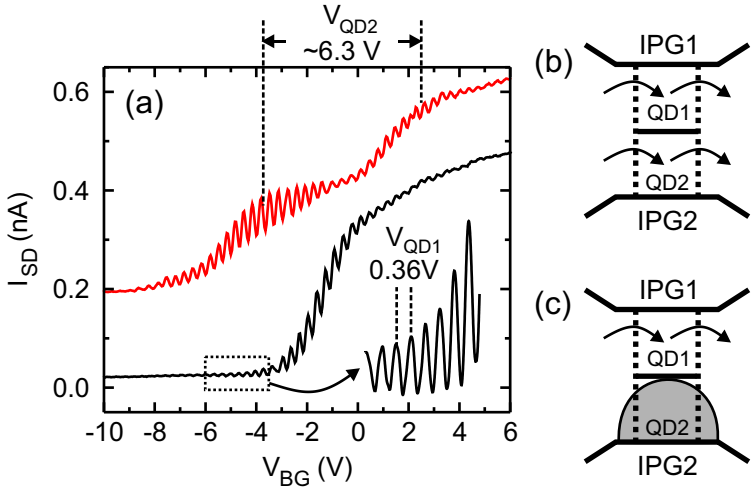

Figure 5.10: (a) Source-drain current I_{SD} as a function V_{BG} of the double quantum dot for $V_{IPG1} = -0.275$ V, $V_{IPG2} = -0.1$ V (upper curve) and $V_{IPG1} = -0.1$ V, $V_{IPG2} = -1.0$ V (lower curve). The curves are offset for clarity. (b)+(c) Blockade of the current flow through QD2 by applying a high negative gate voltage to IPG2.

fication of the region marked with the dashed box. At the second gate voltage pair the modulation observed in the upper curve vanished completely whereas the fast Coulomb-blockade oscillations remain unchanged apart from a slight shift. If we assume that the oscillations with the longer period belong to QD2, which is situated next to IPG2 and the oscillations with the shorter period to QD1 we can totally deplete and block the transport through QD2 by applying $V_{IPG2} \sim -1$ V. This circumstance is visualized in Figure 5.10(b)+(c). At high V_{IPG2} the transport through both dots occurs simultaneously (Figure 5.10(b)) but with increasing negative V_{IPG2} the QD2 is finally depleted and thus the transport is blocked, Figure 5.10(c).

In this context, IPG1 should control the adjacent QD1 in a similar manner. In Figure 5.11 traces of the differential conductance dI_{SD}/dV_{SD} at $V_{SD} \approx 0.0$ mV as a function of the backgate voltage V_{BG} are displayed. IPG2 was kept constant at -100 mV and IPG1 was stepped from -250 mV to -650 mV with $\Delta V = -100$ mV. In the topmost curve ($V_{IPG1} = -250$ mV) we observe the fast Coulomb-blockade oscillations with a period of $\Delta V_{BG} \sim 0.36$ V. This corresponds to a gate capaci-

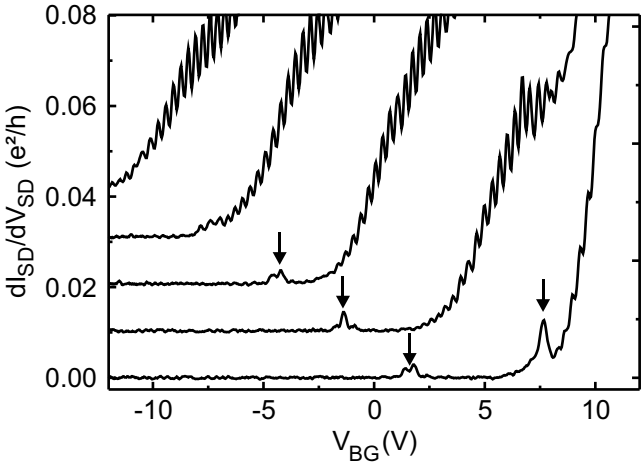

Figure 5.11: Measured differential conductance dI_{SD}/dV_{SD} as a function of V_{BG} and stepwise variation of V_{IPG1} (from top to bottom: -250 mV $\geq V_{IPG1} \geq -650$ mV, $\Delta V_{IPG1} = -100$ mV, $V_{IPG2} = -100$ mV, $T = 350$ mK). The Coulomb-blockade oscillations of QD2 are marked with arrows. The curves are offset for clarity.

	QD1	**QD2**
C (aF)	Figure 5.10 + Figure 5.11	
C_{BG} (aF)	0.45	0.025
C_{IPG1} (aF)	10	0.9
C_{IPG2} (aF)	8	1.1
	Figure 5.12	
C_S	90	40
C_D	~ 140	~ 28
C_Σ	250 ± 10	70 ± 15

Table 5.2: Extracted capacitances for the double quantum dot.

tance between this QD and the backgate of $C_{BG,1} \approx 0.45$ aF. As above we assume that this is the signal of QD1. By lowering V_{IPG1} (lower curves) the onset of the fast oscillations is shifted to higher V_{BG} and at $V_{IPG1} = -450$ mV a new peak appears (marked with an arrow) corresponding to adding of an electron to QD2. Finally at -650 mV a second series of Coulomb-blockade peaks with a much longer period of $\Delta V_{BG} \sim 6.3$ V is observed already seen in the upper curve in Figure 5.10(a). The corresponding capacitance is $C_{BG,2} = e/\Delta V \sim 0.03$ aF to the backgate. At $V_{IPG1} \geq -250$ mV the conductance is dominated by the fast oscillations and for $V_{IPG1} \leq -450$ mV we measure the Coulomb-blockade signals of both dots. At $V_{IPG1} = 650$ mV the fast oscillations are almost completely suppressed. From these results it is evident that IPG1 controls mainly the QD1 with its faster Coulomb-blockade oscillations. With the period of $\Delta V \sim 0.36$ V we extract the backgate capacitance of QD1 $C_{BG,2} \sim 0.45$ aF. We can conclude from these findings that we can control indeed the current flow through both dots with the two in-plane gates.

The assignment of the Coulomb-blockade oscillations to the two QDs can be checked by comparing the capacitances between the QDs and the two in-plane gates. Apart from the size of the dots, the distance between dot and gate should determine $C_{IPGx,y}$, with $x = 1, 2$ and $y = 1, 2$. The capacitance between QD1 and IPG1 $C_{IPG1,1} \approx 10$ aF is calculated from the shift of the Coulomb-blockade oscillations of QD1 by applying $\Delta V_{IPG1} = -0.1$ V in Figure 5.11 with $C_{IPG1,1} = \Delta C_{BG}/\Delta C_{IPG1} \times C_{BG,1}$. For the capacitance between IPG1 and QD2 we get $C_{IPG1,2} \approx 0.9$ aF. The capacitances $C_{IPG2,1} \approx 8$ aF and $C_{IPG2,2} \approx 1.1$ aF were deduced from the measurements in Figure 5.10(a).

The comparison of the above values yields $C_{IPG1,1} > C_{IPG2,1}$ and $C_{IPG1,2} < C_{IPG2,2}$. This indicates that the distance between QD1 and IPG1 is smaller than between QD1 and IPG2 and vice versa for QD2. With these results we can conclude, that we cut the 1D wire into two quantum dots that are parallel to each other.

An interesting aspect are the different capacitances of the two quantum dots to the in-plane gates and the backgate: $C_{BG,1} \sim 0.45$ aF and $C_{BG,2} \sim 0.03$ aF. This indicates a different size of the quantum dots which is in contrast to the AFM image of the completed device shown in Figure 5.9(a). From the geometry at the sample surface both QD should have the same size. Apparently QD1 is much larger than QD2 because the capacitance to the backgate depends mainly on the dot

areas. QD1 has probably the shape of a long box which is 200 nm wide and several 100 nm long. In contrast the smaller QD2 has probably a more circular form with a diameter of about 200 nm.

Measurement of the overall capacitances

To obtain the overall capacitances of the QDs in Figure 5.12 a greyscale-plot of the absolute value of the source-drain current I_{SD} of the device in Figure 5.9(a) is shown. The backgate-voltage V_{BG} and the source-drain voltage V_{SD} are varied and the IPGs constantly biased with $V_{IPG1} = -550$ mV and $V_{IPG2} = -330$ mV. We choose this in-plane gates voltages to achieve a high onset voltage V_{BG} for the Coulomb-blockade oscillations. In the grey-scale map Coulomb-blockade diamonds appear with two different sizes for QD1 and QD2. At high backgate-voltage $V_{BG} > 16$ V we observe many small diamonds – some are marked with black lines. By analysing the maximal width $V_{SD,max}$ we obtain the overall capacitance C_Σ of QD1 with $2e^2/C_\Sigma = eV_{SD,max}$ to $C_{\Sigma,1} \approx 250 \pm 10$ aF. A large diamond at $V_{BG} < 16$ V is marked

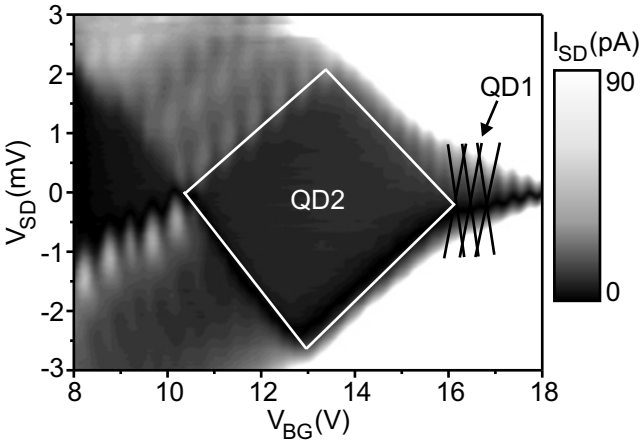

Figure 5.12: Absolute value of the current I_{SD} through the double-dot as a function of the backgate voltage V_{BG} and the source-drain voltage V_{SD} at $V_{IPG1} = -550$ mV, $V_{IPG2} = -300$ mV. At $V_{BG} < 16$ V the transport is dominated by QD2 (large coulomb-blockade diamond, indicated by white line). At $V_{BG} > 16$ V the current flows through QD1 and QD2 (small diamonds, black lines).

by white lines. We can attribute this diamond to QD2 with $C_{\Sigma,2} \approx 70 \pm 15$ aF. The capacitances differ by a factor of four. In Table 5.2 the results of the capacitance measurements are summarized.

However we can conclude that we succeeded in the stepwise fabrication of two parallel quantum dots. Please note, that from another point of view the subsequent fabrication of the device is also a diagnosis tool. The cutting of the RTD enables us to determine the properties of the 1D wire that showed the 2D-1D-2D resonant tunnelling. Here we find that the wire was asymmetrical located in the IPG-channel which leads us to the assumption that dislocations and inhomogeneities are present in the structure. One possible explanation is a wider depleted region around the groove defining IPG2 which is 3 nm deeper and slightly wider than the groove of IPG1. As shown in Section 4.2 the depletion width around the nanomachined lines increase with the depth and width of the groove.

We do not observe any clear signs of a coupling between the dots in the gate-gate characteristics in Figure 5.10(a) and Figure 5.11. The absence of discontinuities in the peak shifts as a function of the gate voltages underlines this assumption. The appearance of a sudden jump in the position of the Coulomb-blockade peaks would indicate that the electrochemical potential on one dot is changed by an additional charge on the second dot. In Figure 5.12 there is a modulation of the transport through QD2 with a period that would fit to the capacitively charging of QD1. The exact origin of these structures remain unclear at the moment.

As a consequence of our results we can conclude that QD1 corresponds to an area that fits to the geometric size extracted from the AFM image. The origin of the very small QD2 remains unclear. We already mentioned the wider depleted region around one of the nanomachined grooves that could lead to a smaller dot. An additional effect might be a local potential minimum induced by some disorder leading to a dot with a rather small confinement potential and thus to a higher charging energy.

As stated above, we can exclude that a quantum-dot molecule is formed out of the two quantum dots since the tunnel coupling between the dots is lower than their coupling to the contacts and the results of the transport measurements. To observe a formation of a coherent state a modification of the geometry of the device is necessary. The dot size should be reduced to below one micron and the inter-dot separation should be as low as possible to increase the interaction strength.

5.3 Conclusion

In the first part of this chapter the constant-interaction model for single-charge tunnelling has been introduced. As an example for a single-electron transistor we fabricated a device with local oxidation. The SET contains a few hundred electrons, which makes the constant interaction model applicable for the description of the main features observed in the transport characteristic. The SET shows the Coulomb-blockade oscillations and the charge stability diagram with almost constant parameters over a wide voltage range.

In the second part we demonstrated that the AFM-based nanolithography provides an relatively easy and controlled approach to create parallel quantum dots. The device was stepwise fabricated with a combination of controlled nanomachining and local oxidation. The dots were defined by splitting a quasi-one-dimensional resonant tunnelling diode in two separate zero-dimensional regions. An analysis of the transport measurements of the two quantum dots allowed the identification of the specific Coulomb-blockade oscillations of each dot. We showed that the current could be directed through both quantum dots separately with applying high negative gate voltages to the respective in-plane gates.

These experiments show that the combination of controlled nanomachining and local oxidation with an atomic force microscope is a straightforward approach to the fabrication of robust mesoscopic devices. The shape and geometry of the gates and source-drain contacts is only limited by the number of contacts to the Hall bar. The possibility to change the device characteristic in a step-by-step process after each transport measurement is very promising especially to study chaotic cavities with complex geometries.

6 Aharonov-Bohm effect in an open quantum ring

In this chapter we will show measurements on a quantum ring with a diameter of below 450 nm fabricated by nanolithography using an atomic force microscope (AFM). With direct local oxidation by an AFM tip a ring geometry was directly written into a GaAs/AlGaAs-heterostructure. The exceptionally short circumference of the ring reduces decoherence due to scattering. Our transport measurements in the open regime show only one transmitting mode and Aharonov-Bohm oscillations with more than 50% modulation of the ring conductance. In-plane gates are used to tune the Fermi wavelength in the arms of the interferometer and thus to control the phase of the Aharonov-Bohm effect.[1]

[1] Parts of this chapter have been already published in U. F. Keyser, S. Borck, R. J. Haug, M. Bichler, G. Abstreiter, and W. Wegscheider, *Aharonov-Bohm oscillations of a tuneable quantum ring*, Semiconductor Science and Technology **17**, L22-L24 (2002), preprint: cond-mat/0202403.

6.1 Aharonov-Bohm effect

6.1.1 Introduction

In quantum mechanics electrons are described by a wave function Ψ. This leads to many phenomena unexpected from the classical description of electrons as point-like particles. One of the most striking effects, tunnelling through a potential barrier, has been investigated in an earlier section of this thesis, see Chapter 2. The wave nature of the electrons has an even more surprising consequence. Electrons can interfere with themselves if they are transmitted through a ring structure like the one shown in Figure 6.1. Such a ring acts as a beam splitter for the incident electronic wave function. Ψ will split into an upper and a lower part that traverse the respective ring arms. If we assume that the phase coherence length l_ϕ is long compared to the circumference $\mathcal{C}$ of the ring there will be an interference between the two parts at the ring exit. For a perfectly symmetric ring the phase difference is zero and thus we have constructive interference.

The relative phase in the ring arms is controlled by applying a perpendicular magnetic field $\vec{B} = \nabla \times \vec{A}$. The vector potential $\vec{A}$ leads to an additional phase factor for the wave function in both arms [86]

$$\exp\left[-i\frac{e}{\hbar}\int_C d\vec{l}\cdot\vec{A}\right] = \exp\left(-i2\pi\frac{\phi}{\phi_0}\right). \tag{6.1}$$

$\phi = \int_C d\vec{l}\cdot\vec{A}$ is the magnetic flux through the ring and $\phi_0 = h/e$ the

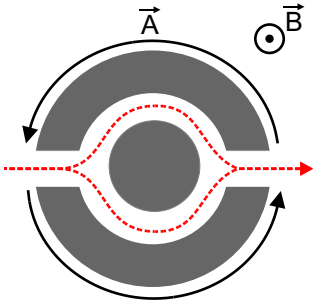

Figure 6.1: A ring structure splits the incident electronic wave function Ψ into two parts that interfere at the ring exit if scattering is absent. The vector potential $\vec{A}$ influences the relative phase of the two parts of Ψ at the ring exit.

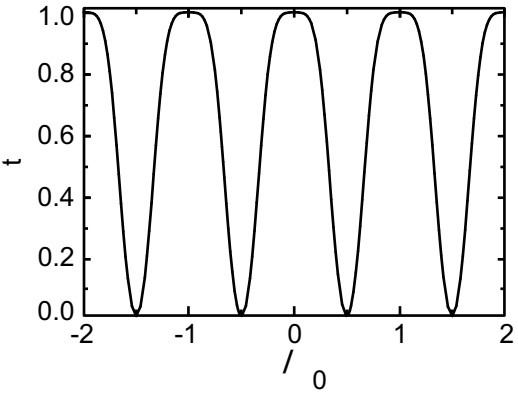

Figure 6.2: Transmission t through a symmetric ring structure as function of the flux ϕ threading the ring. $\phi_0 = h/e$ is the flux quantum.

flux quantum. According to formula 6.1 the wave traversing through the lower part of the ring in Figure 6.1 picks up a phase $\pi\phi/\phi_0$ whereas the part in the upper arm changes its phase by the negative of the above because it moves in the opposite direction relative to $\vec{A}$. The interference at the ring exit leads then to an oscillating phase between 0 and 1

$$\exp(-i\pi\phi/\phi_0) + \exp(i\pi\phi/\phi_0) = 2\cos(\pi\phi/\phi_0). \tag{6.2}$$

From this equation follows that the probability to find an electron at the ring exit oscillates with $\cos^2(\pi\phi/\phi_0)$. According to this result the transmission of the ring equals one if $\phi = n\phi_0$, with $n = 0, 1, 2, ..$. This means for a transport measurement that each time the magnetic flux ϕ threading the ring is an integer multiple of ϕ_0 the conductance G will be maximal. This effect was predicted by Bohm and Aharonov in 1959 [11] and first experimentally observed by Chambers in an electron beam diffraction experiment [87].

The first Aharonov-Bohm oscillations with a periodicity of h/e in a condensed matter device were observed in a transport experiment on very small Au-loops [88]. The high electron densities in metals lead to an averaging of the Aharonov-Bohm oscillations of many different modes and thus to a reduced amplitude. Even at mK temperatures the magnitude of the Aharonov-Bohm oscillations lies below 1% of the signal. Because of their relatively low carrier concentrations in the two-dimensional electron gas, GaAs/AlGaAs-heterostructures were used as

a substrate for the fabrication of ring systems with only a few transmitting modes, see e.g. [89, 90, 91, 92] and references therein. For processing the samples usually well-established techniques like electron beam lithography and wet-chemical etching were utilized. Recently Aharonov-Bohm oscillation with an amplitude of 30% was observed in a vertical interferometer [93]. Recent papers claim to have found experimental evidence for a spin-induced Berry phase in rings realized in other material systems [94, 95].

6.1.2 Transmission through a symmetric ring

In principle for all the above experiments the basic considerations of the introduction can be applied. For a more accurate description of (real) rings a calculation based on scattering matrix theory yields a transmission probability t through a symmetric ring with no elastic scattering:

$$t(\chi, \Phi, \epsilon) = \frac{4\epsilon \, \sin^2 \chi \, \cos^2(\Phi)}{[a^2 + b^2 \, cos^2(\Phi) - (1-\epsilon) \, cos^2\chi]^2 + \epsilon^2 \, sin^2\chi}, \qquad (6.3)$$

with $\Phi = \pi\phi/\phi_0$. ϵ measures the scattering at the ring exit and entrance and $\chi = k_f\mathcal{C}/2$ the product of the Fermi wave vector k_F and the circumference $\mathcal{C}$ of the ring. An exact derivation of the above equation can be found e.g. in Ref. [96, 97]. a^2 and b^2 are coefficients that directly result from the scattering matrix and depend on ϵ. In this chapter we work with a device in the limit of open point contacts. For such quantum point contacts in the ballistic regime we have to choose $\epsilon = 0.5$ which results in $a^2 = 1/4$ and $b^2 = 1/4$ [97].

In Figure 6.2 a plot of the transmission t as a function of ϕ/ϕ_0 is shown. The phase coherence length l_ϕ is infinite and χ was set to $\pi/4$. t varies between $t = 0 \Leftrightarrow G = \min$ and $t = 1 \Leftrightarrow G = \max$ as a function of the applied magnetic field. Please note the periodicity of the curve with ϕ_0.

6.1.3 Transmission through an asymmetric ring

For a realistic device equation 6.3 has to be modified because there exists usually a length difference of the ring arms ΔL. This leads to an additional phase difference δ between the two parts of the wave function of $\delta = k_F\Delta L$. Considering this in the model the transmission

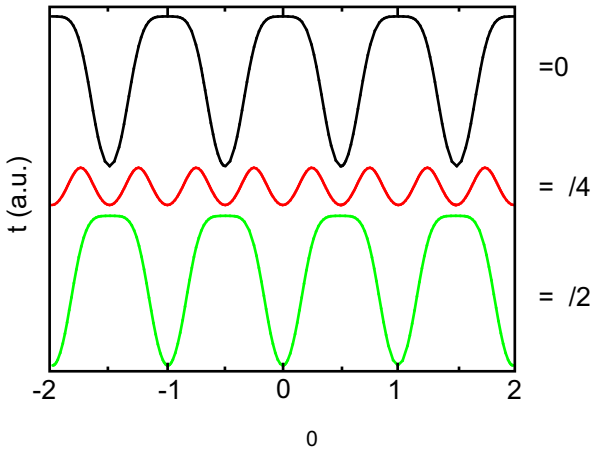

Figure 6.3: Transmission probability through an asymmetric biased ring as function of the magnetic flux ϕ/ϕ_0 for $\delta = 0, \pi/4, \pi/2$ and $\chi = \pi/4$. The curves are offset for clarity. The maximum at $\phi = 0$ for $\delta = 0$ changes into a minimum for $\delta = \pi/2$. Note the frequency doubling and the reduction of the oscillation amplitude for $\delta = \pi/4$.

probability has to be modified to [98, 97]

$$t(\chi, \Phi, \delta, \epsilon) = \frac{4\epsilon\,[sin^2\chi\, cos^2\Phi + sin^2\Phi\, sin^2\delta - sin^2\chi\, sin^2\delta]}{[a^2\, cos2\delta + b^2\, cos^2\Phi - (1-\epsilon)\, cos^2\chi]^2 + \epsilon^2\, sin^2\chi}. \quad (6.4)$$

Please note that equation 6.3 is a special case of the above equation for $\delta = 0$. Equation 6.4 also applies when e.g. in a symmetric ring the Fermi wave length is different in the ring arms. This can be achieved by e.g. an outer gate voltage that couples to one ring arm. This changes the Fermi wave length and thus the effective arm length. As a consequence δ is controlled by an outer parameter.

The results of calculations with equation 6.4 for $\delta = 0, \pi/4, \pi/2$ and $\chi = \pi/4$ are shown in Figure 6.3. As mentioned above, for $\delta = 0$ we get the same oscillations with a maximum at zero flux (upper curve) as for the symmetric case in Figure 6.2. $\delta = \pi/4$ leads to a signal with halved period and a much smaller amplitude (central curve). Additionally the maximum at zero magnetic field changes into a minimum indicating a phase change of the wave function in the ring. This becomes even more clear when looking at the third and lowest curve in Figure 6.3

with $\delta = \pi/2$. The original curve reappears but is shifted by half a period. The occurrence of the phase jumps is periodic with a period $\delta = \pi$.

The tuning of the phase at zero magnetic field is sometimes called electric or electrostatic Aharonov-Bohm effect. It seems as though one can influence the phase of the wave function with the scalar potential of an electric field. But the underlying process is completely different from its magnetic pendant. Whereas the vector potential $\vec{A}$ changes directly the phase factor in Ψ the electric field changes the Fermi energy and thus the wave length and energy of the incident electron.

In the above equation the phase coherence length l_ϕ is not considered. In a real device l_ϕ will be finite because of scattering, finite temperatures, and defects. If an electron is scattered during the passage in one ring arm this can be considered as a "which-path" measurement. The interference pattern is destroyed [99] and leads to a reduced oscillation amplitude of the conductance in the Aharonov-Bohm effect.

6.2 Sample fabrication

In this chapter we present data measured on an asymmetric quantum ring with two tuneable point contacts. The ring was fabricated using an atomic force microscope (AFM) as nanolithographic tool. With the design of the quantum ring we are able to investigate the interplay between electron interference and single-electron charging effects on the same device. We focus on the ballistic regime, where the conductance of the point contacts G lies around $2(e^2/h)$. The quantum ring acts in this regime as an electron interferometer. Measurements in the Coulomb-blockade regime with closed point contacts ($G < 2(e^2/h)$) will be studied later in this thesis, see Chapter 7.

For the fabrication of the device we used a GaAs/AlGaAs-heterostructure consisting of a 5 nm thick GaAs cap layer, 8 nm of AlGaAs, the Si-δ-layer, a 20 nm wide AlGaAs barrier and 100 nm of GaAs (from top to bottom, wafer 71000, Figure 3.2). The two-dimensional electron gas (2DEG) is located 34 nm below the surface with a density of $4.3{\cdot}10^{15}$ m^{-2} and a mobility of 42 m^2/Vs. The mean free path of the electrons is $l_\phi \sim 4.6$ μm. A Hall-bar geometry was defined by standard photolithography and wet-chemical etching.

By applying a negative voltage to a conducting AFM tip the GaAs is oxidized. Underneath the oxide the 2DEG is totally depleted and thus

one can directly write electronic devices into the 2DEG. A detailed description of the process is given in Chapter 4.3. An AFM image of the completed ring structure is shown in Figure 6.4(a). The oxide lines insulating the in-plane gates from the ring were written with an oxidation current of 1 μA. The relevant geometric dimensions of the ring are its outer diameter of 450 nm, measured from the inner edge of the oxide lines across the ring, and the diameter of the central oxide dot of 190 nm. The constrictions that connect the ring to the source and drain contacts are both 150 nm wide, in the following these will be addressed as point contacts.

The electrochemical potentials of the ring and the conductance through the point contacts are tuned with the two in-plane gates (IPG) that are marked in Figure 6.4(a) with IPGA and IPGB. Please note, that IPGA has a much shorter boundary to the upper ring arm than IPGB to the lower. From the AFM image one can directly see that the structure is asymmetric.

Another important detail is the gate coupling to the point contacts. Whereas IPGA directly influences both ring exits, IPGB controls only the upper point contact. The device was characterized in a ^{3}He-^{4}He-dilution cryostat. In the following we will keep V_A (voltage applied to IPGA) at a constant value of 95 mV. The cryostat was kept at a base temperature of $T_b = 30$ mK throughout the measurements if not stated otherwise in the text. The electronic temperature lies below 50 mK as measurements in the Coulomb-blockade regime indicate.

A schematic picture of the ring is shown in Figure 6.4(b). The solid

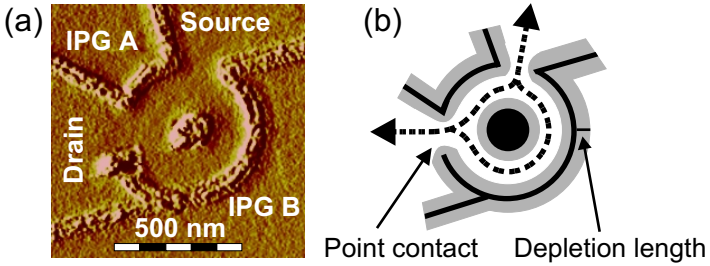

Figure 6.4: (a) AFM image of the ring-structure. IPGA, IPGB denote the in-plane gates. (b) Schematic picture of the ring. The solid lines indicate the insulating lines and the grey area the width of the depleteion in the 2DEG. The dashed trajectory has a diameter of $d_e \sim 300$ nm.

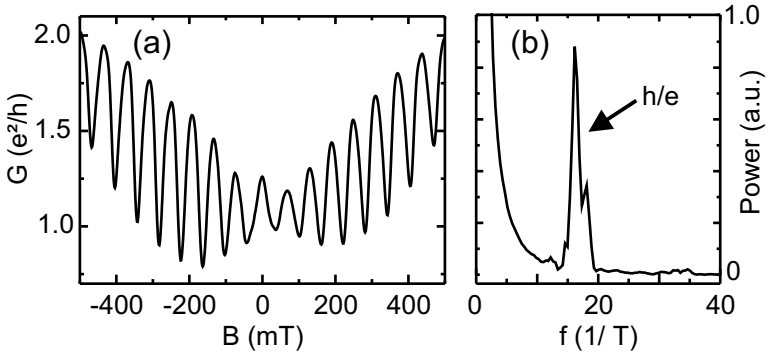

Figure 6.5: (a) Conductance G through the open quantum ring as function of the magnetic field B at $V_A = 95$ mV, $V_B = 120$ mV. (b) The Fourier transformation of the data shows one distinct peak at 16 ± 1 T^{-1}.

lines depict the oxide and the light grey areas around them the depletion width of some ten nanometers in our structures (see Chapter 5.1). We illustrate the expected electron path in the open transport regime with the dashed lines. The diameter of this electronic path is ~ 300 nm. Since the phase coherence length in the unstructured 2DEG is $l_\phi = 4.6$ μm and the circumference of the ring is only $\mathcal{C} = 1.0$ μm we assume that the ring is in the ballistic regime and neglect effects of inelastic scattering.

Figure 6.5(a) shows the conductance $G(B)$ of the quantum ring in the open regime with $V_A = 95$ mV and $V_B = 120$ mV ($R < h/e^2$) in a perpendicular magnetic field B. We observe Aharonov-Bohm oscillations with an oscillation amplitude of more than 50%. This exceptional high value was not reported before in transport experiments in semiconductor rings. We extract a period $\Delta B \sim 60$ mT from the data in Figure 6.5(a). The clear oscillations without any distortions together with the high amplitudes indicate that we have very few conducting channels in the ring.

For a further analysis of the periodicity we use a Fourier transformation of the data. The power spectrum of the measurement in Figure 6.5(a) as a function of the oscillation frequency f is shown in Figure 6.5(b). The dominating feature is at a frequency of 16/T. This corresponds to $\Delta B \sim 60$ mT and indicates that a flux quantum $\phi_0 = h/e$ enters the area enclosed by the electron paths every ~ 60 mT. Each

additional flux quantum in the ring changes the phase by 2π and thus we observe a full oscillation period. We estimate the diameter of the electron orbit in our ring from the period of $\Delta B = 1/f$

$$\phi_0 = \frac{1}{4}\Delta B \pi d_e^2 \Rightarrow d_e = 2\sqrt{\frac{h}{\pi e \Delta B}}. \tag{6.5}$$

With $\Delta B \sim 60$ mT a flux quantum is added to the ring area and we determine the diameter d_e of the dominating electron orbit in our ring to $d_e \sim 300$ nm. This fits perfectly the geometry of our device. The observation of only one dominant frequency at 16/T indicates that only a single conducting channel is present in this voltage regime.

6.3 Gate voltage dependence

6.3.1 Aharonov-Bohm oscillations

In this paragraph we will study the ring conductance in the range of 70 mV $< V_B <$ 100 mV and $V_A = 95$ mV. In Figure 6.6(a) we show again ring conductance $G(V_B)$ at $B = 0$ as a function of V_B. We observe an oscillating signal which has about the same amplitude as the Aharonov-Bohm oscillations depicted in Fig. 6.5(a).

The average peak-to-peak distance is $\Delta V_B \sim 3.5$ mV. The grey-scale plot in Figure 6.6(b) shows G as a function of B and V_B. As usual, black(white) stands for high(low) G. The arrow marks zero magnetic field $B = 0$ that is the symmetry axis as expected for a two-terminal measurement. The alternating pattern of high and low conductance as a function of V_B and B is due to the Aharonov-Bohm effect. A check of the periodicity of the data in Figure 6.6(b) is obtained with Fourier transformations over the whole gate voltage range. The resulting power spectra are depicted in Figure 6.7 in a grey-scale map as a function of V_B and the frequency f. Here we chose a logarithmic scale for the grey-scale. This makes the higher frequency components visible that are suppressed by more than a factor of 10^3 compared to the leading frequency of 16/T as known from Figure 6.5(b).

The dominating feature in Figure 6.7 is a vertical black line around $f_0 \sim 16$/T. At 10/T, 26/T and ~ 34/T there appear weaker frequency components, the latter is probably the second harmonic of the base frequency f_0 where the electrons traverse the ring twice.

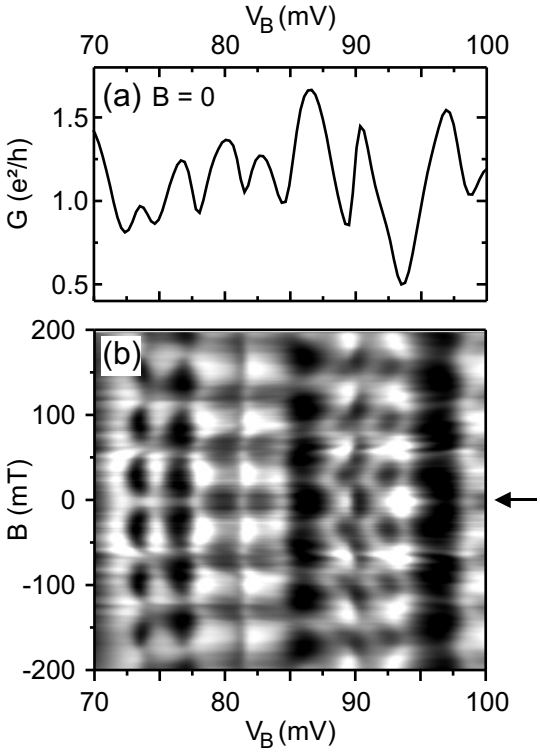

Figure 6.6: (a) Conductance G through the open quantum ring at $B = 0$ and $V_A = 95$ mV. (b) Greyscale plot of $G(V_B, B)$ for the device in a perpendicular magnetic field. The data in the upper window was measured along the line indicated by the arrow.

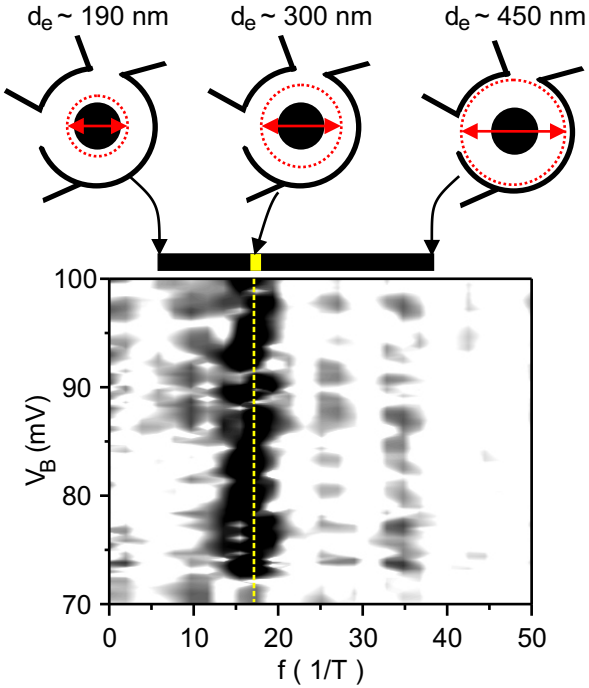

Figure 6.7: Logarithmic grey-scale plot of the power-spectrum of the data in Figure 6.6(b) as a function of V_B. We observe one dominating frequency component at 16/T over the whole range. The solid line at the top of the structure marks the boundaries for the frequency defined by the device geometry. This is visualized in the schematic pictures above. These show electron paths through the ring with diameters $d_e = 190$ nm, $d_e = 300$ nm, and $d_e = 450$ nm. The image in the center for $d_e \sim 300$ nm corresponds to the base frequency f =16/T.

We estimate the lowest frequency component of 7/T by calculating the expected periodicity with equation 6.5 for $d_e = 190$ nm. This result neglects any effects from the finite depletion length. There exists a maximum frequency of 37/T defined by the maximal geometric diameter of $d_e = 450$ nm. But electrons can also pass the ring twice which doubles the enclosed area. We observe this effect only weakly in the spectra of the ring in Figure 6.7. The black line depicted directly above the grey-scale plot indicates these boundaries. For clarification three schematic pictures of the ring with electron paths of different diameters d_e are depicted. The picture in the center gives an impression for the situation in the ring with $d_e \sim 300$ nm which corresponds to the base Aharonov-Bohm frequency of 16/T.

Following the discussion of asymmetric ring structures we expect to observe phase jumps in the Aharonov-Bohm oscillations in our quantum ring. A closer look at the grey-scale plot in Figure 6.6(b) already indicates this. For a clear demonstration of this characteristic we depicted the magneto-conductance $G(B)$ at four different gate voltages V_B =86.6, 89.4, 90.3, and 93.4 mV in Figure 6.8(a). At $V_B = 86.6$ mV (lowest curve) G has a maximum at $B = 0$ whereas at $V_B = 89.4$ mV the curve is shifted by half a flux quantum and shows a minimum at $B = 0$. Thus the phase of the wave function changed by π by applying an outer gate voltage. The same occurs between each pair of the four curves which leads to three phase jumps in this voltage range. The corresponding conductance trace $G(V_B)$ at $B = 0$ is shown in Figure 6.8(b). The gate voltages of the four traces in Figure 6.8(a) are denoted by the squares. The phase jumps that occur at V_B =88.6., 90.0, and 91.7 mV are marked by the arrows.

We have shown in Chapter 6.1.3 that a phase jump comes along with a frequency doubling and a damping of the Aharonov-Bohm oscillations. This latter characteristic should lead to a vanishing of the 16/T peak at the gate voltages where we get $\delta = \pi/4$. Indeed we observe this behaviour for our ring in the power spectra shown in Figure 6.8(c). The graph shows the power spectra of the magneto-conductance data between 86 mV $\leq V_B \leq$ 94 mV. The huge peak corresponds again to the 16/T oscillation of the 300 nm orbit. Both the phase jumps at $V_B = 88.6$ mV and $V_B = 91.7$ mV lead to a suppression of the main frequency component by almost a factor of 10. The phase "jumps" abruptly between two points of the measurements but the damping of the oscillation already starts before. We observe the maximal signal at the gate voltages of the measurements in Figure 6.8(a).

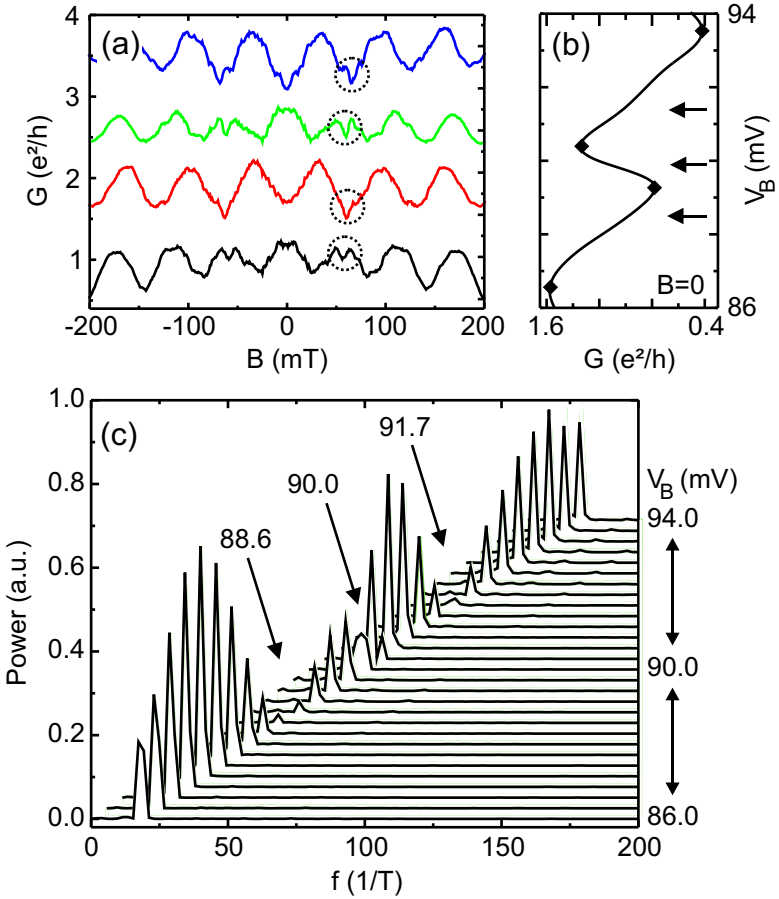

Figure 6.8: (a) Conductance G as function of the magnetic field B at four gate voltages $V_B = 86.6, 89.4, 90.3, 93.4$ mV from bottom to top. Between each curve pair the phase changes by π. The curves are offset for clarity. (b) G at $B = 0$ as function of V_B, the exact positions of the phase jumps are marked by the arrows. The gate voltages of the traces in (a) are marked by the black diamonds. (c) Power spectra for all gate voltages of (b), the base frequency of the ring 16/T vanishes or is suppressed at the phase jumps indicated by the arrows at $V_B = 88.6, 90.0, 91.7$ mV. The curves are offset for clarity.

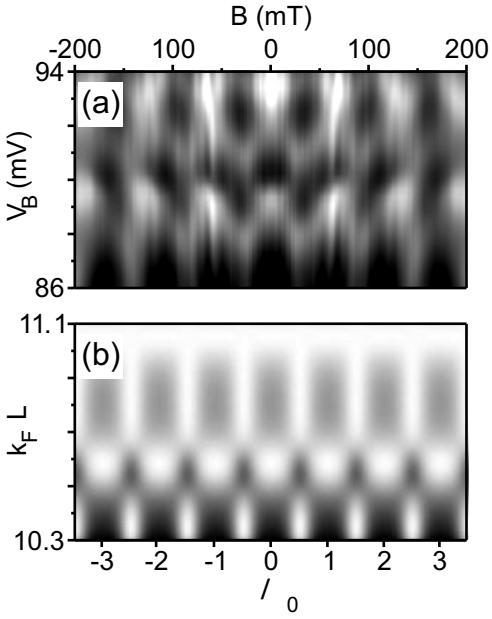

Figure 6.9: (a) Grey-scale plot of the conductance G through the ring as function of B and 86 mV $< V_B <$ 94 mV, $V_A = 95$ mV. (b) Grey-scale plot of the calculated transmission $T(\chi = \pi/4, \Phi, \delta, \epsilon = 0.5)$ for an asymmetric ring with varying δ (see text).

This is completely different for the situation at $V_B = 90.0$ mV where we see just a short reduction by a factor of two or three, Figure 6.8(c). This is understood if we look back at the dependence of G on V_B at $B = 0$, Figure 6.8(b). Whereas there is a relatively smooth gradient between the first maximum and the first minimum the rise to the second maximum is rather fast. Thus the transition from a minimum at $B = 0$ to a maximum has to be faster than during the other phase changes. With a finer resolution of the gate voltage we should be able to observe the damping at this phase jump as well.

We don't observe a real frequency doubling in the Fourier spectra because the amplitude of the Aharonov-Bohm oscillations is almost totally suppressed at the phase jumps. The reason for this specific characteristic of our ring will be discussed in the next paragraph. Before we want to comment on the small dashed circles at $B \sim 50$ mT in Figure 6.8(a). They mark small dips in each of the conductance traces

$G(B)$. The exact position barely shows any dependence on V_B. At first one could believe that we see a frequency doubling of the Aharonov-Bohm signal. But the dip appears only at the first maximum and at higher V_B even in the minima of $G(B)$. We attribute this to a specific characteristic of the ring spectrum.

Modelling of the data

In Figure 6.9 again a grey-scale plot of $G(V_B)$ is shown. The voltage range is the same as discussed above. The phase jumps observed in Figure 6.8(a) are indicated by the alternating pattern of high and low conductance in vertical direction. At the bottom we have a maximum (black) at $B = 0$ that changes into a minimum (white) etc. With equation 6.4 we tried to reproduce the key features of the quantum ring in this voltage regime in the strong coupling limit $\epsilon = 0.5$. Since we vary the in-plane gate voltage we will change the relative phase between the two ring arms and thus introduce an effective length difference ΔL. This was taken into account by introducing the asymmetry parameter $\delta = k_F \Delta L / 0.15$ which leads to a rather strong dependence of δ on the gate voltage. Figure 6.9(b) shows a grey-scale map of the transmission probability of the ring calculated with formula 6.4. In the depicted range there are three phase jumps and the signal starts with a maximum. The absence of a frequency doubling of the Aharonov-Bohm oscillation between the phase jumps in the calculated data is related to the very fast change of δ.

Since we do not know the exact dependence of k_F on V_B we cannot map the axis of the simulation to the data. Please note, that this is not a fit but a mere phenomenological comparison of a measurement to an idealized calculation. However, this allows to check whether we have to consider any other effects to explain the behaviour of our device in this regime. Apparently this is not necessary to understand the main features of the transport in region 2.

6.3.2 Ring conductance at lower gate voltages

In Figure 6.10(a) $G(V_B)$ is depicted again at zero magnetic field $B = 0$ and $V_A = 95$ mV. But in this case we reduce V_B to 40 mV. Above $V_B > 70$ mV we observe the oscillating signal already discussed in the preceding paragraph. But apparently $G(V_B)$ divides into two regions which differ by the shape of the measured resonances.

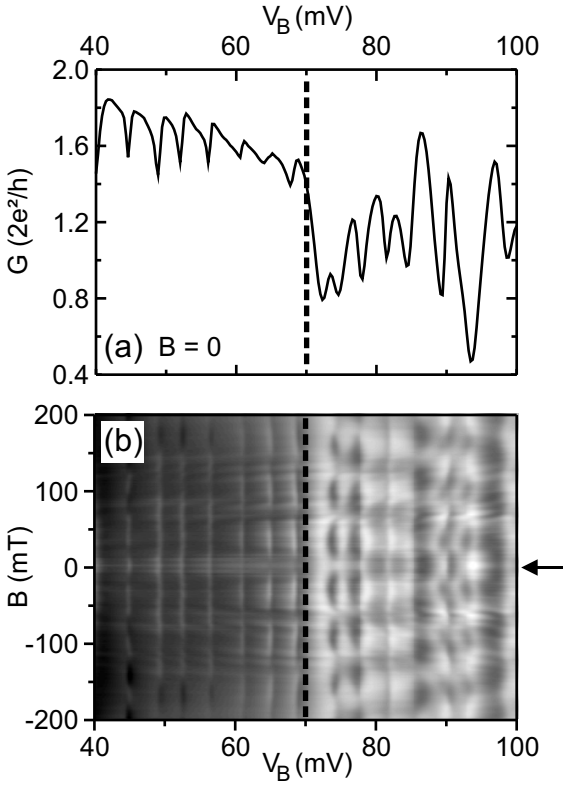

Figure 6.10: (a) Ring conductance G as a function of gate voltage V_B at $V_A = 95$ mV, $V_{SD} = 0$, $B = 0$, and $T = 30$ mK. Note the change in the shape of the resonances in the two regions of the curve. (b) Grey-scale plot of G as function of V_B and B, for $V_B > 70$ mV we observe Aharonov-Bohm oscillations. These are only present at the dips in the trace for $V_B < 70$ mV.

Whereas for $V_B > 70$ mV the peaks are smooth and rounded for $V_B < 70$ mV relatively sharp dips appear in the conductance with almost the same period of $\Delta V_B \sim 3.5$ mV. The transition between the two regions at $V_B = 70$ mV is accompanied by a fast *decrease* of G from $\sim 1.7\ e^2/h$ to $\sim 0.8e^2/h$.

In Figure 6.10(b) a grey-scale plot of the magneto-conductance G as a function of V_B and B is shown, black indicates a maximum and white a minimum in the conductance. Please note that this is the original data. Because of the high oscillation amplitudes we don't have to subtract any slowly varying background. As expected from the measurements at $B = 0$ this plot also consists of two regions. The data for $V_B > 70$ mV is depicted already in Fig. 6.6(b). Here we adjusted the grey-scale to maximize the contrast for the whole plot.

For $V_B > 70$ mV we observe Aharonov-Bohm oscillations for the whole gate gate voltage range. But for $V_B < 70$ mV these appear only at the distinct gate voltages corresponding to the "anti"-resonances in Fig. 6.10(a). Between these dips $G(B)$ barely depends on B which leads to the large grey areas.

We further analyzed the "anti"-resonances in the conductance by performing Fourier transformations on the data. The corresponding power spectra of $G(B)$ in this voltage range are shown in Figure 6.11(a) for 40 mV$\leq V_B \leq$70 mV. The plot shows the expected maximum at $f_0 \sim 16$/T only at the gate voltages corresponding to the minima in the conductance. This coincidence is underlined by the adjacent Figure 6.11(b) that shows $G(V_B)$ at $B = 0$. The gate axis was scaled to fit the offset of the curves in Figure 6.11(a).

One possible explanation for the suppression of the Aharonov-Bohm effect in this voltage regime might be the asymmetric gate bias. Because the voltage at $V_B < 70$ mV is always smaller than the constant $V_A = 95$ mV applied to IPGA the electron trajectories concentrated in the upper ring arm. The incident electrons can leave the ring directly through the other point contact without passing the lower arm. This focusing effect is known from point contacts in series [100]. However, this model explains only the absence of the interference pattern. For the "anti"-resonances in $G(V_B)$ with their peculiar shape we have to find another explanation.

From the analysis of the Aharonov-Bohm measurements we have strong indications that only one subband is occupied – at least in the lower ring arm. However, the conductance through the ring in region 1 is almost $2(e^2/h)$ and even exceeds $2(e^2/h)$ when we apply a perpendic-

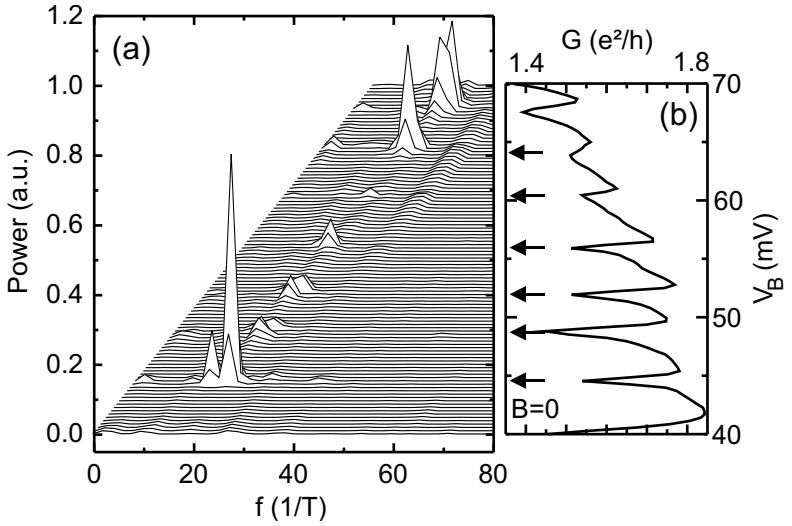

Figure 6.11: Fourier spectra of the measurements in Figure 6.8 for 86 mV $< V_B <$ 94 mV, $V_A = 95$ mV. The curves are offset for clarity. At $V_B \sim 88.5$ mV and 91.5 mV the peak at 16/T vanishes almost completely, which indicates a phase jump by π. At $V_B \sim 90.0$ mV we observe another phase jump but the power spectrum shows only minor changes.

ular magnetic field, shown in Fig. 6.13(b). If we take into account that we are performing two-terminal measurements we have to subtract a series contact-resistance ranging from a few hundred Ω to 1 kΩ to get the "pure" conductance of our ring. The corrected conductance G' exceeds $2(e^2/h)$ which requires that more than one subband is occupied because each subband has a conductance of $2(e^2/h)$. This contradiction to the results of the Aharonov-Bohm oscillations is overcome if we assume that the upper arm transmits two subbands whereas the lower arm contains only one subband. This is depicted in the diagram shown in Figure 6.12(a).

The AFM image of the ring in Figure 6.4(a) provides us a possible explanation for this assumption. It is barely visible but the oxide dot is not perfectly centered in the ring and shifted some 10 nm wide to the lower right. This reduces the width of the lower ring arm in comparison to the upper one. Additionally we will have more electrons in the vicinity of the point contacts which further increases the electron

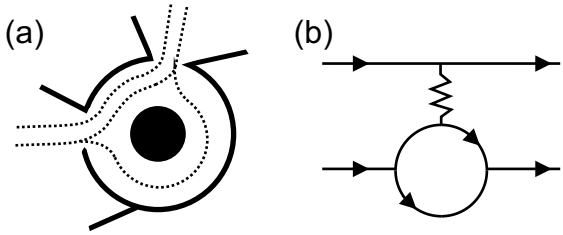

Figure 6.12: (a) Schematic picture of the ring shows the paths of the electrons in the ring that interact with the state around the center. (b) Simplified picture of conducting channels that interact with a bound state in the ring.

density in the shorter upper arm. The Fermi wave length $\lambda_F \sim 40$ nm in the unstructured 2DEG is roughly factor two smaller than the reduced arm width of the structure. The effective electronic width will be smaller than 100 nm because of the depletion length in the range of some ten nm. With the considerations of Chapter 4.2 for ballistic point contacts we conclude that maximal two subbands can be occupied in the ring.

With the above assumptions we can explain the appearance of the

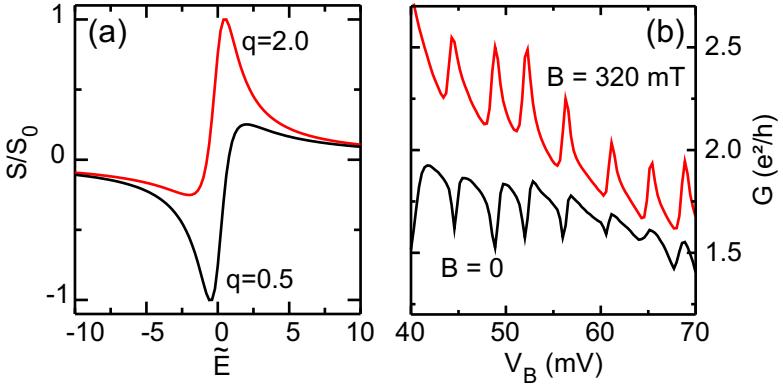

Figure 6.13: (a) Fano resonance for $q = 0.5$ (lower curve) and $q = 2.0$ upper curve as function of $E - E_{\mathrm{res}}$. (b) Conductance $G(V_B)$ in region 1 at $B = 0$ (lower curve) and $B = 320$ mT (upper curve). The sharp dips change into maxima in the field. The curves are offset for clarity.

dips in $G(V_B)$ observed in Figure 6.10. In principle the picture in Figure 6.12(a) shows two interacting states that pass a resonant bound state around the center of the ring. Whereas the upper channel is transmitted directly through the structure the lower path is "scattered" at the ring center.

A better representation of this circumstance is depicted in Figure 6.12(b) by two channels passing a resonant state (depicted by the circle), whereas one is transmitted directly or non-resonantly the other may be in resonance with the circular state only if its energy matches the resonant energy. Both channels will interfere/interact in the upper ring arm which is depicted by the zig-zag line.

The dips in $G(V_B)$ appear at distinct gate voltages corresponding to the resonances of the bound state. Whereas the phase of the non-resonant state changes slowly with V_B the lower channel will pick up a phase shift by π every time it fits to a resonance on the ring. This phase shift is an inherent characteristic of all resonant processes in physics.

The interference between a resonant and non-resonant state is known from e.g. nuclear or atomic physics. In the latter one can observe resonances of an electron that is temporarily bound at an He-atom and then decays [101]. The interference between two channels results in spectra with resonant lines shaped similar compared to the ones in our ring. In general these lines are described by the following expression proposed by Fano in 1964 [102]

$$S \propto \frac{(\tilde{E}+q)^2}{\tilde{E}^2+1}. \tag{6.6}$$

q is a parameter that describes the relative phase between the two paths. $\tilde{E} = (E - E_{\mathrm{res}})/(\hbar\Gamma/2)$ is the dimensionless detuning of the energy E of the incident electrons from the energy E_{res} of the resonant state. $\hbar\Gamma$ measures the line width of the resonance. The left-hand side of Figure 6.13 depicts two so-called Fano resonances for $q = 0.5$ and $q = 2.0$. The curves were normalized to their respective maximum S_0. The difference in q leads to a change from a dip to a peak. For comparison with the resonances in region 1 we show a measurement in Figure 6.13(b) at $B = 0$ (lower curve) and $B = 320$ mT (upper curve). The curves were offset for clarity. Apparently the line shape is adjustable in our experiment by variation of the outer magnetic field. The "anti"-resonances at $B = 0$ in Figure 6.13(b) evolve into maxima at $B = 320$ mT. This is an indication that the above picture might be applicable for the description of our system.

These so-called Fano resonances were studied in recent experiments on quantum dots [103, 104]. But the authors could not explain the exact nature of the non-resonant channel. Our design of the ring gives us a better control over the relevant parameters, namely q. For further investigations of the properties of this type of resonances one can for example tune the coupling between the resonant and the non-resonant state with the gate voltage applied to gate A.

In this context the transition at $V_B \sim 70$ mV between the two transport regimes marks a fundamental change in the electronic structure of the ring. The stronger the coupling grows this might lead to an overlap and thus to strong interaction between the two subbands. The drop in the conductance by almost 50% is probably caused by the longer stay of the electrons in the device due to the longer path.

6.4 Conclusion

In this chapter we discussed the Aharonov-Bohm effect in an asymmetric quantum ring with a diameter of below 450 nm. The analysis of the data with Fourier transformation indicates that we have only one interfering subband in the ring. This leads to a modulation of the conductance of more than 50%, a value not reported before in transport experiments in semiconductor rings. The electron orbit extracted from the periodicity of the Aharonov-Bohm effects fits perfectly to the ring geometry. The attached in-plane gates allow to tune the phase of the Aharonov-Bohm effect at zero magnetic field and we observed the typical sharp phase jumps by π that are related to the asymmetry of our device.

Finally we showed that the line-shape of the resonances in the quantum ring is controlled by an outer gate voltage. We found first indications for a resonant bound state that couples to the directly submitted electrons and leads to a Fano like characteristic.

7 Kondo effect in a quantum ring

A small quantum ring with less than 10 electrons was studied by transport spectroscopy. For strong coupling to the leads a Kondo effect is observed and used to characterize the spin structure of the system in a wide range of magnetic fields. At small magnetic fields Aharonov-Bohm oscillations influenced by Coulomb interaction appear. They exhibit phase jumps by π at the Coulomb-blockade resonances. Inside the Coulomb-blockade regime the Aharonov-Bohm oscillations can also be studied due to the finite conductance caused by the Kondo effect. Interestingly, the maxima of the oscillations show linear shifts with magnetic field and gate voltage.[1]

[1] Parts of this chapter were published in U. F. Keyser, S. Borck, R. J. Haug, M. Bichler, G. Abstreiter, and W. Wegscheider, *Aharonov-Bohm oscillations of a tuneable quantum ring*, Semiconductor Science and Technology **17** L22-L24 (2002), preprint: cond-mat/0202403. The main part of this chapter is submitted: U. F. Keyser, C. Fühner, S. Borck, R. J. Haug, M. Bichler, G. Abstreiter, and W. Wegscheider, *Kondo effect in a few-electron quantum ring*, preprint: cond-mat/0206262.

7.1 Introduction

The characterization of semiconductor quantum dots by transport spectroscopy turned out to be an extremely successful approach to understand the physics of interacting electrons confined to a quasi-zero dimensional potential well [1]. Until recently the only accessible shape of the quantum dots was a tiny disc or box with a simple topology. With new fabrication techniques it is possible to create multiple connected topologies, namely small quantum rings with an outer and an *inner* boundary. These novel devices allow to study experimentally interference phenomena of electrons, like the Aharonov-Bohm effect [11] where the electronic properties of the system show a periodicity with the magnetic flux quanta threading the ring.

First quantum rings were fabricated by self-assembled growth of InAs on GaAs [105, 106], but these structures were mainly used for optical experiments. A completely different approach, the local oxidation of GaAs/AlGaAs-heterostructures with an atomic force microscope (AFM) [6], allows to write directly tuneable quantum rings into a two-dimensional electron gas [107, 108]. These rings can be studied by tunnelling experiments. For high tunnelling barriers charging effects and Coulomb blockade dominate the transport characteristics. In the Coulomb-blockade regime the number of electrons on such a ring can be controlled by an external gate voltage. Adding an electron to the ring requires the Coulomb charging energy. This leads to a nearly equally spaced sequence of Coulomb-blockade peaks as a function of the applied gate voltage. For a quantum dot with a simple connected geometry we already discussed these characteristics in chapter 5. Recently, a quantum ring containing a few hundred electrons was studied in the Coulomb-blockade regime [107]. These measurements showed the Aharanov-Bohm effect and allowed to determine the energy spectra [109] of such quantum rings. It turned out that the spectra can be well described within single-particle physics [107], because of an effective screening of the electron-electron interaction by a metallic gate.

Here we are going to discuss a quantum ring in a totally different regime. For a small number of electrons interactions dominate the spectra in absence of a front gate. In addition, for a strong coupling to the leads the spin structure of the system will strongly influence the tunnelling current. For a net spin of the system being 1/2 the ring can be mapped to the Anderson model [110] in which the ring acts as a *magnetic impurity* showing the so-called Kondo effect. This many body

phenomenon describes the formation of a spin singlet consisting of an electron on the ring and electrons in the contacts if the tunnel coupling is sufficiently high. The Kondo effect gives rise to a finite density of states at the Fermi level [111] and thus to a finite conductance around zero bias voltage even for Coulomb blockade.

In this chapter we present measurements on a quantum ring, fabricated by local oxidation with an AFM. We study our ring in a transport regime with few electrons and strong coupling to the leads. In the Coulomb-blockade regime we can tune the electron number between three and seven. For odd electron numbers a Kondo effect [14, 15] is observed and characterized with temperature dependent non-linear transport measurements. In a magnetic field we find a splitting of the Kondo resonance which, together with the even-odd behaviour, indicates a spin-1/2 Kondo effect.

The small number of electrons allows to investigate the influence of the electron-electron interaction on the level structure of our quantum ring. A theoretical calculation predicts smaller Aharonov-Bohm periods than in the multi-electron case, because the degeneracy between singlet and triplet states in a ring is lifted by the Coulomb interaction [112]. We indeed find indications for this effect in our ring at small magnetic fields. The finite Kondo conductance enables the observation of the Aharonov-Bohm effect even between two Coulomb-blockade peaks. We observe a smooth shift of these Aharonov-Bohm oscillations in the Coulomb-blockade valley with magnetic field and gate voltage.

We commence with a short introduction to Kondo physics in quantum dots.

7.2 Kondo effect

In the late eighties theoretical studies predicted a Kondo effect for a quantum dot with an unpaired electron in the topmost occupied state. The tunnelling barriers of the device should become perfectly transparent with a conductance of $2(e^2/h)$ [12, 13]. The name Kondo effect originates from the similarities between a single quantum dot and the scattering of electrons in metals induced by diluted magnetic impurities. The resistance of a metal is enhanced by an interaction of the electrons with the spins at the magnetic impurities. This effect was first explained by Kondo in 1964 in terms of correlations in the

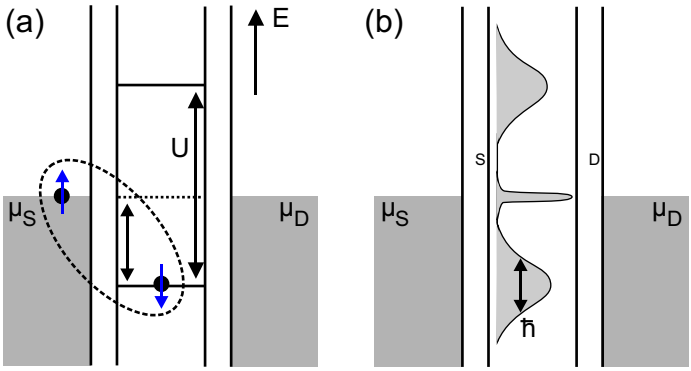

Figure 7.1: (a) Quantum dot with a singly occupied spin degenerate level. The electron on the dot couples to electrons with opposite spin in the source and drain contacts. This leads to the formation of a spin singlet indicated by the dashed ellipse. (b) The resulting density of states has a maximum pinned to the Fermi energy in the contacts.

scattering of localized spins [113]. A quantum dot with a net spin of 1/2 acts as an "impurity" as well, but the "scattering" of electrons from the contacts leads to an enhancement of the conductance.

The theoretical framework of a description of the Kondo effect in quantum dots is the Anderson impurity model [110]. An exact derivation of the model is not necessary to understand the key features of this effect and hence we only give a rather simple explanation.

In Figure 7.1(a) a quantum dot in the Coulomb-blockade regime with N electrons is shown. It is coupled to electron reservoirs by two tunnelling barriers. The topmost state of the dot contains one single electron. It is necessary that the level is two-fold degenerate, in our case due to the electron spin. In principle, we have to pay the charging energy U to add an electron but if the coupling of the electron on the dot to the leads is high enough, the interaction leads to the formation of a spin singlet state at finite temperatures. This is indicated by the dashed ellipse in Figure 7.1(a). Electrons from the leads and the dot can change places by an exchange of their spins. The spin singlet state gives rise to a finite conductance despite the charging energy and the constant N. A recent experiment indeed gives an indication for a spin-charge separation in the Kondo regime [114].

A more elaborate picture for the Kondo effect is shown in Fig-

ure 7.1(b). Here we depicted the density of states in the quantum dot. The broad peaks denote the positions of the single-particle levels in the addition spectrum. The width of the peaks is determined by the tunnel coupling to the leads given by the barrier transparencies $\hbar\Gamma = \hbar(\Gamma_S + \Gamma_D)$. Γ measures the inverse lifetime of the electron on the dot.

The striking fact is the appearance of a very narrow peak at the electrochemical potential of the contacts [111]. This finite density of states allows the transport of electrons through the structure as described in the simple picture above. In the model a new temperature scale appears named Kondo temperature T_K. In some sense $k_B T_K$ measures the binding energy of the spin singlet state. Often the Kondo temperature is defined by the following equation [115]

$$k_B T_K = \frac{1}{2}\sqrt{U\hbar\Gamma}\exp\left(\pi\frac{\varepsilon(U+\varepsilon)}{\hbar\Gamma U}\right) \tag{7.1}$$

for $\varepsilon < 0$ and $U + \varepsilon > 0$. ε is the energetic distance of the occupied level below the electrochemical potential in the contacts. The exponential dependence of T_K on the inverse of the tunnel coupling $T_K \propto \exp -1/\hbar\Gamma$ explains the necessity for the observation of this effect to tune the system into a regime with a high Γ. Additionally the Kondo temperature will be minimal in the middle of two Coulomb-blockade peaks.

Some tests can prove whether there is indeed a Kondo effect in a specific sample or not. In general, the Kondo correlations are suppressed when the outer energy scales exceed the binding energy of the spin singlet. The most direct influence is the temperature T of the electronic system in the leads. By increasing T to $T > T_K$ the finite Kondo conductance in the Coulomb-blockade valley is reduced. The most important result of the theoretical calculations is the universal behaviour of G as a function of the reduced Kondo temperature T/T_K. In Chapter 7.6.1 we discuss an empirical function that describes this characteristic. An increase of the source drain bias voltage to $eV_{SD} > k_B T_K$ leads to a similar effect. This dependence on V_{SD} gives rise to the formation of a zero bias resonance inside a Coulomb-blockade diamond.

7.3 Description of our device

Before we discuss the measurements we give a short introduction to our sample. We fabricated our quantum ring from a δ-doped GaAs/AlGaAs-heterostructure containing a two-dimensional electron gas (2DEG) 34 nm below the surface of wafer 71000. Details on the layer structure can be found in Chapter 3.1. The 2DEG has an electron density of $n_e \sim 4 \cdot 10^{15}$ m^{-2} and a mobility of $\mu_e \sim 42$ m^{2}V^{-1}s^{-1} at low temperatures. After the fabrication of Hall bars the devices are mounted into an atomic force microscope (AFM). Underneath the oxide lines, generated with local oxidation at the sample surface [6], the 2DEG is depleted. By applying high oxidation currents to the conducting AFM tip we are able to create insulating regions in the 2DEG and write complex structures directly into the electronic system with an accuracy better than 10 nm. A detailed description on our fabrication scheme can be found in Chapter 2.3.1.

An AFM image of the completed ring structure is shown in Figure 7.2(a). The two in-plane gates A and B are separated from the ring by rough oxide lines. The ring is connected to the leads by two 150 nm wide point contacts. Both point contacts are tuned by gate A whereas gate B couples only to the drain contact. The inner diameter of the ring is 190 nm and the outer diameter 450 nm. In the follow-

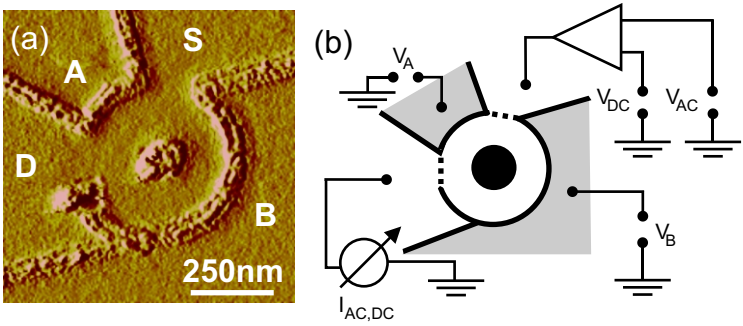

Figure 7.2: (a) AFM image of the ring-structure. IPGA, IPGB denote the in-plane gates, S and D the source and drain contacts. (b) Schematic picture of our measurement setup. The tunnelling barriers (indicated by the dashed lines) are induced by negative gate voltages.

ing experiments, gate A is kept at a constant voltage V_A, and V_B is used to control the number of electrons on the ring. A schematic picture of our measurement setup is depicted in Figure 7.2(b), where the gates are indicated by the grey areas. All transport measurements were performed in a ^{3}He/^{4}He-dilution refrigerator with an AC-excitation voltage of 5 μV, at 89 Hz, added to a variable DC-voltage V_{SD}. The base temperature during the experiments was $T_b = 30$ mK. From the temperature dependence of the Coulomb-blockade peaks we deduce an effective temperature of less than 50 mK for the electronic system.

In the open transport regime with $V_A, V_B \geq 0$ mV, we obtain an Aharonov-Bohm period $\Delta B \sim 60$ mT for electrons that are transmitted ballistically through the ring. The observed periodicity corresponds to a diameter for the electronic orbit of 300 nm, which fits perfectly to the geometric values. An extensive study of the open transport regime of this sample was already discussed in Chapter 6.

For the measurements in the Coulomb-blockade regime we have to separate the ring from the contacts by tunnelling barriers (indicated by the dashed lines in Figure 7.2(b)). These are induced by applying $V_A, V_B < -50$ mV to the in-plane gates. In the Coulomb-blockade regime, we extract a charging energy for our ring of $U \sim 1.5$ meV by analysing the Coulomb-blockade diamonds. The observation of excited states in such measurements allows to estimate the single-particle level spacing to $\delta E \sim 150$ μeV, see Appendix A.

7.4 Tuning of the tunnel coupling

As already mentioned we can use the in-plane gates to induce tunnelling barriers at the point contacts. These separate the ring from the source and drain contact. In Figure 7.3(a) a grey-scale plot of the linear conductance G as a function of V_A and V_B is shown. For the measurement V_A was stepped from -250 mV to -50 mV with $\Delta V_A = 5$ mV and V_B varied continuously between -280 mV$< V_B <$-100 mV. When the electrochemical potential on the ring matches with the electrochemical potentials in the leads the number of electrons N on the ring is increased by one. On every occurrence this leads to a peak in G indicated by a black line in the plot. The peaks have a gradient because of the finite capacitance of the gates. In this regime the ring exhibits dot-like characteristics as observed for the single-electron transistor in Chapter 5.

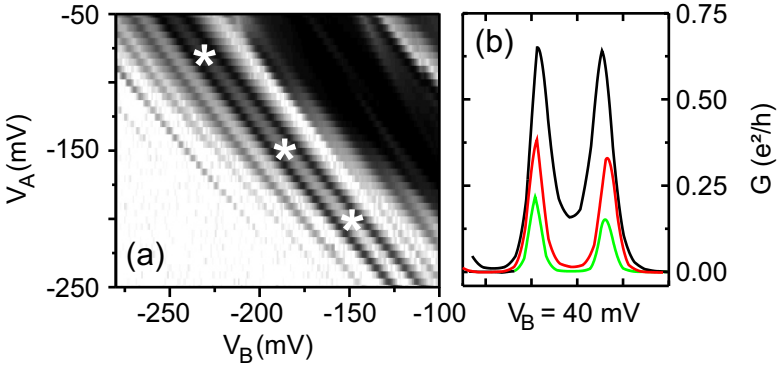

Figure 7.3: (a) Grey-scale plot of the linear ring conductance G as a function of both in-plane gate voltages V_A, V_B. Each time an electron is added to the quantum ring a peak shown in black is observed. (b) The Coulomb-blockade valleys (in (a) marked with an asterisk) for $V_A = -200$ mV (lower curve), $V_A = -150$ mV and $V_A = -80$ mV (upper curve) show an increasing valley conductance with V_A.

Apart from the electrochemical potential the tunnel coupling increases with V_A. The data in Figure 7.3(b) depicts two Coulomb-blockade peaks with an equal number of electrons at $V_A = -200, -150, -80$ mV from top to bottom. The positions of the shown Coulomb-blockade valleys are marked in Figure 7.3(a) by the white asterisks. Beside the raise of the peak conductance by a factor of five to $0.8(e^2/h)$ the most striking result is the increase of the valley conductance in between the peaks whereas it barely changes at the left and right hand side. From the constant interaction model described in Chapter 5 we would expect that the transport of electrons is suppressed in a Coulomb-blockade valley because of the charging energy U. In the regime with the higher tunnel coupling this simple picture is no longer valid and we observe a finite valley conductance due to a Kondo-effect as described in Chapter 7.2. In Chapter 7.6.1 we will investigate the Kondo temperature and even-odd effects.

7.5 Counting electrons on a quantum ring

First we focus on the addition spectrum of our ring in a perpendicular magnetic field at high tunnel coupling with $V_A = -80$ mV. The addition spectrum is shown in Figure 7.4 for magnetic fields up to 6 T. The linear conductance G ($V_{SD} = 0$) is plotted in a grey-scale as function of V_B and the perpendicular magnetic field B at $V_A = -80$ mV. Each Coulomb-blockade peak appears as a black line which runs more or less parallel to the B-axis. Signatures of non-vanishing conductance between the Coulomb-blockade peaks can be seen and are attributed to the Kondo effect. One example is marked by the arrow in Figure 7.4 at $V_B = -230$ mV. The Kondo effect shows a pattern of abrupt changes between high (grey) and low (white) conductance regions for $B < 2$ T. This pattern looks similar to the pattern obtained in a quantum dot designed as a disc [116], presumably due to the similar importance of the outer edge for transport in high magnetic fields. Whereas for disc-like

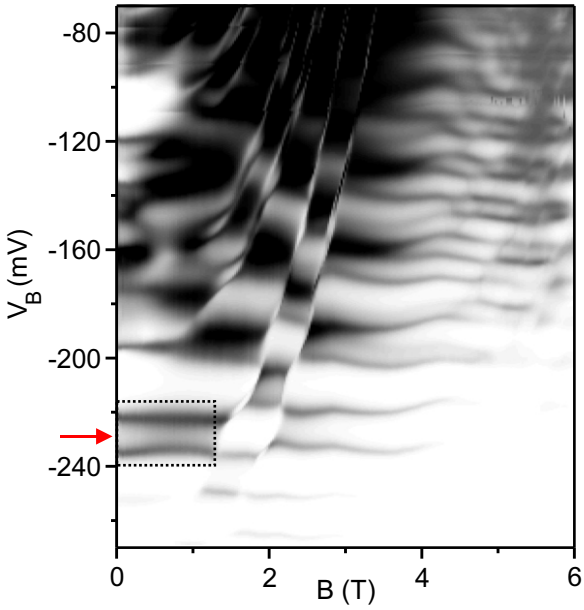

Figure 7.4: Linear conductance G of the ring as a function of V_B and the magnetic field B at $V_A = -80$ mV. The grey-scale plot shows the addition spectrum of our quantum ring.

quantum dots Hund's rule was found [117], we observe an odd-even behaviour of the Kondo effect for the gate voltage range $V_B < -200$ mV.

The alternating pattern of the valley conductance with magnetic field is explained by a redistribution of the electrons between different Landau levels (LL). For example, inside the Kondo valley marked by the arrow in Figure 7.4 we obtain high conductance because of an unpaired spin in the transport state at small magnetic fields. At $B \sim 1.5$ T an electron from the upper LL is transferred to the lower LL which is indicated by the sharp boundary in the spectrum in Figure 7.5. The Kondo effect is suppressed because the transport level in lowest and outermost LL $n = 0$ contains two electrons with opposite spins (N =odd, spin-0 in $n = 0$). At $B \sim 2.0$ T a second electron is transferred to LL $n = 0$ and there is again an unpaired spin in the transport state in LL $n = 0$ and the Kondo effect is restored. For higher magnetic fields similar changes are not observed anymore and thus we conclude that no further electrons are redistributed from LL $n = 1$ to $n = 0$. Therefore, we assume that all electrons on our quantum ring are in the lowest Landau level and the filling factor ν equals two at $B \sim 2.0$ T.

With a further increase of the magnetic field we observe small variations of the position and height of the Coulomb-blockade peaks. These weaker features are highlighted in Figure 7.5 by the dashed lines. The small wiggles in the peak position are only observed up to magnetic fields of $B \sim 5.5$ T for the Kondo valley marked in Figure 7.4. The features are identified with spin flips of the electrons on the ring.

The spin of the electron is flipped from the up to the down state in the lowest LL because of the increasing magnetic field [118, 119, 116]. N is determined by assuming that the electrons in the lowest LL are totally spin-polarized for $B > 5.5$ T. This corresponds to a filling factor $\nu = 1$ of the quantum ring. Between $\nu = 2$ ($B = 2$ T) and $\nu = 1$ ($B \sim 5.5$ T) we observe two spin flips for the Kondo valley marked in Figure 7.5. Therefore, we conclude that there are four electrons on the quantum ring. The same considerations apply for the consecutive Coulomb-blockade valleys. We extract for these valleys $N = 5$ and $N = 6$, respectively. This is underlined by the alternating occurrence of the Kondo effect in the spectrum. As mentioned above, we observe an even-odd behaviour at $B = 0$. In the next section, we investigate this characteristic with non-linear conductance measurements.

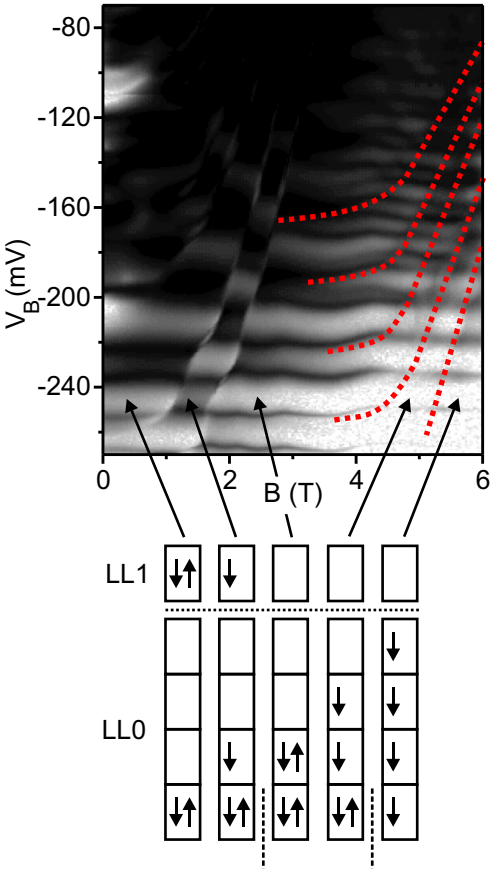

Figure 7.5: Logarithmic plot of the addition spectrum shown in Figure 7.4. The dashed lines mark the observed spin flips in the ring. The boxes and arrows below denote the situation for $N = 4$ electrons on the dot at the different magnetic fields. At $B > 5.5$ T the dot has the filling factor $\nu = 1$ and is fully spin polarized. The sharp boundary between $\nu > 2$ and $\nu < 2$ at $B \sim 2.0$ T marks the depletion of Landau level 1 (LL 1).

7.6 Non-linear transport measurements in the Kondo regime

For a further analysis of the Kondo effect non-linear transport measurements are shown in Figure 7.6 at $B = 0$. Figure 7.6(a) depicts the differential conductance dI_{SD}/dV_{SD} at a temperature of $T_b = 30$ mK as a function of V_B and V_{SD} ($V_A = -80$ mV, $B = 0$) in a grey-scale. We show five consecutive Coulomb-blockade diamonds. The horizontal line in the center diamond marks the valley with the arrow in Figure 7.4. Here a sharp zero-bias peak (Figure 7.6(c)) can be observed whereas the valleys above and below show only low conductance due to

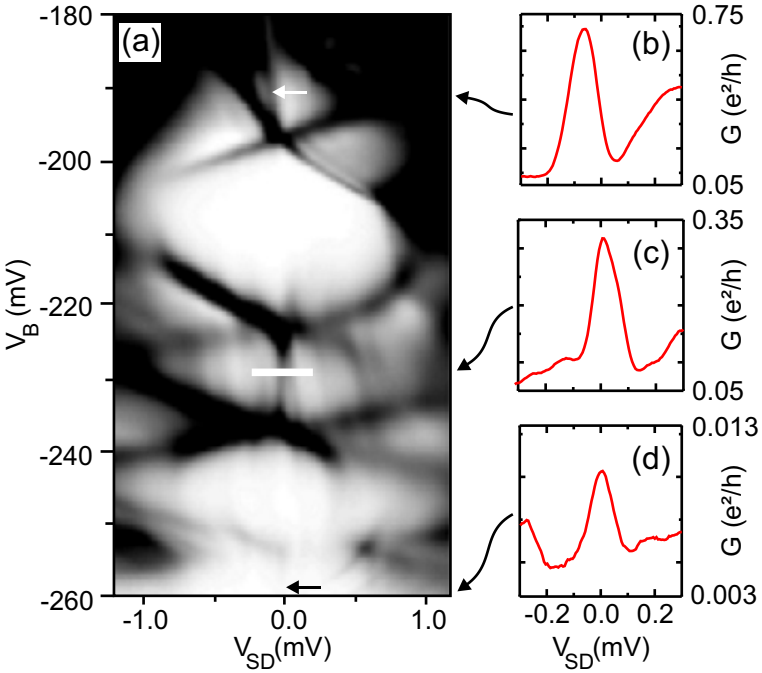

Figure 7.6: Grey-scale plot of the differential conductance dI_{SD}/dV_{SD} as a function of the source-drain voltage V_{SD} and in-plane gate voltage V_B at $V_A = -80$ mV. The Kondo effect is only observed in the diamonds with odd electron numbers: $N = 3$ marked with the black arrow, $N = 5$ marked with the horizontal line, and $N = 7$ marked with the white arrow.

the Coulomb-blockade charging energy. We observe also Kondo peaks in the lowest and top-most diamonds. This is illustrated by the traces shown in Figure 7.6(b)+(d), respectively. Please note the different scaling of the conductance axis. We conclude that there is an even-odd asymmetry of the Kondo effect. This is an indication that the characteristic is due to a spin-1/2 Kondo effect.

In Figure 7.6(b) the resonance is shifted to finite bias voltages. This behaviour is expected from the asymmetry of our device since with increasing V_B the upper tunnelling barrier is lowered. This behaviour was reported by Simmel *et al.* [17] for a quantum dot with very asymmetric barriers.

7.6.1 Temperature dependent measurements

Figure 7.7(a) depicts measurements at different temperatures at the gate voltage marked in Figure 7.6 by the horizontal dashed line. The zero-bias peak observed at $T_b = 30$ mK vanishes almost completely when the temperature is increased to $T \sim 500$ mK as predicted for a Kondo resonance [111]. From these measurements we estimate the Kondo temperature T_K for our system by extrapolation of the peak width ΔV_{SD} (full width at half maximum) to $T = 0$ as depicted in Figure 7.7(b) [111, 120], which results in $T_K \approx 0.5 e\Delta V_{SD}(T = 0)/k_B \sim 600$ mK. A fit of the peak conductance at zero bias $G_0(T)$ with the empirical formula of Ref. [121, 120],

$$G(T) = G_0 / \left(1 + (2^{1/s} - 1)(T/T_K)^2\right)^s \tag{7.2}$$

provides another estimate for T_K, yielding $T_K \sim 600$ mK for $s = 0.2$. s is a fit parameter that is related to the spin state of the impurity that induces the Kondo effect. For a spin-1/2 system $s \sim 0.25$ was observed in an experiment by Goldhaber-Gordon *et al.* [121]. The peak conductance scaled with the extracted T_K and $G_0 \sim 0.33 e^2/h$ is shown together with the fit in Figure 7.7(c).

7.6.2 Splitting with magnetic field

A zero-bias peak of a spin-1/2 Kondo effect at $B = 0$ is expected to split in a magnetic field with $\Delta E_z = g_{GaAs}\mu_B B$ (g-factor of GaAs 0.44, μ_B Bohr's magneton) due to the Zeeman effect [111]. The resulting density of states is depicted in Figure 7.8(a). As a consequence, the

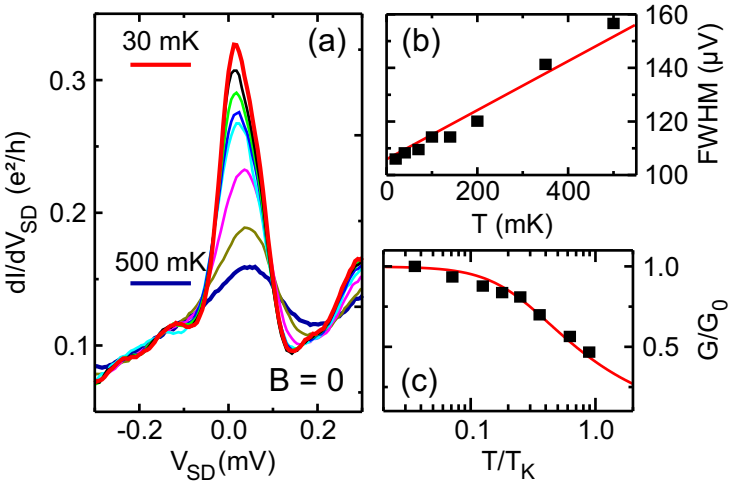

Figure 7.7: (a) Differential conductance as a function of the source drain voltage V_{SD} for $N = 5$ electrons at $V_A = -80$ mV for temperatures between $T = 30$ mK (upper curve) and $T = 500$ mK (lowest curve). The data is marked in Figure 7.6 by the horizontal line. (b) Full width at half maximum (FWHM) of the Kondo peak in (a) as a function of the temperature T. By extrapolating the data to $T = 0$ the Kondo temperature is estimated to $T_K \sim 600$ mK. (c) Peak conductance G/G_0 as a function of T/T_K. The data was scaled with $G_0 = 0.33(e^2/h)$ and $T_K \sim 600$ mK. The line is a fit with the empirical function 7.2.

peak induced by the Kondo effect is split with ΔE_z. For the observation of the spin singlet between both leads a non-zero bias voltage has to be applied to compensate for the splitting.

We investigate the splitting of the Kondo resonance in the diamond marked by the horizontal line in Figure 7.6 at high magnetic fields. In Figure 7.8(b) the corresponding diamond is shown at $B = 3$ T. At non-zero bias voltages two peaks appear, which are symmetrically located around $V_{SD} = 0$. A cut through the data along the line is depicted in Figure 7.8(c). The different amplitudes of the two peaks have to be related to the slight asymmetry in the coupling of the ring to the contacts.

The peak positions in V_{SD} of such split peaks extracted from several of these measurements for 2 T$< B <$ 4 T are plotted in Figure 7.8(d).

The lines in Figure 7.8(d) indicate the expected peak positions (for a g-factor of 0.44). We observe a nice agreement between the measured and expected spin splitting for $B > 2$ T which is another evidence for a spin-1/2 Kondo effect. Between 1.5 T and 2.1 T the Kondo effect is absent due to the paired spin configuration. For fields lower than 1.5 T the peak splitting is not resolved, presumably due to the broadening of the Kondo peak on the order of $k_B T_K \sim 50$ μeV. In contrast to the expected splitting a maximum of the Kondo conductance is even observed for a magnetic field of around 1 Tesla which is related to a decreased backscattering in the magnetic field.

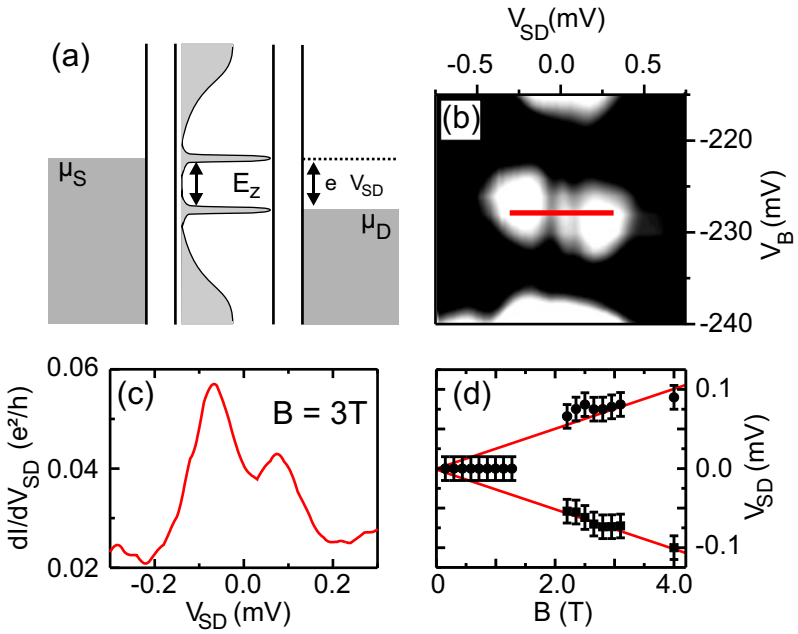

Figure 7.8: (a) Density of states at finite magnetic field. The Zeeman-splitting E_z of the level in the dot leads to a splitting of the Kondo resonance. (b) Coulomb-blockade diamond at $B = 3$ T showing the split Kondo resonance. (c) Non-linear conductance along the dashed line in (b). (d) Splitting of the Kondo resonance as a function of magnetic field. The lines denote the expected spin splitting. For the peak positions at $B < 1.5$ T see text.

7.7 Valley conductance at small magnetic fields

In Figure 7.9(a) we show again the $N = 5$ Kondo valley for $B < 1.5$ T. This part of the addition spectrum is marked by the dotted box in Figure 7.4. As usual the Coulomb-blockade peaks are depicted as black lines at $V_B \sim -223$ mV and $V_B \sim -237$ mV. In Figure 7.9(b) the nonlinear differential conductance dI_{SD}/dV_{SD} is plotted as function of B and V_{SD} along the dashed line at $V_B = -229$ mV in 7.9(a).

The zero-bias peak (black region around $V_{SD} = 0$ mV) gets more pronounced with increasing B. In Figure 7.9(c) we depict the corresponding peak conductance G_0 at $V_{SD} = 0$ along the white dashed line in (b). G_0 doubles from 0.3 to $0.6(e^2/h)$ at $B \sim 800$ mT. This is completely unexpected. With increasing perpendicular B the effective tunnel coupling is reduced which should lead to a suppression of the Kondo effect. Indeed we observe this behaviour but only for $B > 800$ mT. An increase of the Kondo temperature is probably excluded to cause the doubling of G_0 because the peak width, and thus T_K, remains constant as displayed in Figure 7.9(d). We plotted the

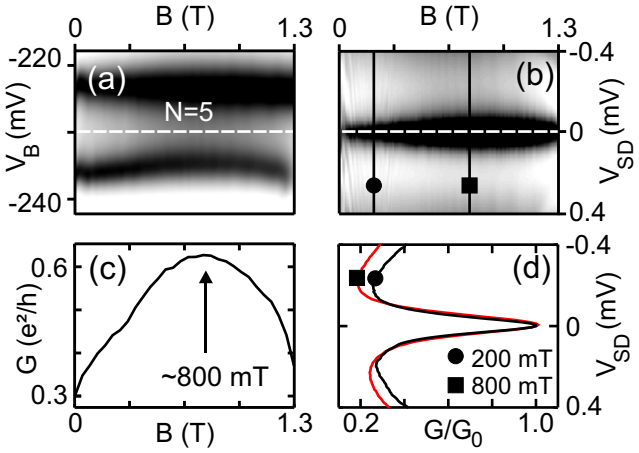

Figure 7.9: (a) Greyscale plot of the linear conductance $G(V_B, B)$ – (b) greyscale plot of the nonlinear conductance $g(V_{SD}, B)$ along the white dashed line in (a) – (c) G_0 as a function of B at $V_B = -229$ mV and $V_{SD} = 0$ – (d) scaled zero bias peaks at $B = 200$ mT marked in (b) by • and ■ at $B = 800$ mT.

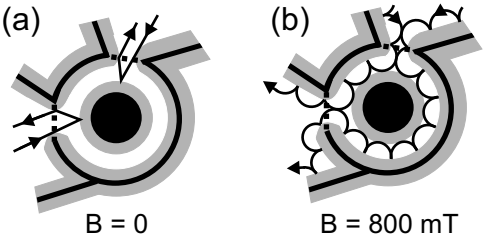

Figure 7.10: (a) Schematic picture of our ring in the Kondo valley for $B = 0$. (b) Classical electron trajectories at finite B. Please note the reduced backscattering at the ring center compared to (a).

zero-bias peak for $B = 200$ mT and $B = 800$ mT normalized to the respective G_0, both peaks have the same width and thus a similar T_K.

For an ideally symmetric quantum dot the tunnelling barriers should become transparent in the Kondo effect with a conductance of $2(e^2/h)$. This behaviour was reported for real quantum dots only recently [122, 120]. The asymmetry of our device prevents the observation of this effect in this gate voltage regime. But transport through the device in the Kondo regime might be ballistic.

In a classical picture an incident electron is scattered at the inner ring boundary. Depending on the angle of incidence the electron is reflected back into the contact, Figure 7.10(a). This backscattering leads to a reduction of G_0 at zero magnetic field. It is known that the scattering of ballistic electrons at boundaries is specular, see e.g. [123]. We estimate the cyclotron length l_c for the ring at the maximum of G observed at $B \sim 800$ mT. With the electron density n_e in the unstructured 2DEG $n_e \sim 4 \cdot 10^{15}/\mathrm{m}^2$ this yields $l_c = hk_F/2\pi eB \sim 100$ nm at $B = 800$ mT, with h Planck's constant and $k_F = \sqrt{2\pi n_e}$ is the wave number. Since the reduced arm width lies in the same range because of the finite depletion width around the oxide lines, G_0 increases, because the backscattering at the inner ring boundary is suppressed. In a classical picture this is shown in Figure 7.10(b).

This reduced scattering is only one of the possible explanations for the increasing valley conductance. There might be also a change in the level structure of the ring in this magnetic field range. At least the lower Coulomb-blockade peak in Figure 7.9(a) is moving upwards in V_B. Such a gradually change is could be due to a split state of the ring at $B = 0$ induced by spin-orbit interaction.

7.8 Aharonov-Bohm measurements in the Kondo regime

With our quantum ring in the Kondo regime we are able to study the influence of the magnetic field on the level structure as described in Chapter 2. But the Coulomb-blockade peaks are broadened due to the strong coupling in the Kondo regime. This obscures the observation of small shifts in the peak positions as induced by the magnetic field. To avoid this, the Kondo valley marked in Figure 7.4 is shown again in Figure 7.11(a) at a slightly lower tunnel coupling with $V_A = -150$ mV. This reduces the conductance in the Kondo regime to below $0.1(e^2/h)$. Due to the finite capacitance between the ring and gate A, the valley is shifted to $V_B \sim -185$ mV. Figure 7.11(b) shows the normalized conductance G/G_0 as a function of B for the gate voltages marked by the symbols in Figure 7.11(a). The vertical dashed lines denote the expected period of $\Delta B \sim 60$ mT of the Aharonov-Bohm oscillations extracted from the measurements in the open regime, see Chapter 6. It is immediately evident that we obtain a much shorter period. This result is in contrast to the results of Fuhrer *et al.* [107], who obtained the normal Aharonov-Bohm period for their ring with many electrons and a front gate screening the electron-electron interaction.

The fast oscillations are also reflected by the movement of the Coulomb-blockade peaks in the grey-scale plot of Figure 7.11(c) (the peak positions are marked by white dots). Each kink in the trace of the Coulomb-blockade peaks indicates a change of the ground state in the quantum ring.

We are investigating the $N = 5$ valley and observe a surprisingly short period of around $\Delta B \sim 13$ mT. This corresponds to a four to five times shorter period than in the open regime. This is unusual because this would indicate that our ring has a five times *larger* area.

Interacting electrons in quantum rings

The model in Chapter 2 is only a simple approach to the description of non-interacting electrons in a single-particle picture. A period halving for the persistent current in a ring [124] because of the electron spin was found even for *non-interacting* electrons [125]. But this effect does not explain our higher frequencies.

We have already shown that there are less than ten electrons on our ring in the Coulomb-blockade regime. The single-particle considera-

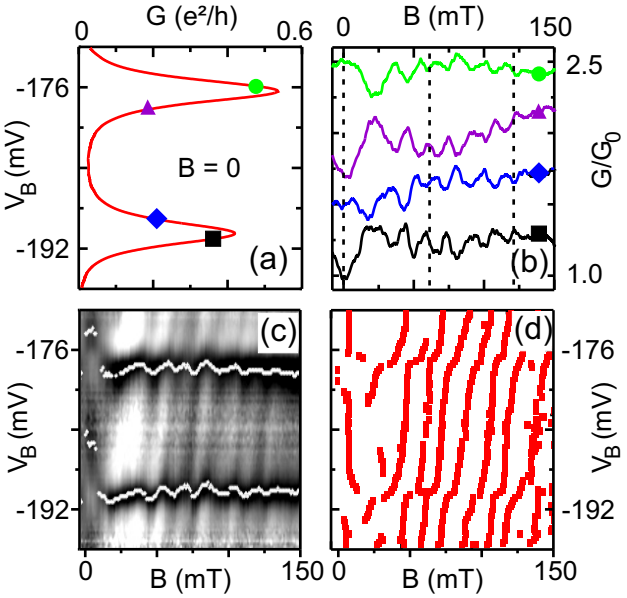

Figure 7.11: (a) The $N = 5$-Kondo valley at a lower tunnel coupling at $V_A = -150$ mV and $B = 0$. ■, ♦, •, ▲ mark the gate voltages for the Aharonov-Bohm measurements shown in (b). (b) Normalized conductance G/G_0 of the quantum ring as a function of magnetic field B. The curves are offset for clarity. (c) $G/G_0(B, V_B)$ as grey-scale plot. (d) Position of the Aharonov-Bohm maxima extracted from (c).

tions will no longer be valid and interaction effects have to be taken into account. A theoretical calculation of the energy spectra of few-electron rings with exact diagonalization by Niemelä et al. [112] indicate that the Aharonov-Bohm period ΔB of the peak oscillation depends on the number of interacting electrons on the ring. For N electrons ΔB should be shortened by a factor of $1/N$. Their results are explained by the Coulomb interaction between the electrons. A result of calculations for two and three electrons on a ring is depicted in Figure 7.12. All energies are measured in units of $E_0 = 2h^2/m^*\pi^2 d_e^2$, with d_e the diameter of the ring.

If no interaction is present the ground state of the ring is always a spin-singlet and the first excited state is spin degenerated. For two

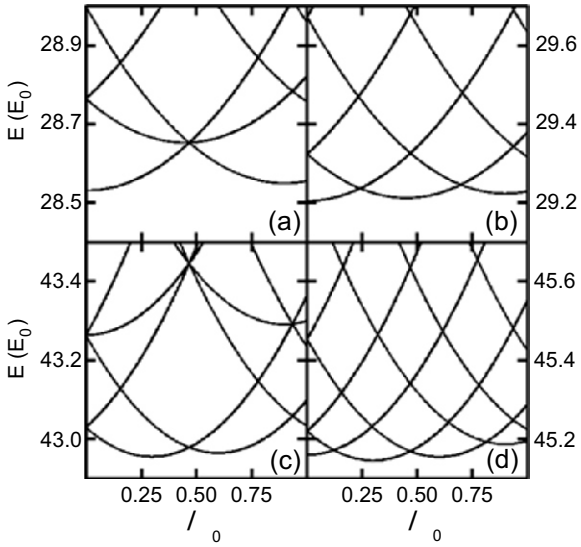

Figure 7.12: The few low-lying energy states for a ring containing (a) two non-interacting electrons, (b) two interacting electrons, (c) three non-interacting electrons, and (d) three interacting electrons as a function of the applied magnetic flux ϕ. This picture was taken from Ref. [112].

non-interacting electrons the ground state changes like $l = 0, 2, 4, ..$ (Figure 7.12(a)) and thus we get a similar behaviour of the lowest state as for the simple picture shown in Figure 2.2(b). With the Coulomb interaction the degeneracy of the singlet-triplet state is lifted and the triplet state comes down in energy with respect to the singlet due to the exchange term in the Coulomb matrix element [112]. As a consequence already for two interacting electrons a halving of the Aharonov-Bohm period for the peak oscillation is expected because l changes with $0, 1, 2, 3, ..$ which leads to $\Delta B/2$ as depicted in Figure 7.12(b).

These considerations are valid for three electrons as well. Without interactions the ground state changes with $l = 1, 2, 4, 5, ..$, see Figure 7.12(c). Here the oscillation period is already halved. The Coulomb interaction leads to a sequence $l = 0, 1, 2, 3, ..$ and thus the ground state of the ring in the magnetic field changes more often than for the non-interacting case as depicted in Figure 7.12(d).

As as consequence these results lead to a shortened Aharonov-Bohm

period for the N-electron quantum ring of $\Delta B/N$ [112]. With these results in mind our shorter period has to be linked to the small number of electrons on our ring. There might be some reasons for the deviations from the reduced period. We expect a decrease of d_e with an increasing negative gate voltage and thus ΔB will be higher than 60 mT which would fit even better our observations. The deviations from perfect periodicity especially at small magnetic fields might be explained by the influence of some residual disorder. There remain some open questions because we were not able to obtain data in the next Coulomb-blockade valley due to a spin blockade. At even higher tunnel couplings there starts already the chaotic regime without regular Coulomb blockade, see Figure 7.4. However, the good agreement of the data with the theoretical predictions gives a strong indication that our interpretation of the data is correct.

7.8.1 Aharonov-Bohm effect in the Kondo valley

As mentioned above we investigate now the evolution of the Aharonov-Bohm effect in the Kondo-valley. As depicted in the grey-scale plot in Figure 7.11(c) there are oscillations with the correct frequency. But the origin of the observed modulation of the Kondo conductance in our quantum ring is not clear at the moment. One possible explanation is the dependence of T_K on the ground state from a singlet to a triplet. Sasaki *et al.* [126] reported measurements on a vertical quantum dot where a Kondo effect was achieved by tuning the degeneracy of a singlet and a triplet state with an outer magnetic field. Excited states interacting with the degenerate levels in the quantum ring could as well play a role and modify the transport in the Kondo regime.

Of special interest is the evolution of the Aharonov-Bohm effect between the Coulomb-blockade peaks. The finite conductance in this regime allows following the positions of the maxima as function of the gate voltage V_B and magnetic field B. For illustration of this result the position of each maximum in B as observed in Figure 7.11(c) is marked by a dot in Figure 7.11(d). At the first Coulomb-blockade peak (between $V_B = -191$ mV and $V_B = -189$ mV) we observe a phase jump of π, indicated by the small kink at $V_B = -190$ mV for all magnetic fields. This is verified in Figure 7.11(b) – the oscillation at $B = 0$ changes from a minimum to a maximum. The same behaviour is observed at the next Coulomb-blockade resonance in Figure 7.11(b). At this peak the signal at $B = 0$ changes from a minimum (trace at

$V_B = -178$ mV) to a maximum at $V_B = -176$ mV. Both peaks show a similar phase change by π.

This in-phase characteristic of consecutive Coulomb-blockade peaks was also observed in a study on a dot in one arm of an Aharonov-Bohm interferometer [127]. The origin of this effect in the Coulomb blockade regime of quantum dots is still not clarified and extensively studied in the literauture.

We now take a closer look on the evolution of the Aharonov-Bohm oscillations as a function of gate voltage and magnetic field. In the Coulomb valley the maxima show a smooth shift (Fig. 7.11(d)). These linear shifts appear in our two-terminal measurement only at finite magnetic field when the ring is threaded by at least half a flux quantum. Linear shifts of *normal* Aharonov-Bohm oscillations were recently reported by Ji *et al.* for a quantum dot in the Kondo regime embedded in an Aharonov-Bohm interferometer [128]. Their four-terminal measurement is interpreted in terms of smooth phase shifts by π across a Kondo resonance. In our experiment we investigate the Kondo resonance of a quantum dot which itself serves as the interferometer.

The exact mechanism for the observed linear shift of the Aharonov-Bohm maxima is still to be clarified, but it might be connected to the fact that the level structure of our small ring interferometer is influenced by the gate voltage. For a detailed understanding further theoretical work is necessary.

7.9 Conclusion

In conclusion, a small tuneable quantum ring with less than ten electrons is studied in the Coulomb-blockade and in the Kondo regime. The Kondo effect allows the study of the spin structure of the measured spectrum. Zeeman splitting of the zero-bias anomaly indicates a spin-1/2 Kondo effect. An analysis of the phase evolution of the Aharonov-Bohm effect in the Kondo regime yielded phase jumps by π at the Coulomb-blockade resonances and a smooth shift of the Aharonov-Bohm maxima between the Coulomb-blockade peaks.

8 Summary

In this thesis we used the atomic force microscope (AFM) for the creation of complex mesoscopic devices with various geometries. The basis for our experiments were GaAs/AlGaAs-heterostructures with two-dimensional electron gases (2DEG) 57 nm, 40 nm, and 34 nm below the surface. We studied in detail controlled mechanical nanomachining and local oxidation.

We fabricated ballistic quantum point contacts by engraving a constriction into a GaAs/AlGaAs-heterostructure with the tip of an AFM. The devices were nanomachined using both a silicon tip and a diamond tip to study the influence of the tip material. It turned out that a diamond tip is almost perfect not only for a fast and simple processing but also in forming proper potential profiles to observe ballistic electron transport. The appearance of the 0.7 ($2e^2/h$) conductance anomaly confirms the high quality of diamond-engraved devices. We deduced the depletion lengths induced by the different tips, yielding ~ 200 nm for diamond-engraved samples, which is roughly two times smaller than typical depletion lengths in devices patterned with a Silicon tip.

A detailed study of the local oxidation with an AFM proved the importance of the oxidation current for the controlled fabrication of tunnelling barriers in 2DEGs. We found a linear dependence of the barrier height on the oxidation current which is related to the depth of the oxide lines. With these tunnelling barriers we fabricated a single-electron transistor containing several hundred electrons well described by the constant interaction model.

Further we demonstrated that the AFM-based nanolithography provides a relatively easy and controlled approach to create parallel quantum dots. The double dot was stepwise fabricated with a combination of controlled nanomachining and local oxidation. The dots were defined by splitting a quasi-one-dimensional resonant tunnelling diode in two separate zero-dimensional regions. Analysing of the transport measurements of the two quantum dots allowed the identification of the specific Coulomb-blockade oscillations of each dot. We showed that the current

could be directed through both quantum dots separately by applying high negative gate voltages to the respective in-plane gates. These experiments proved that the combination of controlled nanomachining and local oxidation with an atomic force microscope is a straightforward approach to fabricate robust mesoscopic devices.

In the remaining part of the thesis we investigated the transport characteristic of a quantum ring defined by local oxidation in great detail. We discussed the Aharonov-Bohm effect in this asymmetric quantum ring with a diameter of below 450 nm. The analysis of the data with Fourier transformation indicated only one interfering subband in the ring. This led to a modulation of the conductance of more than 50%. The electron orbit extracted from the periodicity of the Aharonov-Bohm effects fits perfectly to the ring geometry. The attached in-plane gates allow to tune the phase of the Aharonov-Bohm effect at zero magnetic field and we observed the typical sharp phase jumps by π that are related to the asymmetry of our device. Finally, we showed that the line-shape of the resonances in the quantum ring is controlled by an outer gate voltage and the magnetic field. This fact was explained by interference between a resonant bound state and directly submitted electrons. This led to a Fano like characteristic.

The attached in-plane gates of the quantum ring allowed to study the same device in the Coulomb-blockade regime. With the observation of spin flips in the addition spectrum in a perpendicular magnetic field we determined the number of electrons to below ten in this voltage range. The observation of a Kondo effect enabled to study the spin structure of the measured quantum ring. The Kondo resonances vanished and broadened with increasing temperature. The peak conductance follows the universal curve and was used to estimate the Kondo temperature of the device. Non-linear transport measurements showed an even-odd behaviour of the Kondo effect. This result together with a Zeeman splitting in a perpendicular magnetic field led to the conclusion that the Kondo effect was induced by a single spin on the ring. The magnetic field dependence of the conductance in the Kondo valley could be interpreted as ballistic transport of as few as five electrons.

At low magnetic fields we observed oscillations in the ground state of the device with a periodicity related to the number of electrons on the ring. This effect caused by strong electron-electron interactions was attributed to the small number of electrons. We found Aharonov-Bohm oscillations of the conductance in the Kondo regime as well. The finite conductance due to the Kondo effect was used for an analysis of the

phase evolution of this Aharonov-Bohm effect in the Coulomb-blockade valley. The measurement yielded phase jumps by π at the Coulomb-blockade resonances and a smooth shift of the Aharonov-Bohm maxima in between.

The observation of the Kondo and Aharonov-Bohm effect shows the wide range of possible research topics for these kind of devices. Due to their smallness together with the few electrons and the exact control of the sample parameters these devices are ideal systems to compare the experimental results with theoretical predictions. With the AFM-based lithography it should be possible to design novel geometries for mesoscopic systems, which may show an unexpected variety of new effects in transport experiments.

Deutsche Zusammenfassung

In dieser Arbeit wurde ein Rasterkraftmikroskop (englisch: Atomic Force Microscope AFM) zur direkten Herstellung mesoskopischer Bauteile in zwei-dimensionalen Elektronengasen (2DEG) in GaAs/AlGaAs-Halbleiterheterostrukturen verwendet. Es kamen zwei Strukturierungsverfahren mit dem AFM zum Einsatz: die mechanische Nanostrukturierung und die lokale Oxidation. Beide Techniken erlauben die kontrollierte Erzeugung von isolierenden Bereichen in einem 2DEG durch Manipulation an der Probenoberfläche. Der große Vorteil beider Techniken liegt in der räumlichen Trennung von strukturierten Bereichen an der Oberfläche und dem elektronischen System. Diese Besonderheit verhindert die Erzeugung von Defekten im 2DEG.

Bei der mechanischen Nanostrukturierung wird die AFM-Spitze wie ein Pflug verwendet, der die Oberfläche der Heterostrukturen in kontrollierter Weise einritzt. Die Untersuchungen konzentrierten sich dabei auf den Vergleich der Strukturierungseigenschaften von herkömmlichen, aus Silizium bestehenden Spitzen und neuartigen Diamantspitzen. Im Laufe der Experimente wurde gezeigt, daß die Diamantspitzen nicht nur sehr viel haltbarer sind, sondern auch den Herstellungsprozeß um ein Vielfaches beschleunigen. Zum Vergleich der elektronischen Eigenschaften der mit verschiedenen Spitzen hergestellten isolierenden Linien, wurden ballistische Quantenpunktkontakte erzeugt und bei tiefen Temperaturen mit Transportspektroskopie vermessen. Während die mit einer Si-Spitze hergestellten Proben nur eine schwach ausgeprägte Quantisierung des Leitwerts zeigen, ergaben die Beobachtungen an mit Diamantspitzen erzeugten Proben ballistischen Transport über einen weiten Kennlinienbereich. Damit konnte gereigt werden, dass mit einer Diamantspitze geschriebene Linien ein adiabatisches Einschlußpotential ohne nennenswerte Defekte definieren. Zudem halbiert sich die minimale Linienbreite genauso wie die Verarmungslänge im Vergleich zu mit Si-Spitzen hergestellten Strukturen.

Außerdem wurde die lokale Oxidation von Heterostrukturen untersucht. Hierfür wurde eine negative Spannung zwischen einer leitfähigen

AFM-Spitze und der Heterostruktur angelegt. Durch den auf fast jeder Probe existierenden Wasserfilm entstand so eine Elektrolytzelle mit einer Ausdehnung von wenigen Nanometern. Auch mit dieser lokalen Oxidation wurden verschiedene 2DEGs isloiert analog zur mechanischen Strukturierung. Diese Technik bot zudem die Möglichkeit, durch eine Regelung des Oxidationsstroms die Verarmung des 2DEGs exakt einzustellen. Dies wurde für die Herstellung eines Einzelelektrontransistors (SET) verwendet. Die Charakterisierung mit Transportmessungen bei Temperaturen von 350 mK zeigte, dass das Bauteil mit einem einfachen Modell für Einzelladungseffekte beschrieben werden konnte. Von besonderem Interesse war insbesondere die Kombination von Nanostrukturierung und lokaler Oxidation für die Herstellung von zwei parallelen SETs, die ebenfalls demonstriert wurde.

Ein weiterer großer Vorteil der AFM-Strukturierung mit der lokalen Oxidation ist die Möglichkeit, Proben mit mehrfach zusammenhängender Topologie zu erzeugen. Als Beispiel wurde ein kleiner Quantenring mit einem Durchmesser von nur 450 nm diskutiert. Die Transportmessungen zeigten bei 30 mK und senkrecht zum Stromfluß angelegtem Magnetfeldern Aharonov-Bohm-Oszillationen mit einer Leitwertsfluktuation von mehr als 50%. Dieser quantenmechanische Intereferenzeffekt von Elektronen erlaubte die genaue Bestimmung der Länge der Elektronenbahn im Quantenring. Es ergab sich eine hervorragende Übereinstimmung der gemessenen Oszillationsfrequenz mit der erwarteten, die aus den AFM-Bildern der Struktur berechnet wurde. Die an jedem Ringarm angebrachten lateralen Elektroden erlaubten zudem, die Phase der elektronischen Wellenfunktion im Ring einzustellen. Bei bestimmten Werten der Elektrodenspannung traten Fanoresoannzen auf, deren Form vom Magnetfeld und der Elektrodenspannung bestimmt wurde.

Die spezielle Geometrie des Quantenrings erlaubte auch eine Charakterisierung im Coulombblockadebereich, in dem der Ring mit den Elektroden als SET betrieben wurde. Die Transportmessungen zeigten die von einem solchen Bauteil erwarteten Einzelelektronenladeeffekte. Hier fiel ein besonderes Augenmerk auf die Magnetfeldabhängigkeit der elektronischen Zustände im Quantenring. Durch die Auswertung des sogenannten Additionsspektrums in hohen Magnetfeldern bis zu 6 T konnten die Elektronen im Ring genau abgezählt werden. Es ergab sich eine Zahl von weniger als zehn im Bereich der Coulombblockade.

Bei kleinen Magnetfeldern änderte sich der Grundzustand periodisch, jedoch sehr viel häufiger als erwartet. Dieser Effekt konnte durch den

Einfluss der Coulombwechselwirkung zwischen den Elektronen erklärt werden, die die Entartungen zwischen Zuständen mit verschiedenen Drehimpulsquantenzahlen aufhebt.

Von besonderem Interesse war ausserdem die Charakterisierung von Korrelationseffekten zwischen Elektronen auf dem Quantenring und Elektronen aus den Kontakten bei hohen Tunnelankopplungen. Dabei wurde ein Kondoeffekt beobachtet, hervorgerufen durch die Streuung von Elektronen an einem einzelnen, ungepaarten Spin auf dem Quantenring. Messungen zur Temperatur- und Magnetfeldabhängigkeit lieferten die erwarteten Eigenschaften, wie z.B. die universelle Linienform für die temperaturabhängige Leitfähigkeit.

In diesem Transportregime wurden auch Aharonov-Bohm-Oszillationen beobachtet aber in diesem Fall im Bereich der Coulombblockade. Die beobachtete (höhere) Frequenz entsprach der oben beschriebenen, die durch Wechselwirkungseffekte verursacht wurde. Daraus konnte geschlossen werden, dass der Quantenring selbst als Interferometer angesehen werden kann.

Aus diesem Grund erlaubten unsere Transportmessungen die Bestimmung der Phase der Elektronenwellenfunktion in diesem Regime. An den Coulombblockaderesonanzen ergaben sich scharfe Phasensprünge um π. Im Gegensatz dazu zeigten die Messungen zwischen den Resonanzen jedoch eine unerwartete lineare Verschiebung der Aharonov-Bohm-Oszillationen in Abhängigkeit von der Elektrodenspannung und vom Magnetfeld. Dieser Effekt trat erst auf, nachdem ein halbes Flußquantum zur Ringfläche addiert wurde. Diese Beobachtung ist wohl ebenfalls auf einen Wechselwirkungseffekt zurückzuführen. Ein tieferes Verständnis dieser Phänomene erfordert weitergehende theoretische Untersuchungen zu Quantenringen im Kondoregime.

A Inelastic cotunnelling in a quantum ring

Inside a Coulomb-blockade diamond the number of electrons N a quantum dot is constant, see Figure A.1(a). The dominant process leading to transport through a quantum dot in this regime is elastic cotunnelling, see e.g. [129].

Cotunnelling is a second-order process, in which one electron tunnels into the dot and at the same time one electron leaves it, see Figure A.1(b). If the quantum dot is in an excited state after the tunnelling event, this is called inelastic cotunnelling. A schematic picture is shown in Figure A.1(c). These inelastic processes can only occur if an applied source-drain bias V_{SD} exceeds the level spacing of the states ΔE. As

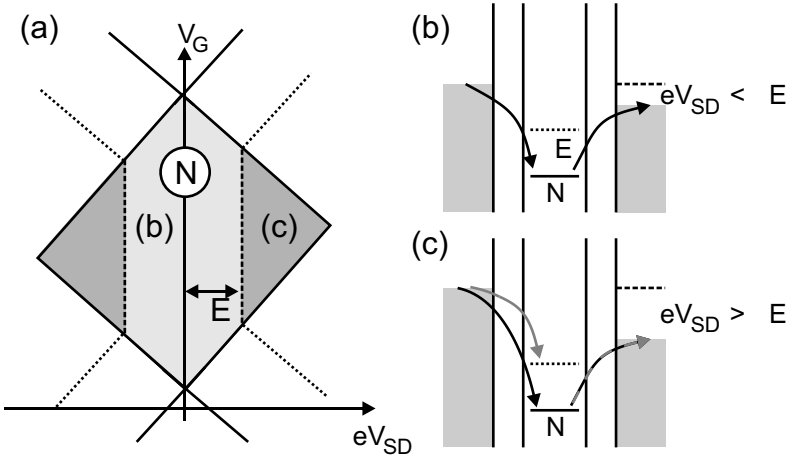

Figure A.1: (a) Coulomb-blockade diamond with N electrons on a quantum dot. The dashed lines depict the source-drain voltage corresponding to an excited state. (b) Elastic cotunnelling for $eV_{SD} < \Delta E$ and (c) inelastic cotunnelling for $eV_{SD} > \Delta E$.

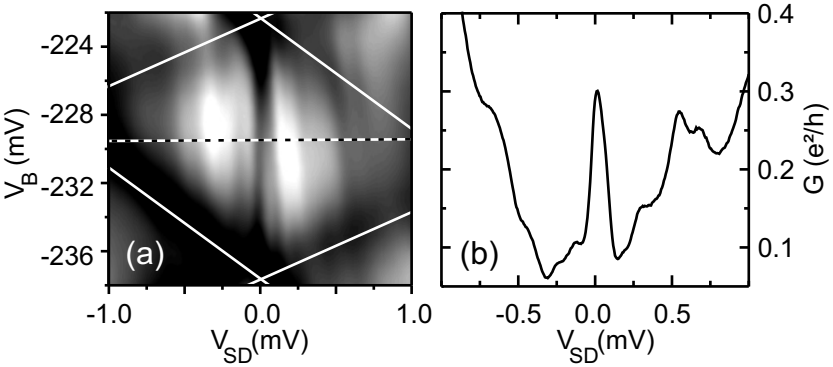

Figure A.2: (a) Coulomb-blockade diamond of our quantum ring with $N = 5$ electrons. Depicted is the differential conductance as a function of V_{SD} and V_B at $V_A = -80$ mV. (b) Non-linear differential conductance at $V_B = -229$ mV, marked by the dashed line in (a). We observe several steps and peaks indicating inelastic cotunnelling.

a consequence this leads to a stepwise increase of the conductance in the Coulomb-blockade diamond as depicted in Figure A.1(a) by the light and dark grey regions at finite bias voltages separated by the dashed lines. These denote the bias voltage for the onset of inelastic cotunnelling.

We observe inelastic cotunnelling in our quantum ring and determine the typical level spacing. In Figure A.2(a) we show the diamond corresponding to $N = 5$ electrons on our ring at $V_A = -80$ mV. At $V_{SD} = 0$ mV the Kondo resonance appears as relatively sharp black line. Please note the vertical grey lines that run parallel to the gate axis. Each denotes the onset of inelastic cotunnelling through an additional excited state. To underline this characteristic we depict a non-linear conductance measurement in Figure A.2(b) at $V_B = -229$ mV. We observe several peaks and steps in the differential conductance which correspond to an average $\Delta E \sim 150$ μeV. We conclude that the level spacing lies around this value for our quantum ring.

In Figure A.3 we show the non-linear conductance as a function of V_{SD} and magnetic field B in a grey-scale map. The Kondo resonance appears as vertical black region around $V_{SD} = 0$. Interestingly, there are diagonal lines in the plot that run from the lower left to the upper right of the plot at low magnetic fields $B < 200$ mT. This is explained

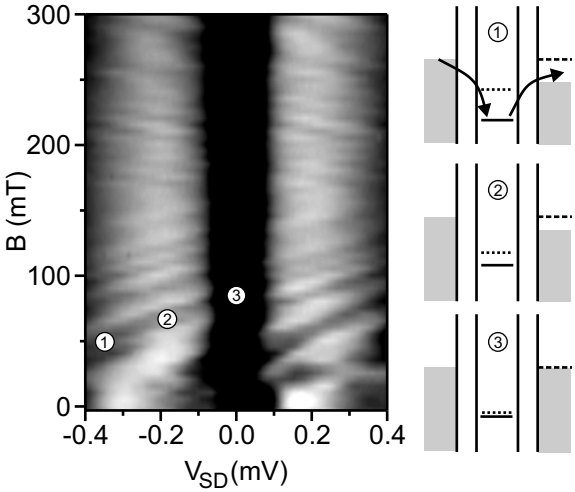

Figure A.3: Grey-scale plot of the non-linear conductance as a function of V_{SD} and magnetic field, the black region around $V_{SD} = 0$ depicts the Kondo resonance at $V_B = -229$ mV and $V_A = -80$ mV. Please note the diagonal lines that run from the lower left to the upper right at low magnetic fields. The numbers denote the positions of the schematic pictures shown at the right-hand side.

by the tuning of the excited states of the quantum ring with the magnetic field.

With increasing B the states with higher angular momentum reduce their energy and finally will be degenerated with the former ground state, see Figure 2.2. At each level-crossing on the ring one of the lines intersects with the central Kondo-resonance. In principle we expect a symmetric behaviour of the system, which would result in a plot with lines running from the lower right to the upper left. The grey-scale map should exhibit a crisscross pattern. The absence of it is possibly caused by the asymmetry of the ring in this gate voltage range.

B Symbols and abbreviations

2DEG	Two **D**imensional **E**lectron **G**as
nD	n-dimensional electron system
AFM	**A**tomic **F**orce **M**icroscope
D	**D**rain contact of a sample
FWHM	**F**ull **W**idth at **H**alf **M**aximum
IPG	**I**n-**P**lane **G**ate
LL	**L**andau **L**evel
MBE	**M**olecular **B**eam **E**pitaxy
NDR	**N**egative **D**ifferential **R**esistance
QD	**Q**uantum **D**ot
QPC	**Q**uantum **P**oint **C**ontact
rel. H.	Relative humidity
RTD	**R**esonant **T**unnelling **D**iode
S	**S**ource contact of a sample
SEM	**S**canning **E**lectron **M**icroscope
SET	**S**ingle-**E**lectron **T**ransistor
SPM	**S**canning **P**robe **M**icroscope
STM	**S**canning **T**unnelling **M**icroscope

$A = D/H$	Aspect ratio of an oxide line
$\vec{A}$	Vector potential
a	Lattice constant of a crystal
α	Voltage to energy conversion factor
B	Magnetic field
C_Σ	Overall capacitance of a quantum dot
C_i	Capacitance between gate i and the quantum dot
C_S	Capacitance between source and quantum dot
C_D	Capacitance between drain and quantum dot
χ	Arm length of an Aharonov-Bohm ring in multiples of π
D	Depth of an oxide line
d_e	Electronic diameter of an Aharonov-Bohm ring

D_e	Electronic diameter of a quantum dot
$D(E)$	Density of states
E	Energy for electrons
e	Elementary charge
E_C	Conduction band edge
E_F	Fermi energy
E_r	Energy of a 1D-subband relative to E_F
E_s	Single-particle energy level on a quantum dot
E_V	Valence band edge
ΔE_z	Zeeman splitting
ε	Energetic distance between $\mu_{QD}(N)$ and μ_S
ϵ	Coupling coefficient for a ring interefrometer
f	Frequency of the Aharonov-Bohm oscillations
$f(E)$	Fermi-Dirac distribution
f_0	Ground frequency of our Aharonov-Bohm ring
F_C	Contact force between AFM tip and sample
Φ_0	Height of a tunnelling barrier above E_C
Φ^{eff}	Effective barrier height above $\mu_{S,D}$
$\phi_0 = h/e$	Magnetic flux quantum
ϕ	Magnetic flux
G	Linear conductance through a sample ($V_{SD} = 0$)
G_0	Conductance at $V_{SD} = 0$
g_{GaAs}	Landé g-factor of GaAs
Γ	Barrier transparency, inverse lifetime
H	Hight of an oxide line
h	Planck constant
$\hbar$	$h/2\pi$
I_{SD}	Source-drain current through a sample
I_{ox}	Oxidation current flowing between AFM tip and sample
k	Spring constant of the cantilever
$\vec{k}$	Wave vector of an electron
k_i	i-th component of the wave vector
k_F	Wave number at E_F
$\delta = k_F \Delta L$	Phase difference between the ring arms
k_B	Boltzmann constant
ΔL	Length difference of the arms of an Aharonov-Bohm ring
l	Angular momentum quantum number
λ_F	Wavelength of the electrons at E_F
l_{1D}	Length of a quantum wire

l_e	Mean-free pass of an electron
l_ϕ	Phase coherence length
m^*	Effective mass of an electron
μ_e	Mobility of a 2DEG
μ_S	Electrochemical potential in the source contact
μ_D	Electrochemical potential in the drain contact
$\mu_{QD}(N)$	Electrochemical potential of a quantum dot
N	Number of electrons on a quantum dot
n_e	Electron density in a 2DEG
N_{Scan}	Number of scan lines for controlled nanomachining
ν	Filling factor in a magnetic field
Ψ	Electronic wave function
R	Resistance of a sample
T	Absolute temperature
$\mathcal{T}_n$	Transmission through the n-th subband of a QPC
t	Transmission coefficient
T_b	Base temperature of the dilution cryostat
T_K	Kondo temperature
Θ	Heaviside function
$U = eV_{SD,U}$	Charging energy of a quantum dot
V	Voltage applied to a sample
V_i	Voltage applied to gate i
V_{ox}	Oxidation voltage applied to the AFM tip
V_{SD}	Source-drain voltage
v_n	Velocity of an electron in the n-th subband
v_{tip}	Tip velocity during the oxidation with an AFM
w	Width of a tunnelling barrier
w_{1D}	Width or point contact
$w_{\mathrm{dpl,x}}$	Depletion width for a nanomachined line

Bibliography

[1] L. P. Kouwenhoven, in *Mesoscopic Electron Transport*, NATO ASI Series, edited by L. L. Sohn, L. P. Kouwenhoven, and G. Schön (Kluwer, Dordrecht, 1997), Vol. 345.

[2] R. Dingle, H. L. Störmer, A. C. Gossard, and W. Wiegmann, Appl. Phys. Lett. **33**, 665 (1978).

[3] G. Binnig and H. Rohrer, Hel. Phys. Acta **55**, 726 (1982).

[4] D. M. Eigler and E. K. Schweizer, Nature **344**, 524 (1990).

[5] G. Binnig, C. F. Quate, and C. Gerber, Phys. Rev. Lett. **56**, 930 (1986).

[6] M. Ishii and K. Matsumoto, Jpn. J. Appl. Phys. **34**, 1329 (1995).

[7] H. W. Schumacher, U. F. Keyser, U. Zeitler, R. J. Haug, and K. Eberl, Appl. Phys. Lett. **75**, 1107 (1999).

[8] Y. Okada, S. Amano, M. Kawabe, B. N. Shimbo, and J. S. Harris Jr., Elec. Lett. **34**, 1262 (1998).

[9] S. Lüscher, A. Fuhrer, R. Held, T. Heinzel, K. Ensslin, and W.Wegscheider, Appl. Phys. Lett. **75**, 2452 (1999).

[10] U. F. Keyser, H. W. Schumacher, U. Zeitler, R. J. Haug, and K. Eberl, Appl. Phys. Lett. **76**, 457 (2000).

[11] Y. Aharonov and D. Bohm, Phys. Rev. **115**, 485 (1959).

[12] L. I. Glazman and M. E. Raikh, JETP Lett. **47**, 452 (1988).

[13] T. K. Ng and P. A. Lee, Phys. Rev. Lett. **61**, 1768 (1988).

[14] D. Goldhaber-Gordon, H. Shtrikman, D. Mahalu, D. Abusch-Magder, U. Meirav, and M. A. Kastner, Nature **391**, 156 (1998).

[15] S. M. Cronenwett, T. H. Oosterkamp, and L. P. Kouwenhoven, Science **281**, 540 (1998).

[16] J. Schmid, J. Weis, K. Eberl, and K. von Klitzing, Physica B **256**, 182 (1998).

[17] F. Simmel, R. H. Blick, J. P. Kotthaus, W. Wegscheider, and M. Bichler, Phys. Rev. Lett. **83**, 804 (1999).

[18] V. Fock, Z. Phys. **47**, 446 (1928).

[19] M. Büttiker, Y. Imry, and R. Landauer, Phys. Lett. A **96**, 365 (1983).

[20] L. Kouwenhoven, *Transport of Electron-Waves and Single-Charges in Semiconductor Nanostructures*, PhD thesis, Technische Universiteit Delft, Netherlands, 1992.

[21] Y. V. Sharvin, JETP **21**, 848 (1965).

[22] C. Cohen-Tanoudji, B. Diu, and F. Laloë, *Quantenmechanik* (W. de Gruyter, Berlin, 1997).

[23] A. J. Peck, *Lateral Tunnelling in Two-Dimensional Electron Systems*, PhD thesis, University of Bath, 1994.

[24] H. W. Schumacher, *Nanostrukturierung mit dem Rasterkraftmikroskop: Vom Zweidimensionalen Elektronengas zum Einzelelektrontransistor*, PhD thesis, Universität Hannover, Germany, 2000.

[25] L. L. Chang, L. Esaki, and R. Tsu, Appl. Phys. Lett. **24**, 593 (1974).

[26] S. Y. Chou, J. S. Harris, and R. F. W. Pease, Appl. Phys. Lett. **82**, 1982 (1988).

[27] S. Adachi, Properties of Aluminium Gallium Arsenide, Gumma University, Japan INSPEC, 1993.

[28] D. Winston, SimWindows Semiconductor Device Simulater1.5.0, University of Colorado, USA.

[29] H. van Houten, B. J. van Wees, M. G. J. Heijman, and J. P. Andre, Appl. Phys. Lett. **49**, 1781 (1986).

[30] R. Held, *Atomic force microscope nanography on semiconductor heterostructures*, PhD thesis, ETH Zürich, Suisse, 2000.

[31] C. Hamann and M. Hietschold, *Raster-Tunnel-Spektroskopie* (Akademie Verlag, Berlin, 1991).

[32] G. Binnig and H. Rohrer, Rev. Mod. Phys. **71**, 324 (1999).

[33] T. D. Stowe, K. Yasumura, T. W. Kenny, D. Botkin, K. Wago, and D. Rugar, Appl. Phys. Lett. **71**, 288 (1997).

[34] U. Mohideen and A. Roy, Phys. Rev. Lett. **81**, 4549 (1998).

[35] X. Jin and W. N. Unertl, Appl. Phys. Lett. **61**, 657 (1992).

[36] H. Fuchs, L. F. Chi, L. M. Eng, and K. Graf, Thin Solid Films **210-211**, 655 (1992).

[37] E. Meyer, R. Overney, R. Lüthi, , D. Brodbeck, L. Howald, J. Frommer, H.-J. Günderodt, O. Wolter, M. Fujihara, H. Takano, and Y. Gotoh, Thin Solid Films **220**, 132 (1992).

[38] T. Sumomogi, T. Endo, K. Kuwhara, R. Kaneko, and T. Miyamoto, J. Vac. Sci. Technol. B **12**, 1876 (1994).

[39] Y. Kim and C. M. Lieber, Science **257**, 1992 (375).

[40] M. Wendel, S. Kühn, H. Lorenz, J. P. Kotthaus, and M. Holland, Appl. Phys. Lett. **65**, 1775 (1994).

[41] V. Bouchiat and D. Esteve, Appl. Phys. Lett. **69**, 3098 (1996).

[42] R. Magno and B. R. Bennett, Appl. Phys. Lett. **70**, 1855 (1997).

[43] J. C. Rosa, M. Wendel, H. Lorenz, J. P. Kotthaus, M. Thomas, and H. Kroemer, Appl. Phys. Lett. **73**, 2684 (1998).

[44] E. Oesterschulze, A. Malavé, U. F. Keyser, M. Paesler, and R. J. Haug, Diamond and Related Materials **11**, 667 (2002).

[45] H. W. Schumacher, U. F. Keyser, U. Zeitler, R. J. Haug, and K. Eberl, Physica E **6**, 860 (2000).

[46] A. Malavé, K. Ludolph, T. Leinhos, C. Lehrer, L. Frey, and E. Oesterschulze, Appl. Phys. A, in press (2002).

[47] M. J. Kelly, *Low-dimensional semiconductors* (Oxford University Press, New York, 1995).

[48] C. W. J. Beenakker and H. van Houten, *Quantum Transport in Semiconductor Nanostructures, Solid State Physics Vol. 44* (Academic Press, 1991).

[49] K. J. Thomas, J. T. Nicholls, M. Y. Simmons, M. Pepper, D. R. Mace, and D. R. Richtie, Phys. Rev. Lett. **77**, 135 (1996).

[50] S. K. Ghandhi, *VLSI Fabrication Principles*, 2nd. ed. (J. Wiley and Sons Inc., 1994).

[51] U. F. Keyser, Diploma thesis, Universität Hannover, Germany, 1999.

[52] P. M. Campbell, E. S. Snow, and P. J. McMarr, Appl. Phys. Lett. **66**, 1388 (1994).

[53] E. S. Snow and P. M. Campbell, Science **270**, 1670 (1995).

[54] E. S. Snow, D. Park, and P. M. Campbell, Appl. Phys. Lett. **69**, 269 (1996).

[55] E. S. Snow, P. M. Campbell, R. W. Rendell, F. A. Buot, D. Park, C. R. K. Marrian, and R. Magno, Appl. Phys. Lett. **72**, 3071 (1998).

[56] R. Held, T. Vancura, T. Heinzel, K. Ensslin, M. Holland, and W. Wegscheider, Appl. Phys. Lett. **73**, 262 (1998).

[57] N. J. Curson, R. Nemutudi, N. J. Appleyard, M. Pepper, D. A. Ritchie, and G. A. C. Jones, Appl. Phys. Lett. **78**, 3466 (2001).

[58] P. Avouris, R. Martel, T. Hertel, and R. Sandstrom, Appl. Phys. A **66**, 659 (1998).

[59] P. A. Fontaine, E. Dubois, and D. Stiévenard, J. Appl. Phys. **84**, 1776 (1998).

[60] H. Bloeß, G. Staikov, and J. W. Schultze, Electrochimica Acta **47**, 335 (2001).

[61] J. A. Dagata, T. Inoue, J. Itoh, and H. Yokoyama, Appl. Phys. Lett. **73**, 271 (1998).

[62] J. A. Dagata, F. P'erez-Murano, G. Abadal, K. Morimoto, T. Inoue, J. Itoh, and H. Yokoyama, Appl. Phys. Lett. **76**, 2710 (2000).

[63] E. S. Snow, G. G. Jernigan, and P. M. Campbell, Appl. Phys. Lett. **76**, 1782 (2000).

[64] Y. Okada, S. Amano, M. Kawabe, and J. S. Harris Jr., J. Appl. Phys. **83**, 7998 (1998).

[65] H. Sugimura, T. Uchida, N. Kitamura, and H. Mauhara, J. Vac. Sci. Technol. B **12**, 2884 (1994).

[66] H. J. Song, M. J. Rack, K. Abugharbieh, S. Y. Lee, V. Khan, D. K. Ferry, and D. R. Allee, J. Vac. Sci. Technol. B **12**, 3720 (1994).

[67] K. Matsumoto, S. Takahashi, M. Ishii, M. Hoshi, A. Kurokawa, S. Ichimura, and A. Ando, Jpn. J. Appl. Phys. **34**, 1387 (1995).

[68] J.-I. Shirakashi, K. Matsumoto, and M. Konagai, Appl. Phys. A **66**, 1083 (1998).

[69] P. Avouris, T. Hertel, and R. Martel, Appl. Phys. Lett. **71**, 285 (1997).

[70] S. Richter, D. Cahen, S. R. Cohen, K. Gartsman, V. Lyakhovitskaya, and Y. Manassen, Appl. Phys. Lett. **73**, 1868 (1998).

[71] G. Krause, Diploma thesis, Universität Hannover, Germany, 2001.

[72] U. Meirav and E. B. Foxman, Semicon. Sci. Technol. **10**, 255 (1985).

[73] J. Weis, *Einzelelektron-Tunneltransistor: Transportspektroskopie der elektronischen Grund- und Anregungszustände in einem GaAs/AlGaAs-Quantentopf*, PhD thesis, Max-Planck-Institut für Festkörperforschung Stuttgart, 1994.

[74] A. D. Wieck and K. Ploog, Appl. Phys. Lett. **56**, 928 (1990).

[75] J. D. Jackson, *Classical Electrodynamics* (John Wiley and Sons, 1975).

[76] K. K. Choi, D. C. Tsui, and K. Alavi, Appl. Phys. Lett. **50**, 110 (1987).

[77] S. Lüscher, *Single electron transport through AFM defined quantum dots*, PhD thesis, ETH Zürich, Suisse, 2001.

[78] C. Livermore, C. H. Crouch, R. M. Westervelt, K. L. Lampmann, and A. C. Gossard, Science **274**, 1332 (1996).

[79] R. H. Blick, R. J. Haug, J. Weis, D. Pfannkuche, K. von Klitzing, and K. Eberl, Phys. Rev. B **53**, 7899 (1996).

[80] R. H. Blick, D. Pfannkuche, R. J. Haug, K. von Klitzing, and K. Eberl, Phys. Rev. Lett. **80**, 432 (1998).

[81] T. H. Oosterkamp, T. Fujisawa, W. G. van der Wiel, K. Ishibashi, R. V. Hijman, S. Tarucha, and L. P. Kouwenhoven, Nature **395**, 873 (1998).

[82] F. Hoffmann, T. Heinzel, D. A. Wharam, J. P. Kotthaus, G. Böhm, W. Klein, G. Kränkel, and G. Weimann, Phys. Rev. B **51**, 13872 (1995).

[83] A. W. Holleitner, C. R. Decker, H. Qin, K. Eberl, and R. H. Blick, Phys. Rev. Lett. **87**, 256802 (2001).

[84] S. Y. Chou, D. R. Allee, R. F. W. Pease, and J. S. H. Jr., Appl. Phys. Lett. **55**, 176 (1989).

[85] K. Ismail, D. A. Antoniadis, and H. I. Smith, Appl. Phys. Lett. **55**, 589 (1989).

[86] K. Seeger, *Semiconductor Physics, An Introduction, 7th edition* (Springer Verlag, Berlin, 1999).

[87] R. G. Chambers, Phys. Rev. Lett. **5**, 3 (1960).

[88] R. A. Webb, S. Washburn, C. P. Umbach, and R. B. Laibowitz, Phys. Rev. Lett. **54**, 2696 (1985).

[89] K. Ismail, S. Washburn, and K. Y. Lee, Appl. Phys. Lett. **59**, 1998 (1991).

[90] G. Cernicchiaro, T. Martin, K. Hasselbach, D. Mailly, and A. Benoit, Phys. Rev. Lett. **79**, 273 (1997).

[91] S. Pedersen, A. E. Hansen, A. Kristensen, C. B. Sørensen, and P. E. Lindelof, Phys. Rev. B **61**, 5457 (2000).

[92] M. Cassé, Z. D. Kvon, G. M. Gusev, E. B. Olshanetskii, L. V. Litvin, A. V. Plotnikov, D. K. Maude, and J. C. Portal, Phys. Rev. B **62**, 2624 (2000).

[93] V. Piazza, F. Beltram, W. Wegscheider, C.-T. Liang, and M. Pepper, Phys. Rev. B **62**, R10630 (2000).

[94] A. F. Morpurgo, J. P. Heida, T. M. Klapwijk, B. J. van Wees, and G. Borghs, Phys. Rev. Lett. **80**, 1050 (1998).

[95] J.-B. Yau, E. P. D. Portere, and M. Shayegan, Phys. Rev. Lett. **88**, 146801 (2002).

[96] M. Büttiker, Y. Imry, and M. Y. Azbel, Phys. Rev. B **30**, 1982 (1984).

[97] S. Pedersen, *Aharonov-Bohm experiments in mesoscopic systems*, PhD thesis, Niels Bohr Institute, University of Copenhagen, Denmark, 1999.

[98] M. Büttiker, in *SQUID'85 - Superconducting Quantum Interference Devices and their Applications*, edited by H. D. Hahlbohm and H. Lübbig (W. de Gryter, Berlin, 1985), p. 529.

[99] E. Buks, R. Schuster, M. Heiblum, D. Mahalu, and V. Umansky, Nature **391**, 871 (1998).

[100] C. W. J. Beenakker and H. van Houten, Phys. Rev. B **39**, 10445 (1989).

[101] *Bergmann Schaefer, Band 4 Teilchen*, edited by W. Raith (W. de Gruyter, Berlin New York, 1992).

[102] U. Fano and J. W. Cooper, Phys. Rev. **137**, A1364 (1964).

[103] J. Göres, D. Goldhaber-Gordon, S. Heemeyer, M. A. Kastner, H. Shtrikman, D. Mahalu, and U. Meirav, Phys. Rev. B **62**, 2188 (2000).

[104] I. G. Zacharia, D. Goldhaber-Gordon, G. Granger, M. A. Kastner, Y. B. Khavin, H. Shtrikman, D. Mahalu, and U. Meirav, Phys. Rev. B **64**, 155311 (2001).

[105] A. Lorke, R. J. Lyuken, A. O. Govorov, J. P. Kotthaus, J. M. Garcia, and P. M. Petroff, Phys. Rev. Lett. **84**, 2223 (2000).

[106] R. J. Warburton, C. Schaflein, D. Haft, F. Bickel, A. Lorke, K. Karral, J. M. Garcia, W. Schoenfeld, and P. M. Petroff, Nature **405**, 926 (2000).

[107] A. Fuhrer, S. Lüscher, T. Ihn, T. Heinzel, K. Ensslin, W. Wegscheider, and M. Bichler, Nature **413**, 385 (2001).

[108] U. F. Keyser, S. Borck, R. J. Haug, W. Wegscheider, M. Bichler, and G. Abstreiter, Semicon. Sci. Technol. **17**, L22 (2002).

[109] W.-C. Tan and J. C. Inkson, Semicon. Sci. Technol. **11**, 1635 (1996).

[110] P. W. Anderson, Phys. Rev. **124**, 41 (1961).

[111] Y. Meir, N. S. Wingreen, and P. A. Lee, Phys. Rev. Lett. **70**, 2601 (1993).

[112] K. Niemelä, P. Pieteläinen, P. Hyvönen, and T. Chakraborty, Europhysics Letters **36**, 533 (1996).

[113] J. Kondo, Progress of theoretical Physics **32**, 37 (1964).

[114] D. Sprinzak, Y. Ji, M. Heiblum, D. Mahalu, and H. Shtrikman, Phys. Rev. Lett. **88**, 176805 (2002).

[115] F. D. M. Haldane, Phys. Rev. Lett. **40**, 416 (1978).

[116] J. Schmid, J. Weis, K. Eberl, and K. v. Klitzing, Phys. Rev. Lett. **84**, 5824 (2000).

[117] S. Tarucha, D. G. Austing, T. Honda, R. J. van der Hage, and L. P. Kouwenhoven, Phys. Rev. Lett. **77**, 3613 (1996).

[118] P. L. McEuen, E. B. Foxman, J. Kinaret, U. Meirav, and M. A. Kastner, Phys. Rev. B **45**, 11419 (1992).

[119] M. Ciorga, A. S. Schrajda, P. Hawrylak, C. Gould, P. Zawadzki, S. Jullian, Y. Feng, and Z. Wasilewski, Phys. Rev. B **61**, 16315 (2000).

[120] J. Nygard, D. H. Cobden, and P. E. Lindelof, Nature **408**, 342 (2000).

[121] D. Goldhaber-Gordon, J. Göres, M. A. Kastner, H. Shtrikman, D. Mahalu, and U. Meirav, Phys. Rev. Lett. **81**, 5225 (1998).

[122] W. G. van der Wiel, S. De Franceschi, T. Fujisawa, J. M. Elzerman, S. Tarucha, and L. P. Kouwenhoven, Science **289**, 2105 (2000).

[123] H. van Houten, C. W. J. Beenakker, J. G. Williamson, M. E. I. Broekaart, P. H. M. van Loosdrecht, B. J. van Wees, J. E. Mooij, C. T. Foxon, and J. J. Harris, Phys. Rev. B **39**, 8556 (1989).

[124] D. Mailly, C. Chapelier, and A. Benoit, Phys. Rev. Lett. **70**, 2020 (1993).

[125] D. Loss and P. Goldbart, Phys. Rev. B **43**, 13762 (1991).

[126] S. Sasaki, S. De Franceschi, J. M. Elzerman, W. G. van der Wiel, M. Eto, S. Tarucha, and L. P. Kouwenhoven, Nature **405**, 764 (2000).

[127] R. Schuster, E. Buks, M. Heiblum, D. Mahalu, V. Umansky, and H. Shtrikman, Nature **385**, 417 (1997).

[128] Y. Ji, M. Heiblum, and H. Shtrikman, Phys. Rev. Lett. **88**, 076601 (2002).

[129] S. De Franceschi, S. Sasaki, J. M. Elzerman, W. G. van der Wiel, S. Tarucha, and L. P. Kouwenhoven, Phys. Rev. Lett. **86**, 878 (2001).

Danksagung

An dieser Stelle möchte ich allen danken, ohne deren Hilfe das Erstellen dieser Arbeit nicht möglich gewesen wäre.

Prof. Dr. Rolf Haug danke ich für die Möglichkeit in seiner Gruppe zu promovieren. Ohne seine Hilfestellung und sein Interesse an diesem Thema wäre diese Arbeit nicht in dieser Form entstanden. Durch die vielen Diskussionen besonders über die Darstellung wissenschaftlicher Ergebnisse habe ich viel gelernt.

Prof. Dr. Werner Wegscheider möchte ich aus zwei Gründen danken. Ohne die extrem flachen zwei-dimensionalen Elektronengase wäre die Herstellung der Quantenringe nicht möglich gewesen. Zudem hat er sich bereit erklärt das Korreferat zu übernehmen.

Dr. Karl Eberl, Dr. Dirk Reuter, Prof. Dr. Andreas Wieck, Max Bichler und Prof. Dr. Gerd Abstreiter haben uns ebenfalls Heterostrukturen zur Verfügung gestellt, Antonio Malavé und PD. Dr. Egbert Oesterschulze die Diamantspitzen entwickelt und gewachsen.

Meinem Kollegen Claus Fühner aus dem "Kon+do"-Raum bin ich zu besonderem Dank verpflichtet. Ohne die vielen Diskussionen, seine Fragen, Hilfe und Aufmunterung hätte ich noch längst nicht die Möglichkeit, diese Danksagung zu schreiben.

Jörn Regul danke ich für die gute Zusammenarbeit bei der Herstellung und Messung der Quantenpunktkontakte und die aufopferungsvolle Durchführung der regelmäßigen "Bürokontrollen".

Ohne meine ehemals "allerbesten" Mitarbeiter Dipl.-Phys. Sebastian Borck und Matthias Paesler würden viele Kapitel fehlen. Ich habe sehr viel von Euch gelernt.

PD Dr. Uli Zeitler und Dr. Frank Hohls hatten immer ein offenes Ohr für Fragen und Probleme eines armen, unwissenden Doktoranden, auch wenn sie eigentlich selbst gar keine Zeit hatten. Eine besondere Erwähnung verdient Phillipp Hullmann, der mir mit manchmal unendlicher Geduld bei meinen Fragen zum Aharonov-Bohm-Effekt geholfen hat. Dr. Hans Werner Schumacher hat mein Interesse am Rasterkraftmikroskop geweckt. Hans Werner und Dr. Thomas Schmidt danke ich für ihre Betreuung während den Anfängen der Doktorarbeit.

Für das Korrekturlesen (von Teilen) der Arbeit danke ich: Melanie Keyser, Uwe Keyser, Frank Hohls, Claus Fühner, Jörn Regul und Ulrich Zeitler. Die SEM-Bilder der verschiedenen AFM-Spitzen stammen von P. Hullmann, M. Rogge, A. Mühle und A. Malavé.

Bei Frau Dr. Isabella Hapke-Wurst, Jens Könemann, André Nauen, Jörg-Michael Meyer und Fritz Schulze Wischeler möchte ich mich ganz besonders für die Hilfe bei den verschiedensten Problemen bedanken. Besonders die Diskussionen waren immer spannend und vor allem spaßig.

Yvonne Griep danke ich für ihr Verständnis und die Hilfe beim Ausfüllen jedweder Anträge und Klara Tetzlaff versorgte uns nicht nur mit flüssigem Helium. Frau Reuter hatte immer ein offenes Ohr für die Fragen eines Doktororanden zur Prüfungsordnung. Der schnellen und genauen Arbeit der feinmechnanischen Werkstatt haben wir insbesondere die Umweltkontrolle des AFM zu verdanken. Vielen Dank für ihre Hilfe, Herr Lehmann. Außerdem möchte ich unseren Systemadministratoren P. Hullmann, G. Sukhodub und A. Nauen für die Betreuung der Rechner danken. Alle aktuellen und ehemaligen Doktoranden und Diplomanden der Abteilung Nanostrukturen haben zu jeder Zeit ein einzigartiges Klima geschaffen, das immer zum Arbeiten anspornte.

Schließlich möchte ich mich bei meinen Eltern Elsa und Uwe Keyser bedanken, die mir dies alles erst ermöglicht haben. Meine Geschwister Hanna und Julius waren immer da, wenn ich sie brauchte. Ganz besonders dankbar bin ich meiner Frau Melanie Keyser, die mir trotz der besonderen Umstände mit ihrem Verständnis und Einsatz zur Seite stand.

Lebenslauf

von Ulrich Felix Keyser, geb. am 31.3.1975 in Braunschweig

1981 - 1985	Besuch der Grundschule Gliesmarode in Braunschweig
1985 - 1987	Besuch der Orientierungsstufe Querum in Braunschweig
1987 - 1994	Besuch des Gymnasiums Ricarda-Huch-Schule in Braunschweig
06/1994	Abitur
1994 - 1996	Grundstudium im Fach Physik an der Technischen Universität Braunschweig
20.9.1996	Vordiplom in Physik
1996-1999	Hauptstudium im Fach Physik an der Universität Hannover
05/1998-05/1998	Diplomarbeit im Institut für Festkörperphysik der Universität Hannover bei Prof. Dr. R. J. Haug mit dem Titel: ,,Herstellung und Charakterisierung von Halbleiternanostrukturen mit dem Rasterkraftmikroskop”
8.6.1999	Diplom in Physik
Seit 1.6.1999	Vorbereitung der Dissertation am Institut für Festkörperphysik der Universität Hannover bei Prof. R. J. Haug
5.8.1999	Heirat mit Melanie Roth